

# Development of Instantaneous Temperature Imaging in Sooty Flames

Doctoral Dissertation

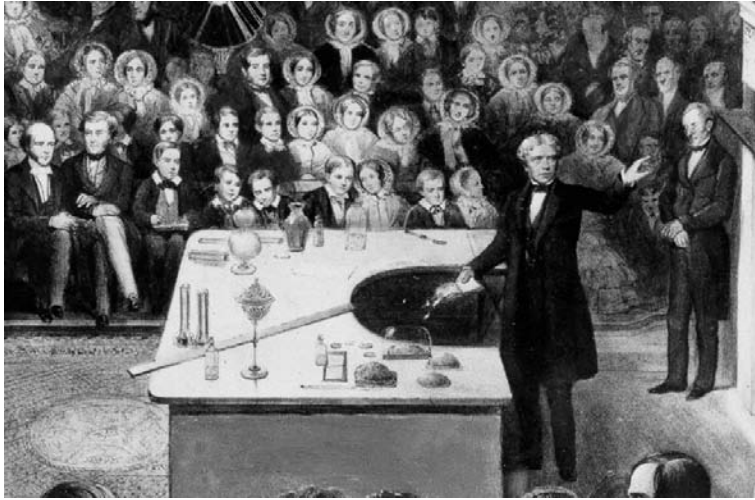
**Qing N. Chan**

January 2011



School of Chemical Engineering  
Faculty of Engineering, Mathematical and Computer Sciences  
The University of Adelaide, Australia

This page intentionally left blank.



“It is to this presence of solid particles in the candle-flame that it owes its  
brilliancy.”

Michael Faraday

19<sup>th</sup> century British Physicist

This page intentionally left blank.

# Declarations

This work contains no material that has been accepted for the award of any other degree or diploma in any university or other tertiary institution and, to the best of my knowledge and belief, contains no material previously published or written by another person, except where due reference has been made in the text.

I give consent to this copy of my thesis when deposited in the University Library, being made available for loan and photocopying, subject to the provisions of the Copyright Act 1968.

The author acknowledges that copyright of published works arising from this thesis (as listed in Appendix C) resides with the copyright holder(s) of those works.

I also give permission for the digital version of my thesis to be made available on the web, via the University's digital research repository, the Library catalogue, the Australasian Digital Theses Program (ADTP) and also through web search engines, unless permission has been granted by the University to restrict access for a period of time.

Qing N. Chan

This page intentionally left blank.

# Acknowledgements

This work would not have been possible without the invaluable contributions and support from numerous people. First and foremost, I must acknowledge the reliable supervision and outstanding assistance provided by my academic supervisors, Dr Zeyad Alwahabi, Prof. Gus Nathan, A/Prof. Bassam Dally and Dr Paul Medwell, whose tutelage has guided me through the highs and lows of a research student. In particular, I owe my deepest gratitude to Dr Paul Medwell, who has made available his support in many ways. It is also necessary for me to thank Dr Peter Kalt, for his insights on work-related and not-so-work-related matters.

I am also indebted to many of the staff members from both Chemical and Mechanical Engineering Departments. In particular, I would like to thank Mary Barrow, Elaine Minerds, Wendy Brown and Yvette Knapp from the offices; Andrew Wright, the Chemical Engineering School's safety officer; Sahn Tran and Billy Constantine, from the IT support group; Richard Pateman, Jason Peak and Jeffrey Hiorns from the workshops, for their constant support throughout the course of this work.

I am also grateful towards my friends, particularly Lucy Lu, Adrian Wun, Tran Nguyen, Winnie Wong, Phuc Nguyen, Ivan Ho, Melissa Supangat and Ryan Tan, for their support and companionship. Above all, I must express my gratitude towards my family for their endless support. Without them, none of this would have been possible.

This page intentionally left blank.

# Abstract

This dissertation reports on the single-shot temperature imaging in sooty flames, based on the development of two-line atomic fluorescence (TLAF), with neutral Indium atom as seeded thermometry species. The TLAF technique in the linear excitation regime has previously been demonstrated to be feasible in sooty environments but single-shot imaging, which requires a higher signal-to-noise ratio (SNR), has been elusive.

The previous TLAF theory has been extended from the linear excitation into the nonlinear excitation fluence regime. Nonlinear regime two-line atomic fluorescence (NTLAF) provides superior signal, and improves single-shot precision from  $\sim 250$  K for the linear TLAF to  $\sim 100$  K for the NTLAF. The NTLAF technique is shown to resolve the temperature profiles across a range of equivalence ratios for natural gas, hydrogen, and ethylene laminar premixed flames, with deviation from radiation-corrected thermocouple measurements not exceeding 100 K, and typically  $\sim 30$  K. Measurements in lightly sooty flames demonstrate good capacity of the NTLAF technique to exclude interferences that hamper most two-dimensional laser-based thermometry techniques.

The developed technique has been further assessed in a laminar nonpremixed flame. The results show the expediency of the technique in the study of the reaction zone, and reveal interesting findings about the Indium formation process. The temperature profile across the reaction zone shows good agreement with laminar flame calculations. Indium fluorescence is observed to be strongest at the flame front, where the temperature exceeds 1000 K.

Indium has been typically seeded into flame as Indium Chloride dissolved in distilled water. The feasibility to improve on the signal quality of the developed

technique, through the substitution of distilled water with an organic solvent (namely acetone, isopropanol, methanol, and ethanol) as the seeding solution, has been examined. Acetone and methanol are shown to enhance the fluorescence signal intensity the most (approximately threefold to fivefold at stoichiometric flame condition) when used. Acetone and methanol are also shown to improve the fluorescence emission across a range of equivalence ratios, most significantly in the rich combustion region, as well as a twofold enhancement in the SNR. The use of acetone or methanol, has the potential to reduce the precision of the measurements down to  $\sim 60$  K.

The use of the NTLAF technique for measurements in flames with high soot loadings was assessed. In particular, the interferences from soot or its precursors on the fluorescence measurements have been evaluated. The findings indicate that interferences, such as spurious scattering and laser-induced incandescence (LII), from soot are not significant. However, interferences from soot precursors, predominantly condensed species (CS) and perhaps polycyclic aromatic hydrocarbons (PAH), are substantial. Potential detection schemes to correct or circumvent these interferences have been identified.

The technical feasibility of the NTLAF technique to be used concurrently with the LII technique to provide simultaneous single-shot imaging of temperature and soot concentration has been demonstrated. The joint NTLAF-LII method has been applied to laminar premixed and nonpremixed flames, as well as a wrinkled nonpremixed flame. No significant interference of the two measurement techniques on each other is observed, for the detection and timing schemes employed. The images also reveal that, whilst NTLAF has a limited operating range, this range is sufficient to span all regions with soot. This observation demonstrates the applicability of the joint NTLAF-LII method in assessing the coupled dependency of temperature and soot in flame.

# Contents

<b>Declarations</b>	<b>i</b>
<b>Acknowledgements</b>	<b>iii</b>
<b>Abstract</b>	<b>v</b>
<b>1 Introduction</b>	<b>1</b>
1.1 Motivation . . . . .	1
1.2 Aims . . . . .	5
1.3 Dissertation Layout . . . . .	5
<b>2 Background Literature</b>	<b>9</b>
2.1 Laser Diagnostics in Sooty Flames . . . . .	9
2.2 Laser-Based Thermometry Techniques . . . . .	10
2.3 Two-Line Atomic Fluorescence . . . . .	15
2.4 Laser-Based Soot Measurement Techniques . . . . .	19
<b>3 Experimental Details</b>	<b>21</b>
3.1 Burners and Seeding Arrangements . . . . .	21
3.2 Laser Systems . . . . .	29
3.3 Experimental Layout . . . . .	30
3.4 Data Processing . . . . .	36
3.5 General Error Sources . . . . .	38

<b>4</b>	<b>Linear Two-Line Atomic Fluorescence (TLAF)</b>	<b>43</b>
4.1	Introduction . . . . .	43
4.2	Methodology . . . . .	44
4.3	Experimental Arrangement . . . . .	45
4.4	Results and Discussion . . . . .	47
4.5	Summary . . . . .	55
<b>5</b>	<b>Assessment of Nonlinear Regime TLAF (NTLAF) in Laminar Premixed Flames</b>	<b>57</b>
5.1	Introduction . . . . .	57
5.2	Methodology . . . . .	58
5.3	Experimental Arrangement . . . . .	59
5.4	Results and Discussion . . . . .	61
5.5	Summary . . . . .	69
<b>6</b>	<b>Assessment of NTLAF in Laminar Nonpremixed Flames</b>	<b>71</b>
6.1	Introduction . . . . .	71
6.2	Experimental Arrangement . . . . .	72
6.3	Results and Discussion . . . . .	73
6.4	Summary . . . . .	77
<b>7</b>	<b>Solvent Effects on NTLAF Measurements</b>	<b>79</b>
7.1	Introduction . . . . .	79
7.2	Methodology . . . . .	80
7.3	Experimental Arrangement . . . . .	82
7.4	Results and Discussion . . . . .	83
7.5	Summary . . . . .	93
<b>8</b>	<b>Application of NTLAF in Sooty Flames</b>	<b>95</b>
8.1	Introduction . . . . .	95

8.2	Experimental Arrangement . . . . .	96
8.3	Results and Discussion . . . . .	100
8.4	Summary . . . . .	114
<b>9</b>	<b>Simultaneous Application of NTLAF and LII</b>	<b>115</b>
9.1	Introduction . . . . .	115
9.2	Experimental Arrangement . . . . .	116
9.3	Results and Discussion . . . . .	118
9.4	Summary . . . . .	125
<b>10</b>	<b>Summary and Conclusions</b>	<b>127</b>
<b>A</b>	<b>Theoretical Derivations</b>	<b>151</b>
A.1	Linear Two-Line Atomic Fluorescence . . . . .	151
A.2	Nonlinear Two-Line Atomic Fluorescence . . . . .	153
<b>B</b>	<b>Radiation Correction</b>	<b>155</b>
<b>C</b>	<b>Publications</b>	<b>157</b>

This page intentionally left blank.

# List of Figures

2.1	The relative distribution of the irradiated laser line, the Rayleigh line and the transmission curve of the iodine filter as a function of wavenumber. . . . .	11
2.2	CARS excitation diagram of a $N_2$ molecule. . . . .	12
2.3	Schematic diagram of the fluorescence processes for Indium. . . .	17
2.4	Well-characterized calibration flames employed for the calibration of LII measurements. . . . .	20
3.1	Photograph of the square flat-flame burner and the premixed flame, here firing natural gas. . . . .	23
3.2	Cutaway view of the square flat-flame burner. . . . .	23
3.3	Photograph of the circular flat flame burner with a honeycomb matrix. . . . .	24
3.4	Cutaway view of the circular flat-flame burner. . . . .	24
3.5	Photograph of the JHC burner. . . . .	26
3.6	Cutaway view of the JHC burner. . . . .	26
3.7	Photograph of the pneumatic nebulizer. . . . .	28
3.8	Photograph of the ultrasonic nebulizer. . . . .	28
3.9	Pictorial representation of experimental layout. . . . .	30
3.10	Schematic details of experimental layout. . . . .	32
3.11	Timing details for the lasers and the detection systems for simultaneous TLAF/LII. . . . .	33
3.12	Timing diagram for simultaneous TLAF/LII. . . . .	34
3.13	General data processing steps. . . . .	37

4.1	Energy transitions involved in the TLAF process. . . . .	44
4.2	Indium fluorescence as a function of spectral intensity in the linear fluence regime. The fluorescence signals are normalized to the local maximum values. . . . .	47
4.3	Indium fluorescence as a function of Indium Chloride concentration. The fluorescence signals are normalized to the local maximum values. . . . .	48
4.4	Typical instantaneous images of (a) Stokes, (b) anti-Stokes Indium fluorescence and (c) temperature in Flame 1 (Table 4.1). . . . .	51
4.5	Typical averaged images of (a) Stokes, (b) anti-Stokes Indium fluorescence and (c) deduced temperature in Flame 1 (Table 4.1). . . . .	53
4.6	Typical deduced 200-shot averaged temperature image in Flame 2 (Table 4.1). . . . .	54
4.7	Indium fluorescence as a function of spectral intensity to the maximum achievable laser fluence. . . . .	55
5.1	Flame fluorescence as a function of tank fluorescence for (a) Stokes and (b) anti-Stokes processes. Dots: NTLAF measurements. Solid line: curve fit. . . . .	60
5.2	Typical instantaneous images of (a) Stokes and (b) anti-Stokes Indium fluorescence and (c) deduced temperature in Flame 1 (Table 5.1). . . . .	62
5.3	Temperature histograms for a typical instantaneous image of Flame 1 (Table 5.1) for (a) linear ( $2500 \text{ W/cm}^2/\text{cm}^{-1}$ ) and (b) nonlinear ( $250,000 \text{ W/cm}^2/\text{cm}^{-1}$ ) excitation regimes. . . . .	63
5.4	Normalized fluorescence signal in Flame 3 (Table 5.1) as a function of equivalence ratio. The fluorescence signals are normalized with respect to the local maximums. . . . .	64
5.5	Temperature of Flame 3 (Table 5.1) over a range of equivalence ratios for NTLAF and calibrated thermocouple measurements. . . . .	65
5.6	Temperature of Flame 4 (Table 5.1) over a range of equivalence ratios for NTLAF and calibrated thermocouple measurements. . . . .	66
5.7	Temperature of Flame 5 (Table 5.1) over a range of equivalence ratios for NTLAF and calibrated thermocouple measurements. . . . .	67

5.8	(a) Photograph of natural light emission from ethylene/air flame with $\Phi=2.25$ showing soot. Dashed area indicates approximately laser-imaging area. (b) Instantaneous NTLAF temperature image for this flame with nonlinear fluence excitation ( $250,000 \text{ W/cm}^2/\text{cm}^{-1}$ ). . . . .	68
6.1	Typical instantaneous images of (a) Stokes and (b) anti-Stokes fluorescence and (c) deduced temperature in a laminar nonpremixed flame. . . . .	74
6.2	Boltzmann fraction as a function of temperature. . . . .	75
6.3	Temperature profile across the reaction zone of a laminar nonpremixed flame, from NTLAF measurements and laminar flame calculations. . . . .	76
7.1	Typical instantaneous images of (a) Stokes and (b) anti-Stokes fluorescence in a laminar premixed natural gas flat-flame. . . . .	84
7.2	Normalized Indium Stokes and anti-Stokes fluorescence for five different seeding solutions for a flame equivalence ratio of 1.0. The fluorescence signals are normalized with respect to the fluorescence signal recorded with water as seeding solution. . . . .	85
7.3	Normalized Indium (a) Stokes and (b) anti-Stokes fluorescence over a range of concentration of organic solvents within seeding solution, balanced with water. The fluorescence signals are normalized by the fluorescence recorded with water as seeding solution. . . . .	87
7.4	Indium fluorescence as a function of flame equivalence ratio. . . . .	88
7.5	Normalized fluorescence signal as a function of flame equivalence ratio. The fluorescence signals are normalized with respect to local maximums. . . . .	90
7.6	Relative gain in SNR of the Indium fluorescence as a function of flame equivalence ratio. . . . .	91
7.7	Temperature histograms from typical instantaneous images of laminar premixed flame with a flame equivalence ratio of $\sim 1.55$ with (a) acetone (b) methanol and (c) water as seeding solution. . . . .	92
8.1	Typical averaged on-wavelength (a) Stokes, (b) anti-Stokes measurements and (c) LII soot volume fraction distribution in Flame 2 (Table 8.1). . . . .	99

8.2	Typical averaged off-wavelength (a) Stokes and (b) anti-Stokes measurements in Flame 2 (Table 8.1).	100
8.3	Typical averaged on-wavelength measurements, with off-wavelength measurements overlaid for (a) Stokes and (b) anti-Stokes processes in Flame 2 (Table 8.1).	102
8.4	Typical averaged off-wavelength measurements with LII soot volume fraction overlaid for (a) Stokes and (b) anti-Stokes processes in Flame 2 (Table 8.1).	102
8.5	Average radial profiles for the (a) Stokes and (b) anti-Stokes processes extracted at a HAB of 25 mm in Flame 2 (Table 8.1).	104
8.6	Averaged radial profiles for the on-wavelength measurements at four different laser fluences, extracted at a HAB of 25 mm in Flame 2 (Table 8.1).	106
8.7	Maximum off-wavelength to on-wavelength measurements ratio as a function of laser fluence.	107
8.8	Averaged radial profiles as a function of radial distance from peak soot volume fraction location, extracted at a HAB of 25 mm in Flame 1 to 5 (Table 8.1).	109
8.9	Averaged radial profiles for the corrected on-wavelength measurements at four different laser fluences, extracted at a HAB of 25 mm in Flame 2 (Table 8.1).	111
8.10	Averaged radial profiles extracted at a HAB of 25mm in Flame 1 (Table 8.1).	112
8.11	Comparison of the maximum off-wavelength to on-wavelength measurements ratio and the maximum soot volume fraction at different flame equivalence ratios.	113
9.1	Simultaneous single-shot images for a laminar premixed ethylene-air flame. (a) Stokes, (b) anti-Stokes Indium fluorescence, (c) NT-LAF temperature and (d) LII soot volume fraction.	120
9.2	Simultaneous single-shot images for a laminar nonpremixed ethylene-air flame. (a) Stokes, (b) anti-Stokes Indium fluorescence, (c) NTLAF temperature, (d) LII soot volume fraction and (e) instantaneous temperature field with location of soot overlaid (in grey).	123

9.3	Simultaneous single-shot images of a wrinkled nonpremixed ethylene-air flame. (a) Stokes, (b) anti-Stokes Indium fluorescence, (c) NTLAF temperature, (d) LII soot volume fraction and (e) instantaneous temperature field with location of soot overlaid (in grey). . . . .	124
9.4	Soot volume fraction as a function of temperature for laminar nonpremixed and wrinkled nonpremixed flames. . . . .	125

This page intentionally left blank.

# List of Tables

4.1	Premixed flat-flame conditions. . . . .	46
4.2	Maximum temperature measurements and calculations for a pre-mixed natural gas/air flame. . . . .	50
5.1	Premixed flat-flame conditions. . . . .	61
7.1	Premixed flat-flame conditions. . . . .	82
7.2	Selected physical properties of the solvents at 20 °C and 1 atm, and the median diameters of the resultant droplets estimated using Lang's correlation. . . . .	82
8.1	Parameters of the fuel stream at the exit of the central fuel jet, issuing into a fixed air co-flow, for the flame conditions of interest. . . . .	97

This page intentionally left blank.

# Chapter 1

## Introduction

In this chapter, a brief outline of the research field is presented, leading to the motivation behind this work. This is followed by the specific aims of this work and the dissertation layout.

### 1.1 Motivation

Soot is a general term that refers to the black carbonaceous substance consisting of fine particles resulting from incomplete combustion processes [1, 2].

Soot, when present within a flame, plays an important role in radiative heat transfer — the dominant heat transfer mode in combustion systems such as kilns, boilers and furnaces [3, 4, 5]. An increased presence of soot within a flame acts to enhance the flame emissivity, and hence the radiative heat output and the radiant cooling of the flame [6]. This is because soot produces broadband incandescent radiation, which typically dominates over the narrowband radiation from intermolecular processes. Beyond a flame, carbon black is an important commercial combustion product used in several applications, including elastomers, tyres and inks [7, 8].

On the other hand, soot is also an unsightly emission from combustion processes [2, 9] and has been shown to be a major environmental pollutant [10]. Soot is the aerosol that is most responsible for the reduced atmospheric transparency

and visibility [11]. The presence of soot particles in the atmosphere has been suggested to result in regional [1] and global climate change [11, 12], in addition to having an adverse effect on the hydrological cycle [9]. Soot also presents a major health risk [11, 13] because of its high toxicity and small particulate size [11], making it easy to inhale and difficult to expel. Recent studies (*e.g.*, [13, 14]) have suggested that soot aerosol plays a major role in deaths associated with particulate air pollution.

While combustion systems involving soot have been applied for many years, the formation, growth, transportation, and destruction of soot, involve complex chemical and physical two-phase processes that occur simultaneously, are still beyond the present capacity to model adequately [7, 8, 15]. For example, the soot precursors are formed from the pyrolysis and/or the oxidation of fuel molecules. These precursor particles subsequently undergo surface growth through interaction with gas-phase species, coagulation growth by colliding and coalescing with one another, and oxidation. These processes are also dependent on a multitude of parameters such as fuel type, mixture fraction, temperature and strain rate [7, 16].

Many of these parameters are interdependent and are further coupled in the presence of turbulence, as the time scales of the soot formation and destruction processes are of the same magnitude as the time scale of mixing [6]. Simultaneous measurements of these interdependent parameters are therefore important to enable direct correlations, and to reveal information on the interactions of these coupled dependencies [17]. These simultaneous data are important for both the advancement of the understanding and the development of the capacity to model the soot processes.

It is desirable for the measurements to be of a multi-dimensional nature to provide physical insights, in addition to spatially correlated measurements and scalar gradients [18], which are not possible with single-point measurements [19]. Multi-dimensional measurements are also useful to capture the large-scale coherent motions that are inherent in turbulent systems. While three-dimensional measurement techniques have been reported in the literature (*e.g.*, [20]), such approaches have yet to be widely implemented in practice due to the complexity and the specialized nature of the equipment involved. Planar measurement techniques

are more commonly used by researchers.

It is also important for the measurements to be acquired at a temporal resolution comparable to the time scale of the combustion process of interest. The acquisition of such temporally resolved measurements is especially crucial for the study of rapidly varying reactive flow with complex fluid dynamic, such as turbulent flames.

It is for these reasons that **simultaneous**, **planar**, and **instantaneous** measurements of the interdependent parameters are important to shed light on the processes associated with the evolution of soot in flame, particularly in the presence of turbulence.

A multitude of interdependent parameters are fundamental to the understanding of soot. Of these, temperature is a dominant parameter in the combustion processes, and plays a major role in radiation heat transfer owing to its fourth-power influence on heat transfer. Temperature characterises the enthalpy of reaction, controls many of the important chemical and physical processes occurring within the flame [21], and influences the composition of the combustion products [22]. Temperature is also an important parameter used in the modelling of many combustion phenomena, including the soot formation processes [22]. An accurate and reliable measurement of temperature is therefore important.

Physical probing methods, traditionally employed for combustion diagnostics (*e.g.*, [23]), are intrusive and may perturb the combustion processes under investigation [24]. Additionally, the probes used are typically characterised by modest spatial and temporal resolution, and therefore cannot be used to investigate flames with steep gradients. Also, as with any physical probes, the measurements are typically *ex situ*, and the readings obtained often require corrections before meaningful interpretations can be made. All these issues imply that experimental investigations with the use of physical probes are difficult to perform with reasonable accuracy in some combustion environments, such as turbulent flames.

Laser-based techniques, on the other hand, offer a number of advantages over the physical probing methods. The laser-based techniques are well-suited to provide *in situ*, instantaneous, nonintrusive, temporally and spatially precise measure-

ments of many important parameters of interest [25, 26]. A variety of laser-based thermometry techniques have been developed [26]. However, most of these are limited to idealized combustion environments and are not applicable in the presence of particles, such as dust, coal, biomass and soot. Absorption, scatter and other interferences prevent many of these laser-based diagnostic techniques from being applied reliably in such combustion environments.

Two-line atomic fluorescence (TLAF) is a laser thermometry technique based on the relative temperature-dependent population of two energy levels within an atomic species. The temperature is deduced from the ratio of the fluorescence signals associated with the transitions. Not only does TLAF offer two-dimensional measurements, the inelastic nature of the TLAF technique, when spectrally-shifted emissions are used, enables filtering to be used to minimize interferences from spurious scattering such as Mie scattering. This allows measurements to be performed in particle-laden environments. Of the atomic species available, indium seeded into the flame has been identified as a suitable thermometry species for TLAF [27]. Indium has good sensitivity within a temperature range that is relevant to most combustion systems. Additionally, the transition wavelengths of the indium atom are in the visible spectrum (*viz.* 410 nm and 450 nm) where interferences are less pronounced than in the ultraviolet (UV) range.

Previous TLAF studies, however, have been limited to the linear excitation regime. Under such conditions, the signal is plagued by low signal-to-noise ratio (SNR) [28], thus preventing useful single-shot imaging that requires higher SNR. Of the few studies that have applied linear TLAF, averaged results have typically been reported. With some notable exceptions (*e.g.*, [29]), virtually all past work on linear TLAF have been performed in laminar flames, and thus the limitation of measuring time-averaged temperature has been acceptable. In the context of the dynamic turbulent flames that are of more practical significance, however, such averaged data are insufficient.

The lack of reliable approaches to provide accurate instantaneous planar measurements of temperature in turbulent sooty flames has resulted in the deficiency of detailed data set of such to date. This provides a significant barrier to the capacity to understand and to model the various soot processes. There is therefore

an apparent need for the development of an alternative laser-based thermometry techniques, to complement and extend those already in common use, for measurements in turbulent sooty flames.

## 1.2 Aims

With a view of the aforementioned issues, the aim of this work is to develop the existing linear TLAFF technique to permit instantaneous imaging in turbulent sooty flames. The four specific aims comprising this work are:

- To assess the capability of the existing linear TLAFF technique in providing single-shot temperature imaging.
- To improve the TLAFF technique to achieve sufficient SNR to permit single-shot temperature imaging.
- To assess the capability of the developed technique to perform measurements in flames of high soot loadings.
- To demonstrate the technical feasibility of the developed technique to be used concurrently with other laser diagnostic method for simultaneous measurements in sooty flames.

## 1.3 Dissertation Layout

This dissertation consists of ten chapters. Following this chapter, Chapter 2 describes the background literature concerning laser diagnostics in sooty flames that are of relevance to this work. A critical review on the laser-based techniques that are commonly employed in the field of combustion for temperature and soot concentration measurements is presented. The literature review confirms the need for a reliable approach for accurate instantaneous temperature imaging in turbulent sooty flames.

The experimental apparatus and setup used for this work are outlined in Chapter 3. The details of the burners used are presented. The technical details of the data collection, and the image processing procedures are described as well.

The first aim of the work is addressed in Chapter 4. The capacity of the TLAF technique, in the linear excitation regime, to provide single-shot temperature imaging in laminar premixed flames is assessed. The instantaneous and averaged images for both the fluorescence and temperature measurements are presented and compared. These images serve as necessary references for measurements in subsequent chapters.

Chapter 5 to Chapter 7 describe, in chronological order, the development of the existing linear TLAF technique to achieve sufficient SNR for single-shot temperature imaging, which addresses the second aim of the work. A flat-flame burner, which is well suited for validation purposes [30, 31], was used. Chapter 5 presents the derivations made to facilitate the application of TLAF in the nonlinear excitation regime. To assess the validity of the derivations, the nonlinear excitation regime TLAF (NTLAF) measurements are compared with radiation-corrected thermocouple readings for laminar premixed natural gas, hydrogen and ethylene flames, across a range of flame equivalence ratios. The validity of the derivations is further assessed in Chapter 6, where the NTLAF technique is used to resolve the temperature profile across the reaction zone of a laminar nonpremixed flame. The measured profile is compared with laminar flame calculations. In Chapter 7, the feasibility to improve on the signal quality of the NTLAF measurements, through the substitution of water with an organic solvent as the seeding medium, is investigated. Measurements using organic solvents and organic solvent-water mixtures as seeding solution are presented and compared with those using water.

The use of the NTLAF technique for reliable measurements in flames with high soot loadings is assessed in Chapter 8, which addresses the third aim of the work. The measurements obtained, when induced on- and off-wavelength, are compared over a range of operating laser fluences and flame conditions. These measurements are also used for the identification of potential detection schemes to correct or to circumvent these interferences.

The fourth aim of the work is addressed in Chapter 9. In Chapter 9, the technical feasibility of the NTLAF method to be used concurrently with laser-induced

incandescence (LII) technique for simultaneous imaging of temperature and soot concentration in sooty flames is assessed. The joint NTLAF-LII method is used to image three flames with different characteristics, namely, laminar premixed, laminar nonpremixed, and wrinkled nonpremixed flame.

Conclusions and recommendations for future work are presented in Chapter 10.

A significant portion of the work has been submitted to archival scientific journals — with six papers accepted for publication and three papers under review (see Appendix C).

This page intentionally left blank.

# Chapter 2

## Background Literature

In this chapter, the background literature concerning laser diagnostics in sooty flames of relevance to this research is presented and discussed.

### 2.1 Laser Diagnostics in Sooty Flames

Laser-based measurement techniques have supplied the combustion research community with *in situ*, instantaneous, nonintrusive, temporally and spatially precise measurement of many important parameters of interest [26]. Producing experimental data sets in flames containing soot using laser-based techniques has been problematic, however [32]. The specific problems that prevent many laser diagnostic techniques from being applied reliably to sooty flames include [24, 32]:

- **Background luminosity:** Increased background luminosity due to the soot particulate blackbody continuum radiation.
- **Laser-induced fluorescence:** Fluorescent interferences from soot precursors and particulates due to the abundance of such species in sooty flames.
- **Laser modulated particulate incandescence:** Increased quantities of the blackbody radiation and molecular emissions from the  $C_n$  species, when the soot particles absorb the incident laser radiation with sufficiently high flux.

- **Absorption and scattering:** Extinction of the incident laser radiation through absorption and/or scattering when the carbonaceous particulates are present.

## 2.2 Laser-Based Thermometry Techniques

A brief review of the various laser-based thermometry techniques that are commonly applied in the field of combustion and the extension of these techniques to measurements in sooty flames is presented. Particular focus is brought onto the two-line atomic fluorescence (TLAF) method, which is the laser technique of choice for this work.

### 2.2.1 Rayleigh Scattering

A relatively simple laser-based thermometry technique is Rayleigh scattering. Rayleigh scattering is a form of elastic scattering of the light quanta from particulate matters with dimensions that are significantly smaller than the wavelength of the radiation. The basic operating principle of Rayleigh scattering involves the utilization of the elastic scatter of light from molecules to give a measure of the total molecular number density, which when coupled with ideal gas law, allows the temperature to be deduced. The extent of the scattering from the probe volume is dependent on the total molecular number density and the species dependent Rayleigh cross-section of the composition. It is therefore necessary to determine the composition in the probe volume by other means.

Rayleigh scattering, however, is highly susceptible to interference from the elastically scattered light from particles (Mie scattering) and surfaces. Mie scattering is especially significant in sooty flames since the soot particles are typically of dimensions that are comparable or greater than the wavelength of radiation. Rayleigh scattering can therefore only be employed under particle-free environments, which limits its applicability in practical combustion systems [33].

Filtered Rayleigh scattering (FRS) is an extension of the conventional Rayleigh scattering and was first proposed by Miles *et al.* [34]. This technique has

NOTE:

This figure is included on page 11 of the print copy of the thesis held in the University of Adelaide Library.

**Figure 2.1:** The relative distribution of the irradiated laser line, the Rayleigh line and the transmission curve of the iodine filter as a function of wavenumber. The shaded area is the FRS signal [33].

been widely investigated subsequently (*e.g.*, [33, 35, 36, 37, 38]). The FRS technique utilizes a narrowband filter at the centre-frequency of a single mode laser to reject interference that is spectrally identical to the incident light. The FRS technique has been primarily used with molecular-iodine filters paired with frequency-doubled single-mode Nd:YAG lasers. The unfiltered component of the pressure- and/or temperature-broadened signal is subsequently used for thermography (Figure 2.1). The filter allows temperature imaging to be performed in the presence of strong elastic scatter that would otherwise obscure the Rayleigh scattered signal. Nevertheless, the degradation of the molecular-filter performance with pulsed lasers [39, 40] prevents the application of the FRS technique to flames with high soot loadings. Also, the FRS technique remains susceptible to variation in the Rayleigh cross-section across the reaction zone, which can be difficult to account for in turbulent flames.

### 2.2.2 Raman Scattering

One approach to circumvent problems associated with elastic scatter from particles is to employ Raman scattering for thermometry [24]. Raman scattering is an inelastic process, whereby the scattered light can be frequency shifted to either longer (Stokes Raman) or shorter (anti-Stokes Raman) wavelength. The

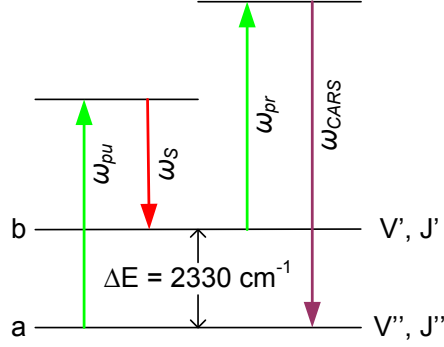


**Figure 2.2:** CARS excitation diagram of a  $N_2$  molecule. Adapted from [42].

Raman scattered signal is species specific and is linearly proportional to the number density of the species. Temperature measurements can be made readily from the spectral distribution of the scattering [24]. Raman scattering, however, is a weak process since only a small fraction of the incoming light (1 in  $10^7$  photons) is scattered inelastically [41]. This results in the Raman signal being highly susceptible to interferences. Also, the weak nature of the Raman scattering limits the technique to point or line measurements.

Offering stronger signal, coherent anti-Stokes Raman spectroscopy (CARS)-based thermometry is more applicable to luminous and particle-laden flows [43]. The basic operating principle of CARS [24, 26] involves the use of three laser beams (typically two of the same wavelength) that interact in the measurement volume to generate the signal (as a fourth beam) as a result of the third-order nonlinear susceptibility. A ‘pump’ beam at frequency  $\omega_{pu}$  (non-resonant to molecular transitions) excites a virtual level. By tuning a second Stokes beam to frequency  $\omega_S$ , where  $\omega_{pu} - \omega_S$  corresponds to a vibrational or rotational transition of the molecule, Raman resonance occurs. A third ‘probe’ beam ( $\omega_{pr}$ ) is then used to generate a coherent CARS signal at  $\omega_{CARS} = \omega_{pu} - \omega_S + \omega_{pr}$ . The processes involved in the generation of CARS signal from a  $N_2$  molecule are depicted in Figure 2.2 [42]. By scanning the Stokes beam across the Raman transitions of the molecule, the spectral shape is used to determine the temperature. Scanning of the Stokes wavelength may be performed on a shot-by-shot basis, or alternatively a broadband laser enables single-shot spectra to be generated.

A key advantage of the CARS technique for assessing practical systems results from the frequency shift in the signal relative to the excitation beams. This allows filtering to separate the influence of scattered interference from soot. In exciting  $\text{N}_2$ ,  $\text{O}_2$  and  $\text{CO}_2$ , the CARS technique has the advantage of avoiding seeding, and accessing species that are widely present in the flame. The CARS signal is also coherent, thus allowing the signal to noise be increased by moving the collection optics further from the flame, since the background is incoherent. Careful selection of the excitation scheme, however, is necessary to minimize soot interferences [44]. Approaches include a dual-pump CARS [45, 46] and shifted vibrational CARS [47]. The use of short-pulse (sub-nanosecond) laser for delayed probing of CARS has also been recently shown to be effective in the suppression of the nonresonant background and elastic scattering, thus providing high signal quality and effectively eliminating interference from soot [48, 49, 50]. The advent of femto-second (fs) lasers is particularly important for the continued development of single-shot CARS for turbulent environments [51]. Recent studies (*e.g.*, [51, 52]) have demonstrated the use of a chirped probe pulse to convert fs-CARS into a single laser-shot thermometry technique. High speed thermometry using a hybrid femtosecond/picosecond (fs/ps) CARS approach has also been reported in the literature [53].

Despite these advantages, CARS suffers from a number of disadvantages when applied in turbulent flames. The necessity for line-of-sight optical access and the experimental complexity are the main practical limitations. However, more fundamentally, the beam configuration results in an elongated probe volume. This lack of high spatial fidelity, in comparison to planar techniques, restricts the generic application of CARS [26]. In addition, its reliance on three beams with different optical paths implies that the method is subject to differential beam steering and attenuation in turbulent environments, especially in the presence of soot. Finally, the method has hitherto been limited to single point and no method to extend it to allow planar measurement, as is desirable for investigation of turbulent systems, has been proposed.

### 2.2.3 Laser-Induced Fluorescence

Laser-induced fluorescence (LIF) process is the spontaneous emission from an upper energy level of atoms or molecules that have been simulated with laser radiation. The signal collected from laser-induced fluorescence (LIF) may be spectrally-shifted, thus allowing it to be separated (*i.e.* filtered) from the scattered interference that plagues Raman and Rayleigh scattering. The fluorescence signal is typically quite strong, making LIF better suited to two-dimensional imaging than Raman and Rayleigh techniques [54]. Various strategies exist for LIF-based thermometry, all of which are based upon the species' population distribution over possible energy states according to the Boltzmann equation [24, 55].

The species of excitation can be naturally occurring or artificially seeded. The use of *in situ* species (*e.g.*, OH, CN, CH) for LIF thermometry is limited because of their low concentrations, and the narrow regions within the flame in which they typically exist. Of the naturally occurring species within a flame, the OH radical has been most commonly used [32, 56, 57, 58]. The OH radicals only exist over a small range of temperature and mixture fraction, and exhibits low concentrations in fuel-rich side of the flames. The OH-LIF is therefore not so well suited for general measurements [59]. Furthermore, the OH concentration is low in flames with soot, making it poorly suited to measurements in such flames [60]. Nitric oxide (NO), which is formed natively during the combustion process, could potentially be used for thermometry, though additional NO is typically added to the inlet streams to give a much improved signal quality [32, 61]. However, the excitation wavelengths required for NO (around 226 nm) are susceptible to interference, attenuation and spectral overlap due to pressure broadening of the excitation lines [62]. Furthermore, in fuel-rich flames, NO may be consumed due to reburn reactions, leading to a loss of signal [61, 63, 64]. Background interferences, which cannot be suppressed easily, too can lead to a significant error in the NO-LIF thermometry in the presence of soot [65]. Multi-line approaches has been used for NO thermometry to alleviate issues with background (*e.g.*, [66]), but at the cost of being restricted to averaged results. As an alternative to naturally occurring species, a wide range of seeded species can be introduced.

The accuracy of single-line LIF thermometry relies on the knowledge of the quenching species densities and quenching rate constant, since the spectra and

intensity of the LIF are influenced by the variation in collisional processes across reaction zone. The use of single-line LIF is also limited to systems with homogeneous distribution of seeded species in the observed field [67]. Two-line approach, which involves the utilization of two excitation/detection wavelengths, can be used to circumvent some of the problems associated with single-line LIF technique [54, 68]. Unlike single-line LIF, the two-line techniques allow measurements in systems with inhomogeneous distribution of the number density and the seeded species concentration. The collisional quenching dependencies that are often associated with single-line LIF technique can also be nullified by taking the ratio of the fluorescence signals, in the case where the same excited state or different excited states showing identical behavior in terms of quenching are involved.

A variety of two-line fluorescence techniques have been explored. For simultaneous thermometry and velocimetry, the use of liquid-crystals has been proposed [69]. However, their relevance to turbulent flames are not clear, since they have limited temporal response and do not survive the combustion environment. Two-line phosphorescence using ZnO:Zn and ZnO:Ga has also been reported in literature, with claims of short lifetimes, thus enabling elimination of background interference [70]. Temperature measurements using tracers such as naphthalene [71], acetone [72], 3-pentanone and toluene [67, 73] have also recently been demonstrated. However, the feasibility of these techniques in practical flame environments is yet to be adequately demonstrated.

## 2.3 Two-Line Atomic Fluorescence

The TLAF theory was first evaluated by Alkemade [74], and has subsequently been the interest of other studies (*e.g.*, [29, 59, 75, 76, 77, 78]). The TLAF technique follows the same principle as the other two-line fluorescence techniques, whereby the ratio of two excitation and detection wavelengths is used, but employs an atomic species. The use of atomic species avoids the additional complications associated with the rotational-vibrational structure of the molecular spectra [28, 79].

The basic principle of the TLAF technique involves optical excitation of the two electronic transitional states of the atomic species, and the subsequent detection of the resultant fluorescence emissions. The ratio of the fluorescence signals gives an estimation of the relative populations in the two states, which provides a measure of temperature when in thermal equilibrium [79]. A summary of the many possible detection schemes for the TLAF technique was given by Zizak *et al.* [28], and the linear excitation regime method remains the most widely-investigated approach. Spectrally shifted emissions are also often used for detection, as this enables optical filtering to be used to separate the inelastic fluorescence from interference by spurious scattering [75, 77, 80].

### 2.3.1 Detection Schemes

Different approaches for the implementation of TLAF with Indium have been demonstrated in the literature. These studies typically involved the use of pulsed dye lasers [29, 59, 76, 77] to perform planar imaging. Calibration is required for this approach since two detector systems, with different collection efficiencies, are often employed to facilitate instantaneous imaging. The accuracy of this approach is therefore susceptible to the errors introduced during calibration. Additionally, the method is also limited by the uncertainties associated with the spectral overlap between the laser and the Indium lineshapes that may drift over time, since the spectral linewidths of pulsed dye lasers are typically comparable with the linewidths of the probed Indium transitions [79]. Therefore, this method is not capable of generating data of the accuracy that is required for detailed soot chemical kinetic studies, but is suitable for semi-quantitative imaging.

As a slight variation on the technique, scanning with the use of narrowband tunable laser is also possible. In a such situation, blue extended-cavity diode lasers (ECDLs) with very narrow linewidth and favourable tuneability [79, 81, 82, 83] are typically used to scan over the absorption lines to provide well-resolved Indium spectra. The detected spectra are used to determine the temperature based on a fit of the resultant curve [78, 82, 84]. The scanning approach has the advantage of providing calibration-free single-point measurements with higher accuracy and precision than that achievable with dye lasers, but scanning is not

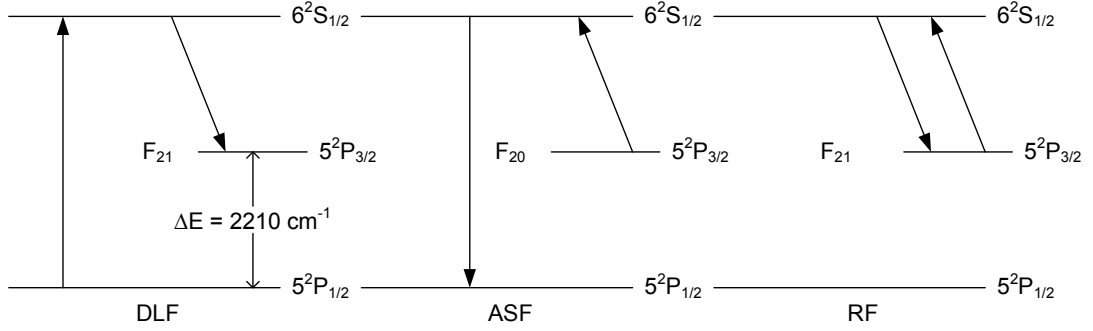


**Figure 2.3:** Schematic diagram of the fluorescence processes for Indium. DLF: direct-line fluorescence. ASF: anti-Stokes fluorescence. RF: Resonance fluorescence. Adapted from [86].

instantaneous and so yields only averaged results.

### 2.3.2 Indium as Seeded Atomic Thermometry Species

Indium has a chemical symbol In and is found in group IIIB of the periodic table. Indium is found in trace amount in many minerals and is typically mined as a by-product during the recovery of major metals, particularly zinc [85]. Indium is often leached from slag and dust from the zinc production, and undergoes further purification via electrolysis. Pure Indium is a soft, lustrous, silvery-white metal that is highly malleable and ductile [85].

Indium has two optically accessible transitions, such as is schematically represented in Figure 2.3, that are sensitive to the temperature range typically encountered in practical combustion systems (800–2800 K) [29]. Additionally, both of the wavelengths involved in the transitions are within the visible spectrum (*viz.* 410 nm and 450 nm), where the interferences are less pronounced than in the UV range.

The large oscillator strength associated with the Indium atom implies that the transitions of the atom are easily saturated. To remain in the linear excitation regime, which is required for the nullification the collisional quenching effects through the ratio of the fluorescence signals (see Section A.1), the laser energy must therefore be limited to low fluences. This leads to weak signal strength,

and so affected by low signal-to-noise ratio (SNR). Time-averaging is therefore typically necessary for TLAf in linear excitation regime.

The seeded Indium species have to undergo the various processes such as desolvation [87] and decomposition prior to the generation of the required neutral Indium atoms (detailed in Section 2.3.3) for TLAf, making the technique limited to measurements above  $\sim 500$  K [88].

### 2.3.3 Transformation of Indium Species

Indium has typically been introduced to the system as Indium Chloride dissolved in solvent when gaseous fuel is used, since the liquid-phase solution of the salt can be easily ‘sprayed’ into most systems with the reactant gas. In order to generate TLAf signal, at least part of the seeded Indium Chloride solution must be converted into free neutral Indium atoms. The conversion of neutral Indium atoms from Indium Chloride solution involves the following steps [87, 89, 90, 91, 92]:

- **Disintegration of the seeding solution:** an aerosol of droplets is formed from the nebulization of the seeding solution.
- **Desolvation of the droplets:** the droplets are heated in the flame whereby the solvent is evaporated to form various Indium complexes. Single ions and molecules are predominantly formed from the desolvation of the droplets with low solute concentration, whilst salt and ion clusters are predominantly formed from the desolvation of droplets with high solute concentration. Neutral or ionized molecules and fragments are subsequently released from the decomposition of the clusters.
- **Gas-phase ion / molecule and anion / cation recombination reactions:** the desolvated ions and molecules undergo different reactions such as electron-ion recombination in the gas-phase to form a variety of species, including neutral Indium atoms, with competing equilibria. These reactions are highly localized within the flame and are dependent on temperature and the chemical reactions within the region [93].

## 2.4 Laser-Based Soot Measurement Techniques

### 2.4.1 Laser-Induced Incandescence

Laser-induced incandescence (LII) has recently emerged as a powerful diagnostic tool for particle concentration and primary particle-size measurements in combustion, particle synthesis, and environmental applications [94]. Although it is now reasonably well established, LII is still a complicated process with many of its details still under investigation [94, 95, 96].

The LII technique involves the rapid laser heating of soot particles to high temperatures (2500–4000 K) that are close to the carbon vaporization temperature [96, 97], and the subsequent detection of the emissions from the laser-heated soot particles. The LII signal can be separated from the background luminosity and interferences with the use of suitable detection scheme [98]. The magnitude of the LII signal is approximately proportional to the soot concentration in the detection region [99], whilst the decay of the signal is correlated to the primary particle size [94].

The LII technique is attractive because it has high temporal and spatial resolution in both point and planar measurements [100], and has been proven to be a useful tool for both qualitative and quantitative measurements [26]. For example, the LII technique has been used to obtain soot concentration measurements in turbulent nonpremixed flames [101, 102]. Henriksen *et al.* [103] have also reported LII measurements in a highly sooty pool fire .

However, the detected LII signal gives only the relative signal of the soot concentration, and therefore must be calibrated via an independent technique that permits the determination of the absolute soot concentration. The calibration of the LII signals can be achieved with the use of *in situ* or *ex situ* methods, such as cavity ring-down spectroscopy (CRDS) [94, 104] and soot gravimetric sampling [105]. Nevertheless, the laser extinction (LE) technique remains the most widely used calibration method.



**Figure 2.4:** Well-characterized calibration flames employed for the calibration of LII measurements. Sooty flames in (left) modified McKenna, (centre) Gülder and (right) Santoro burner from [94].

## 2.4.2 Laser Extinction Measurements

The LE technique, which is commonly used to calibrate the LII technique, is typically performed in well-controlled laminar sooty flames (Figure 2.4). The LE technique is a line-of-sight technique that relies on the measurement of the attenuation of the laser beam by soot. The absolute soot concentration is subsequently inferred from the ratio of the transmitted to the incident light intensity [106], with the use of Bouguer-Lambert-Beer law [107] and soot extinction coefficient ( $K_e$ ) [102, 108]. The LE technique has also been developed to facilitate multi-point measurements by Greenberg and Ku [109], and has since been applied in several studies [110, 111].

The accuracy of the LE technique, however, is primarily limited by the knowledge of the optical properties of the soot particles [106, 108, 112]. Additionally, the necessity for line-of-sight access in addition to the need for spatial and temporal integration restricts the applicability of this technique in combustion systems with steep spatial gradients and short time scales [100].

# Chapter 3

## Experimental Details

This work was undertaken in the Turbulence, Energy and Combustion (TEC) laboratory at The University of Adelaide. A summary of the equipment used during the undertaking of this work is presented in this chapter.

### 3.1 Burners and Seeding Arrangements

A series of well-controlled experimental burners was utilized. Each of the burners produces a reacting medium of different characteristic. The choice of the burner is dependent on the type of flame required for the purpose of the study. This in turn affects the choice of nebulizer and subsequently, the seeding arrangement.

#### 3.1.1 Flat-Flame Burners

Two flat-flame burners were used in this work. These burners were purpose-designed to produce matrices of small laminar premixed flames, which would subsequently interact and combine to form a uniform flame front. Both burners are capable of producing laminar premixed flat-flames that are stable and uniform over a wide range of equivalence ratios, thus allowing comparisons to be made over different flame compositions and temperatures. These burners are well-suited for the validation or calibration of laser measurements [30, 31].

The square flat-flame burner shown in Figure 3.1 has a 50 mm×50 mm burner matrix. The burner face consists of a series of tubes (ID 1.6 mm) that are ~3 mm separated from one another. The burner is 135 mm in length. The burner matrix is encased within a 80 mm×80 mm brass casing to give a channel, which is used to provide co-flow. Flow-conditioning of the co-flow is achieved with the use of stainless steel mesh and layers of glass beads. The cutaway view of the burner is shown in Figure 3.2. This burner was employed in the experiments presented in Chapter 4, Chapter 5, Chapter 6 and Chapter 7. Although the burner is capable of providing flat-flame front conditions for fuel-lean to slightly fuel-rich conditions, non-uniform soot distribution is observed when the burner is operated in richer flame conditions. The spacing between tubes is found to be too far apart to allow the soot, emerging from each of the individual tubes, to interact and coalesce to form a uniform soot sheet. This results in a flame with a ‘stripy’ soot distribution, which can be imaged with laser-induced incandescence (LII) technique, when the burner is operated in very fuel-rich conditions. Independent measurements have verified that this effect does not persist when the burner is operated in soot-free conditions.

The burner was therefore replaced with a circular flat-flame burner, with smaller distance between the burner ports, to generate flames with uniform soot distribution. Such flame conditions are required for the work presented in Chapter 9. The circular flat-flame burner shown in Figure 3.4 consists of a circular ceramic honeycomb matrix with 80 mm diameter. The burner matrix consists of square pores with 1 mm inner length and 1 mm inner width, and 0.25 mm wall thickness. The burner is 240 mm in length. The honeycomb matrix is encased within a brass annular tube with an internal diameter of 80 mm. A second brass annular tube with an internal diameter of 100 mm is aligned to give a co-annular channel, which can be used to provide co-flow. The cutaway view of the burner is shown in Figure 3.4.

### 3.1.2 Jet in Hot Co-flow (JHC) Burner

The jet in hot co-flow (JHC) style burner [113, 114] shown in Figure 3.5 consists of a central fuel jet (OD 20 mm) within an annular co-flow (ID 110 mm). The fuel

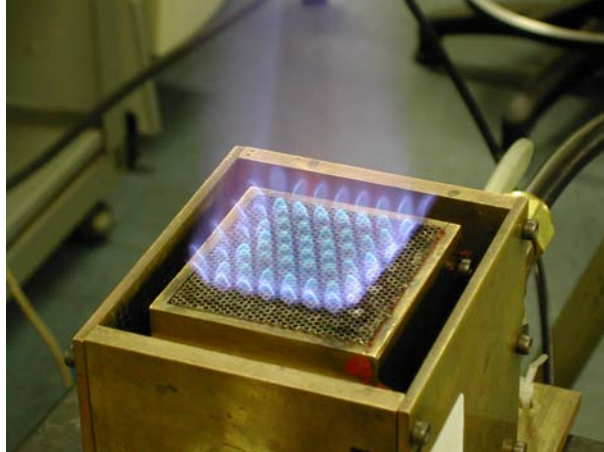


**Figure 3.1:** Photograph of the square flat-flame burner and the premixed flame, here firing natural gas. The burner matrix measures 50 mm×50 mm.

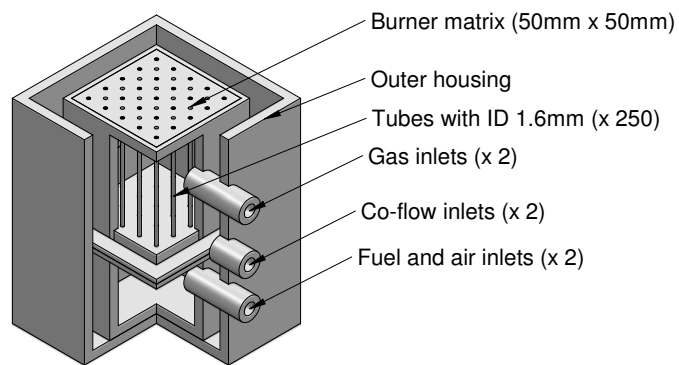


**Figure 3.2:** Cutaway view of the square flat-flame burner. Not all tubes shown.



**Figure 3.3:** Photograph of the circular flat flame burner with a honeycomb matrix. The burner matrix has a diameter of 80 mm and consists of 1 mm×1 mm pores.

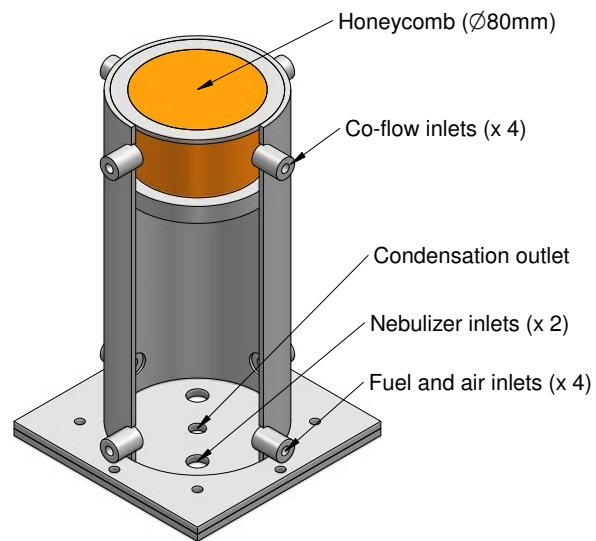


**Figure 3.4:** Cutaway view of the circular flat-flame burner.

jet exit consists of a perforated stainless steel disc with equally-spaced holes (ID 0.8 mm). The fuel pipe is 270 mm in length. A co-flow gas of either nitrogen, air or a premixture of fuel and air can be introduced, depending on the flame conditions of interest. The flow-conditioning of the co-flow gas stream is achieved with the use of stainless steel mesh and layers of flint clay, supported on a perforated plate. The cutaway view of the burner is shown in Figure 3.6. This burner was used to generate laminar nonpremixed flames, as required for the work presented in Chapter 8.

### 3.1.3 Seeding Apparatus

For this work, the Indium has been introduced to the burner systems as Indium Chloride ( $\text{InCl}_3$ ) dissolved in a carrier solvent, since gaseous fuels were used. An indirect nebulization arrangement, where the aerosol is mixed with the combustion gases prior to exiting the burner face, was used to seed Indium into the flames. This configuration provides more uniform seeding than direct nebulization arrangement, where the aerosol is admixed with the combustion gases at the burner face [115].

Indium Chloride salt was dissolved in a solvent, *i.e.* water or organic solvent, and was subsequently nebulized into a mist of droplets. The solvent effects on the Indium fluorescence emission are discussed in Chapter 7. The aerosol was passed through a ballast volume, placed between the nebulizer and the burner, to damp variation in aerosol generation [116]. The ballast volume was also used to filter out the larger droplets and to allow smaller droplets, which will undergo evaporation more readily, to be transported to the flame [87]. The length of the passage used to transport the aerosol from the seeder to the burner was minimized to prevent excessive fallout of the aerosol along the passage. Two types of nebulization methods, namely pneumatic and ultrasonic nebulization, were used in this work.

The pneumatic nebulization utilizes a high velocity gas stream to form an aerosol. The compressed carrier gas streams out from the aperture surrounding the solution capillary resulting in a decrease in pressure at the tip of the capillary. The pressure gradient between the tip of the capillary and the ambient pressure drives



**Figure 3.5:** Photograph of the JHC burner.

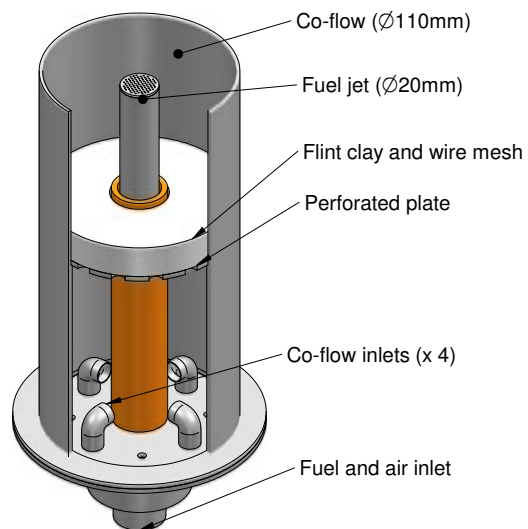


**Figure 3.6:** Cutaway view of the JHC burner.

the seeding solution into, and up, the capillary continuously. The seeding solution, emerging from the tip of the capillary, is subsequently fragmented into an aerosol by the rapidly moving gas streams [115]. The average diameter of the droplets formed is primarily dependent on the carrier gas flow used, and hence the size and the density of the droplets cannot be varied independently [117]. A photograph of a pneumatic nebulizer is shown in Figure 3.7.

Ultrasonic nebulization utilizes a piezoelectric transformer to transform electrical energy into mechanical vibration. The mechanical vibration is transferred through the liquid column, whose energy is derived from the piezoelectric transducer [118], to the liquid-air interface [117, 119]. The efficiency of the transferring of the mechanical vibration energy transfer is therefore dependent on the depth of the liquid column above the device. The constant compression and decompression of the liquid column result in the formation and rupturing of surface waves at the liquid-air boundary. A portion of the wave crests is subsequently ejected from the surface waves as an aerosol [115, 117]. The average diameter of the droplets formed is a function of the surface tension and the density the liquid medium used, as well as the excitation frequency of the nebulizer (Section 7.2.2). A photograph of an ultrasonic nebulizer is shown in Figure 3.8.

The ultrasonic nebulizer possesses a number of attractive characteristics over the pneumatic nebulizer. The ultrasonic nebulizer, unlike the pneumatic nebulizer, is not dependent on a high speed gas stream to form the aerosol [119, 120]. The size and the density of the droplets can therefore be varied independently to suit the characteristic of the burner system used. The ultrasonic nebulizer is also capable of producing an aerosol with droplets of more uniform size distribution and of greater number density when compared with the pneumatic nebulizer [120]. The ultrasonic nebulizer, however, may be susceptible to chemical attack when corrosive seeding solvents are used.

With a view to the aforementioned advantages associated with the ultrasonic nebulizer, the ultrasonic nebulization method is therefore the chosen seeding technique for this work, and was used in the experiments presented in Chapter 4, Chapter 5, Chapter 6, Chapter 7, and Chapter 8. The use of the pneumatic nebulization method as an alternative seeding technique to circumvent the corrosion problem associated with the ultrasonic nebulizer was demonstrated in Chapter 9.



**Figure 3.7:** Photograph of the pneumatic nebulizer. Adapted from [121].



**Figure 3.8:** Photograph of the ultrasonic nebulizer.

## 3.2 Laser Systems

Three laser systems were used to measure the temperature and soot volume fraction distribution within the flames. Two lasers formed part of the two-line atomic fluorescence (TLAF) system, and another laser was used for LII.

### 3.2.1 Two-Line Atomic Fluorescence Laser System

#### 3.2.1.1 Laser System for 410.18 nm Beam

A pulsed tunable dye laser was used to generate the 410.18 nm wavelength light required to probe the  $5^2P_{\frac{1}{2}} \rightarrow 6^2S_{\frac{1}{2}}$  transition of Indium (Figure 2.3). A Quantel TDL 90 dye laser was pumped at 532 nm with a frequency-doubled Q-Switched YG980 Nd:YAG laser. Using a mixture of that consists of Pyridine 1 and DCM laser dyes, the  $\sim 667$  nm output of the dye laser was frequency-mixed with 1064 nm light from the YG 980 Nd:YAG laser with line-narrowing etalon, using a mixing unit extension to obtain the required  $\sim 410$  nm. The output was passed through a Pellin-Broca prism to isolate the desired wavelength. The maximum measured output power was  $\sim 22$  mJ/pulse. The linewidth of the laser was measured using a Burleigh WA-5500 UV-pulsed wavemeter and was found to be  $0.4 \text{ cm}^{-1}$ . It is worth noting that the beam expansion unit within the cavity of the dye laser was removed to increase the linewidth of the laser, and thus ensuring a good spectral overlap between the laser output and the Indium lineshape.

#### 3.2.1.2 Laser System for 451.13 nm Beam

A pulsed tunable dye laser was used to generate the 451.13 nm wavelength light required to probe the  $5^2P_{\frac{3}{2}} \rightarrow 6^2S_{\frac{1}{2}}$  transition of Indium (Figure 2.3). A Quantel TDL 90 dye laser was pumped at 355 nm with a frequency-mixed Q-Switched Quantel Brilliant B Nd:YAG laser. The dye used is a mixture of Coumarin 450 and Coumarin 460. The maximum measured output power was  $\sim 16$  mJ/pulse. The linewidth of the laser was measured using a Burleigh WA-5500 UV-pulsed wavemeter and was found to be  $0.3 \text{ cm}^{-1}$ . The beam expansion unit within the cavity of the dye laser was also removed to increase the linewidth of the laser, and

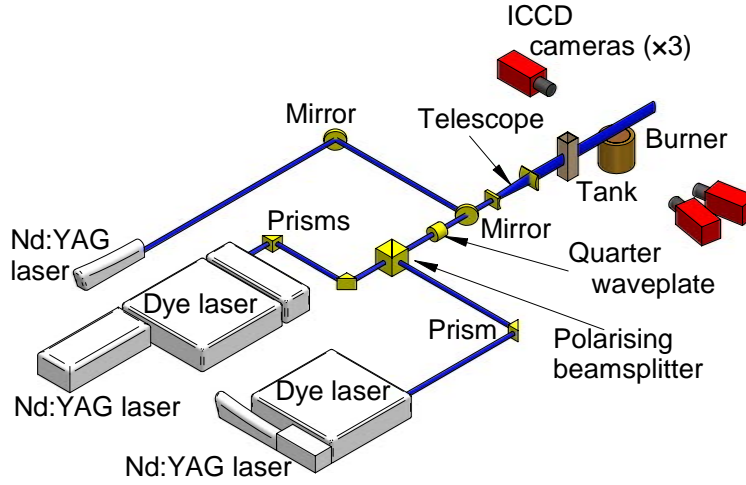


**Figure 3.9:** Pictorial representation of experimental layout.

thus ensuring a good spectral overlap between the laser output and the Indium lineshape

### 3.2.2 Laser-Induced Incandescence Laser System

The 1064 nm output from a Q-switched Quantel Brilliant B Nd:YAG laser was used to generate the LII images required for soot volume fraction measurements. Although this is a double-headed laser, only the master head was used. Also, the doubling unit extension was removed. The maximum measured output power was  $\sim 700$  mJ/pulse at 1064 nm.

## 3.3 Experimental Layout

### 3.3.1 Optical Layout

Figure 3.9 shows diagrammatically the experimental layout which was used for simultaneous TLAF and LII measurements. This setup was used in all of the experiments, with the exception that modifications were made to the cylindrical telescope to change the height and thickness of the laser sheets to accommodate

differing requirements for different experiment configurations. Also, the Nd:YAG laser, mirrors and camera which were used for the generation and detection of LII signals were removed when the LII measurements were not required.

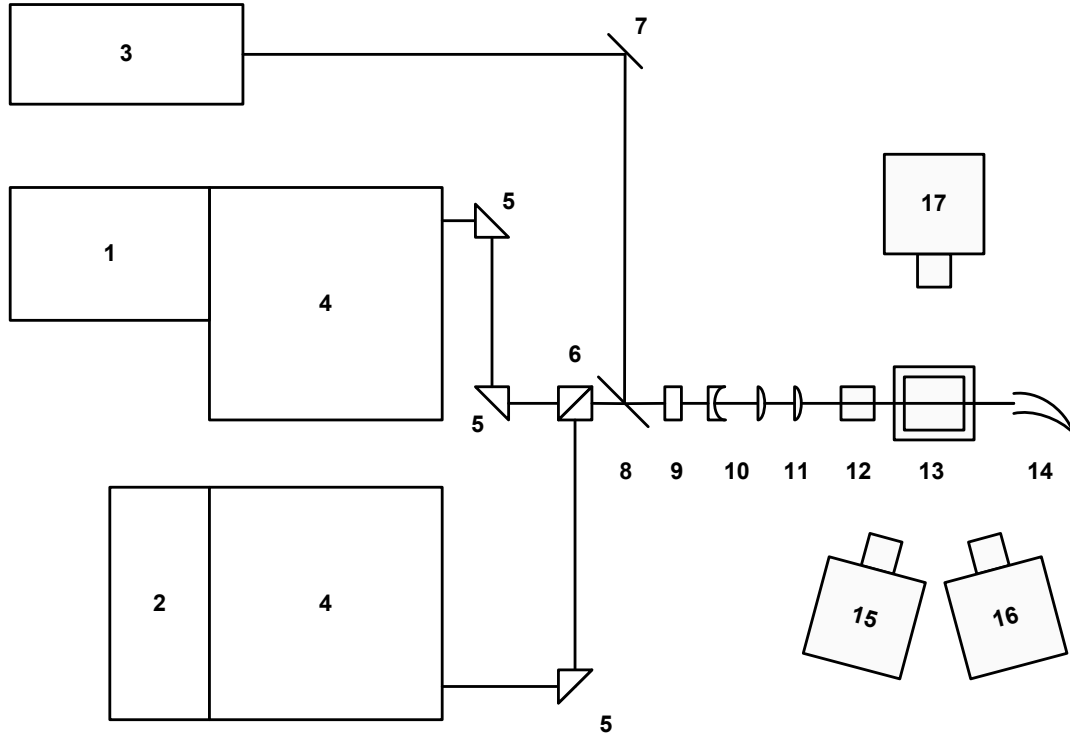
For the TLAF measurements, two Nd:YAG pumped dye lasers were tuned to 410.18 nm and 451.13 nm respectively. The laser pulses were fired sequentially to reduce interference on the other systems. Using the difference in polarisation, the 410 nm and 450 nm beams were combined, converted to circular polarisation, and shaped into co-planar sheets. Circular polarisation was favored to prevent bias in the detected signal due to the difference in linear polarisation orientation of the beams. The laser sheets were directed through a transparent tank, which was filled with fluorescing dye, in the same field of view as the burner. The frequency-shifted emissions from both the tank and the flame were detected through 450 nm and 410 nm optical filters (both with 10 nm bandwidth), using Nikon f<sub>#</sub>1.4 lenses, onto two Princeton Instruments intensified CCD (ICCD) cameras. The gate widths of the cameras were set to 50 ns. The timings of the cameras were set to be prompt with the corresponding laser excitation.

For the LII measurements, an Nd:YAG laser operating at 1064 nm was used for the LII excitation. A 2" high energy 1064 nm mirror was used as a dichroic filter. The 1064 nm laser beam shared the same optical pathway as the TLAF process. The lenses used were not achromatic, leading to a slight difference in the focal length, though insignificant over the region of interest through the flame. The wings of the sheet exhibiting lower laser fluence were clipped with a rectangular aperture. The LII signal was detected through a 410 nm optical filter (10 nm bandwidth), using a Nikon f<sub>#</sub>1.4 lens, onto another Princeton Instruments ICCD camera. The gate width of the camera was set to 100 ns and the timing was set to be prompt to the LII excitation process. This timing scheme was selected to reduce the size-dependent sensitivity of the signal [122].

Figure 3.10 shows the details of the optical layout.

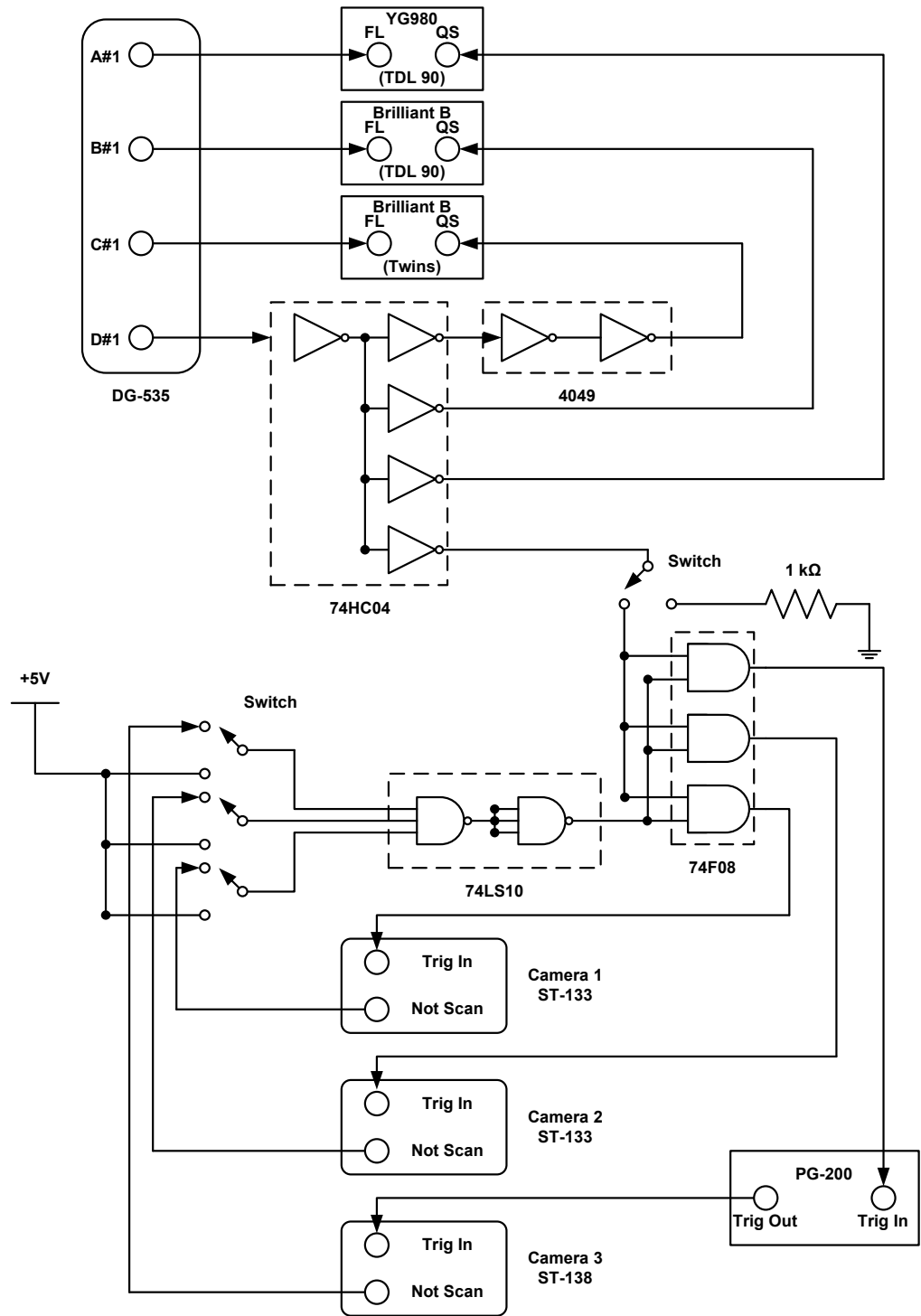
### 3.3.2 Timing Details

Figure 3.11 presents the electronic setup that was used to synchronize the laser and camera systems for simultaneous TLAF and LII measurements. The laser



- 1) Nd:YAG laser (Quantel YG980)
- 2) Nd:YAG laser (Quantel BrilliantB)
- 3) Single-head Nd:YAG laser (Quantel BrilliantB Twins)
- 4) Dye laser (Quantel TDL90)
- 5) Prism
- 6) Broadband polarizing cube beam splitter
- 7) 1" high energy 1064 nm mirror
- 8) 2" high energy 1064 nm mirror
- 9) Achromatic zero-order quarter wave plate
- 10) Cylindrical lens telescope (vertical axis)
- 11) Cylindrical lens (Horizontal axis)
- 12) Dye tank
- 13) Burner
- 14) Beam dump
- 15) ICCD camera (Princeton Instruments, 7467-0004),  $f_{\#}1.4$  lens (Nikon) & 410 nm filter
- 16) ICCD camera (Princeton Instruments, 7361-0001),  $f_{\#}1.4$  lens (Nikon) & 450 nm filter
- 17) ICCD camera (Princeton Instruments, ICCD-575-G/1),  $f_{\#}1.4$  lens (Nikon) & 410 nm filter

**Figure 3.10:** Schematic details of experimental layout.



**Figure 3.11:** Timing details for the lasers and the detection systems for simultaneous TLAF/LII.

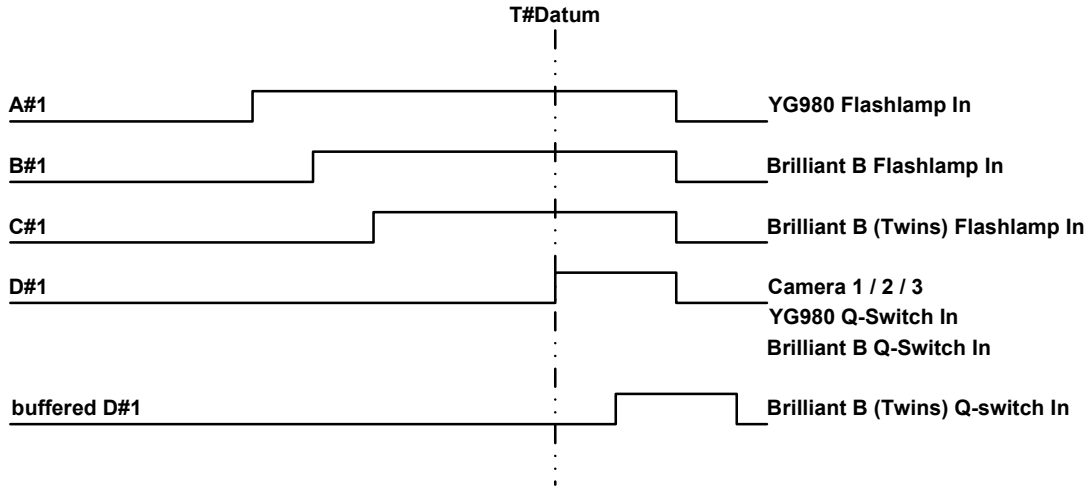


**Figure 3.12:** Timing diagram for simultaneous TLAF/LII. Not to scale.

and camera systems involved in the generation and collection of LII signals, namely Camera 3 and Brilliant B (Twins), were disconnected from the setup when the LII measurements were not required.

A centralized timing system, which consisted of a DG-535 Stanford Research Systems pulse/delay generator and some minor logic gates, was used to synchronize the lasers, the detection systems, and the controlling computers. The electronic setup used to synchronize the devices is shown in Figure 3.11. A fully externally triggered mode has been chosen to attain the required control.

The DG-535 Stanford Research Systems pulse/delay generator generates a continuous 10 Hz signal. The signals from the A#1, B#1 and C#1 terminal of the pulse generator were used to drive the flashlamps of the lasers. The signal from the remaining terminal of the pulse generator, namely D#1, was used to trigger the firing of the Q-switches for all of the lasers. The buffered signals from the D#1 terminal were delayed by exploiting the propagation delay or with the use of logic gate 4049, depending on the configuration of the laser systems involved, to control the firing sequences of the lasers. The firing of the flashlamps was set to occur before the firing of the corresponding Q-switches. The delay between each of the firing of the flashlamps and the Q-switches was varied, using DG-535, to control the output power of the corresponding laser.

The signal from the D#1 terminal was also used to trigger the camera controllers as well. Two different camera controllers (ST-133 and ST-138) were used and hence slightly different timing arrangements were required. The ST-133 controller has the intensifier and camera controllers integrated into one single compact unit whereas the ST-138 controller consists of the camera controller only. A separate high-voltage controller (PG-200) was therefore needed, in combination with the ST-138 controller, to trigger the intensifier of the corresponding camera. Each of the intensifier controllers features an internal delay (gate delay), which governs the delay between the arrival of the trigger signal at the input terminal of the controller and the actual triggering of the intensifier. The gate delay was adjusted to match the triggering of the intensifier with the arrival of the corresponding laser pulse.

All three cameras feature a combined intensifier and CCD arrays within a single camera head. The exposure times (gate widths) of the CCD arrays were kept at 50 ns and 100 ns for the TLAf and the LII laser systems, respectively, to minimize flame luminosity from interfering with the recorded image.

It is important that light must not be allowed to fall on the CCD arrays while the data was transferred from the camera to the host computer (readout), as this would corrupt both the existing and the new image. The signals from the NOT SCAN terminals of the camera controllers were therefore tied together as single line, to inhibit the triggering of the intensifier and the subsequent reading of the CCD arrays, whilst the readout processes were taking place.

There were three switches at the input of the logic gate 74LS10, as shown in Figure 3.11. These switches were used for preliminary testing and were not used during experimentation. Also, an additional switch was included at the input of the logic gate 74F08 as seen in the figure. This switch was to be used to ensure that all cameras were triggered to record at the same pulse.

The relative timing sequences of the devices are depicted in Figure 3.12.

## 3.4 Data Processing

The data processing comprises of image matching and corrections for background, dark-charge, detector attenuation, and laser power and profile. The general data processing steps involved are depicted in Figure 3.13. The details are discussed in the following sections.

### 3.4.1 Image Matching

Image matching is a process to correct for the misalignment of the cameras and thus ensuring that the images overlap. A transparent target with grid and numbering was imaged using the cameras at the beginning of the experiment. This transparent grid image forms the basis of the image matching and morphing procedures. By identifying a set of unique control points on the images of the transparent grid, recorded on all cameras, the control points of the ‘input’ images were mapped onto the control points of the ‘base’ image using a four-point projective transformation algorithm in MATLAB<sup>®</sup> 7 Image Processing Toolbox (Version 4.2). These images were further morphed, to ensure sub-pixel spatial matching of the images, with the use of an in-house image processing software. The image recorded on the camera that has the lowest spatial resolution was selected as the ‘base’ image, whilst the images from the remaining cameras were the ‘input’ images.

### 3.4.2 Background and Dark-Charge Corrections

Background and dark-charge corrections ensure that the data images collected are independent of the extraneous signal due to background noise and/or dark-charge from the CCD arrays. A background image was first recorded with the flame on and the laser blocked, so that any signal detected was due to non-laser sources. Similarly, another background image was also recorded with the flame extinguished and the laser firing. However, because of the very short gate width used for the ICCD cameras, the images recorded were observed to be entirely comprised of CCD dark-charge. Therefore, only the CCD dark-charge image was

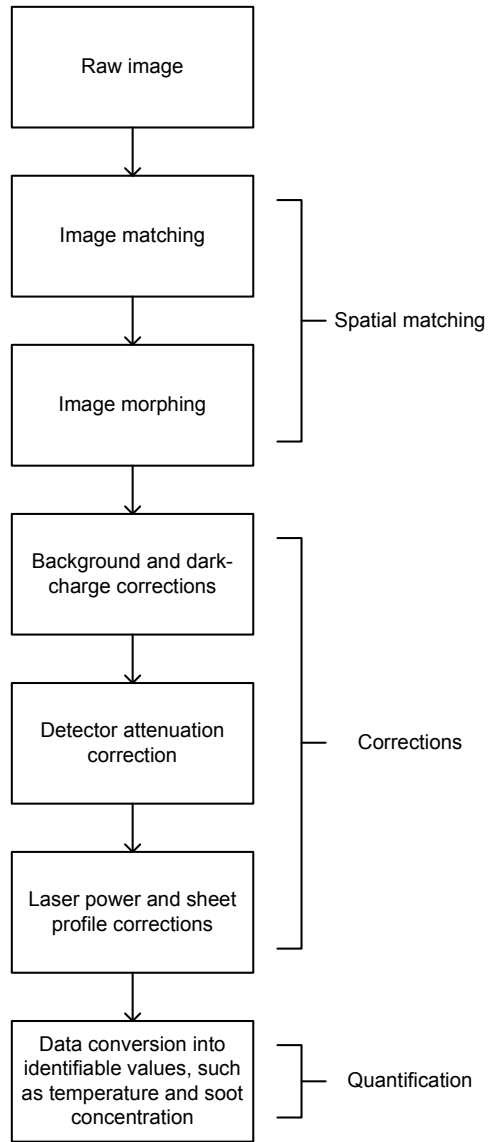


**Figure 3.13:** General data processing steps.

required to be subtracted from all of the data images recorded. Also, the first ten images of the data sets were discarded to ensure that the residual signals on the CCD arrays do not corrupt the rest of the data collected.

### **3.4.3 Detector Attenuation Correction**

Detector attenuation correction is a process to correct for the reduction of the brightness at the periphery, as compared with the centre of the images, due to the vignetting effect of the detection optics. A uniformly illuminated target was first imaged to give spatial intensity information that is required to account for the non-uniform light response over the entire image. The data images were subsequently normalized by the target image.

### **3.4.4 Laser Power and Profile Corrections**

The laser sheets from the dye lasers were first directed through a tank, which was filled with a fluorescing dye (Stilbene 420 in methanol) and placed in the same field of view as the burner. The fluorescence from the tank was subsequently used to give information on the power and energy distribution of the laser sheets. This information was used to rectify the variations in the power and profile of the dye lasers outputs between pulses, on a shot-by-shot basis, thereby reducing these effects on the data images.

## **3.5 General Error Sources**

The potential sources of errors that were typically encountered in all of the experiments are discussed in the proceeding sections.

### **3.5.1 Flow Meters**

The gas flows were metered using tube and float type flow meters. The flow meters were quoted to have an accuracy of 2% with a repeatability of 0.5%, both

at full-scale reading [123]. The actual flowmeter errors introduced, however, were greater than the quoted value since it was not always possible to operate the flow meters at full-scale.

The flow meters were also regulated with pressure gauges. The use of the pressure gauges led to the introduction of additional errors, which were expected to be of similar order as the flow meters. The combined errors from both the flow meters and the pressure gauges affected the overall accuracy and the repeatability of the flame conditions.

### 3.5.2 Dye Lasers

This work involves the utilization of two pulsed dye lasers for excitation. The beam expansion units of the dye laser were removed to give laser outputs with linewidths of  $0.4\text{ cm}^{-1}$  and  $0.3\text{ cm}^{-1}$  for the 410.18 nm and 451.13 nm laser systems, respectively. This is to ensure good spectral overlap between the linewidths of the lasers and the Indium lineshapes. The spectral linewidths of the pulsed dye lasers are now comparable to the linewidths of the probed Indium transitions, which are approximated to be  $0.66\text{ cm}^{-1}$  and  $0.40\text{ cm}^{-1}$  [124] for the  $5^2\text{P}_{\frac{1}{2}} \rightarrow 6^2\text{S}_{\frac{1}{2}}$  and  $5^2\text{P}_{\frac{3}{2}} \rightarrow 6^2\text{S}_{\frac{1}{2}}$  processes, respectively. Nonetheless, the spectral overlap issues are also inherently dealt with in the TLAF theory and experimental calibration procedures, as outlined in the subsequent chapters.

The spectral overlap between the laser and Indium lineshapes may also drift over time, thereby result in unaccountable systematic error. A calibrated Burleigh WA-5500 UV-pulsed wavemeter was also used to measure the wavelengths of the outputs from the dye lasers periodically. The wavelengths of the lasers were found to be relatively stable and hence, no regular adjustment was needed. Additionally, the dye lasers were tuned on- and off-resonance regularly, in addition to wavelength scans, to verify that the excitations occur at the expected peak locations.

### 3.5.3 Seeding

The seeding of the Indium into the flame constitutes an essential component of the TLAFF technique. In this work, the Indium was introduced to the flame as Indium Chloride dissolved in solvent. An ultrasonic nebulizer (Aquapro, DH-24B) or a pneumatic nebulizer (Glass Expansion) was used to fragmentate the seeding solution into aerosol. The mist of droplets was subsequently fed into the flame, whereby neutral Indium atoms were generated within the flame front. Inaccuracies in the seeding rate of the would lead to differences in the gas compositions, thus affecting the overall accuracy and the repeatability of the experimental conditions. It is worth noting that the variation of the seeding rate into the flame does not affect the accuracy of the TLAFF technique, since the TLAFF temperature measurements are deduced from the ratio of the Indium fluorescence, rather than the actual number of the neutral Indium atoms present within the measurement volume.

The nebulization rate of the ultrasonic nebulizer (the chosen seeding method for this work) is dependent on several parameters, one of which is the depth of the liquid column above the device (Section 3.1). The depth of the liquid column affects the transferring of the mechanical vibration energy from the nebulizer, through the column, to the liquid-air boundary. Any variation in the depth of the liquid column would therefore influence the formation and rupturing of the surface waves at the boundary, and the subsequent ejection of the resulting wave crests as aerosol. An automated feed was thus installed to maintain a constant level of the seeding solution above the nebulizer. The ultrasonic nebulizer was also found to be susceptible to chemical attacks from the seeding solution, which resulted in the deterioration of the performance of the device over time. The nebulizer was therefore cleansed after each experiment run, and replaced after each campaign.

Despite these issues, the seeding rate of the Indium Chloride into the flame was found to be reasonably invariant over the duration at which the measurements for a single set of experiment were conducted. At most, the errors in the seeding rate were estimated to be  $\sim 10\%$ .

### **3.5.4 Measurements Errors**

Whilst care was taken to ensure that the measurements from the experimental apparatus were accurate, there were inevitably potential for slight inaccuracies during the reading and the recording of the values from these devices. Different runs of the experiments were conducted to identify and isolate measurements that were found to display apparent discrepancies with the general trends.

### **3.5.5 Processing Parameters**

The general processing structure is outlined in Section 3.4. The processing of the data required the determination of several parameters. Whilst systematic approaches were adopted during the determination of these parameters, there was potential for slight inaccuracies during the selection of these values, which would subsequently lead to the generation of erroneous processed data. Extra care was taken to ensure that these selected values gave accurate representation the required parameters.

This page intentionally left blank.

# Chapter 4

## Linear Two-Line Atomic Fluorescence (TLAF)

In this chapter, the capability of the two-line atomic fluorescence (TLAF) technique in the linear excitation regime to provide single-shot temperature imaging is assessed.

### 4.1 Introduction

Previous TLAF theory has been limited to low laser fluence, whereby the relationship between the excitation fluence and the resulting fluorescence signal is linear (*e.g.* [59, 76, 77]). Under such condition, the signal is plagued by low signal-to-noise ratio (SNR) [28].

The capability of TLAF technique in the linear excitation regime, to provide single-shot temperature image, is assessed in this chapter. Instantaneous and averaged fluorescence and temperature images obtained using linear TLAF are presented and compared. These images serve as necessary references for measurements in the subsequent chapters.

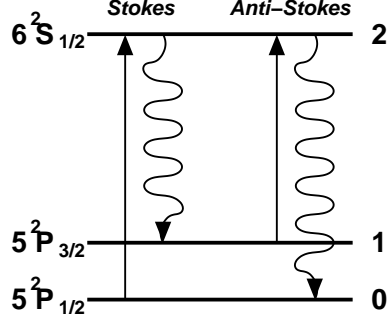


**Figure 4.1:** Energy transitions involved in the TLAF process.

## 4.2 Methodology

The TLAF arrangement of interest for this dissertation involves the sequentially shifted measurements of Stokes and anti-Stokes direct-line fluorescence of a three-level system, namely the Indium atom. The three energy levels of a neutral Indium atom that are relevant to TLAF are shown diagrammatically in Figure 4.1.

The Stokes process involves 410.18 nm laser excitation ( $5^2P_{1/2} \rightarrow 6^2S_{1/2}$  transition), and the subsequent fluorescence ( $6^2S_{1/2} \rightarrow 5^2P_{3/2}$  transition) is detected at 451.13 nm. The anti-Stokes process uses 451.13 nm excitation ( $5^2P_{3/2} \rightarrow 6^2S_{1/2}$  transition) and 410.18 nm detection ( $6^2S_{1/2} \rightarrow 5^2P_{1/2}$  transition) [125].

By introducing a small time delay (of the order of 100 ns) between the two excitation pulses, in conjunction with optical filtering, the Stokes fluorescence detected at 451.13 nm is essentially immune from spurious scatter from the anti-Stokes excitation at that same wavelength. The same applies for the 410.18 nm Stokes excitation and anti-Stokes emission. By both temporal and spectral shifting the Stokes and anti-Stokes processes, measurements in sooting conditions are potentially feasible. The flame temperature is subsequently deduced from the ratio of these fluorescence signals.

Following the derivations given in Appendix A, it can be shown that by rearranging the rate equations for each energy level, and applying the Boltzmann function [24, 55], the temperature expression in the linear excitation regime is given by [76],

$$T = \frac{\Delta E_{10}/k}{\ln\left(\frac{F_{21}}{I_{02}}\right) - \ln\left(\frac{F_{20}}{I_{12}}\right) + 4\ln\left(\frac{\lambda_{21}}{\lambda_{20}}\right) + C_t} . \quad (4.1)$$

Here  $\Delta E$  is the energy difference between the energy levels,  $F$  is the fluorescence,  $I$  is the laser spectral irradiance, and  $\lambda$  is the wavelength.  $C_t$  is a constant that is dependent on a number of experimental factors, such as collection efficiency, and is best determined from experimental calibration. The subscripts refer to the transition between the energy levels, as shown in Figure 4.1. Experimental calibration has the advantage of eliminating the need for accurate quantification of numerous experimental factors, such as laser linewidth and collection efficiency [76].

## 4.3 Experimental Arrangement

### 4.3.1 Burner and Seeding Arrangement

For the assessment of the linear TLA method, the square flat-flame burner was used to generate laminar premixed flames to avoid the complexities associated with turbulent and/or nonpremixed flames. The details of the burner and a photograph of the burner firing natural gas-air premixed flame are provided in Section 3.1.1. In brief, the burner consists of a series of tubes forming a 50 mm square cross section. The burner was fuelled with a premixture of natural gas ( $\geq 92\%$  vol.  $\text{CH}_4$ ), air and nitrogen.

The seeder consisted of an ultrasonic nebulizer, which generated a mist of 5  $\mu\text{m}$  diameter droplets of Indium Chloride dissolved in distilled water. A concentration of 1.5 mg/mL of the Indium Chloride in distilled water was used (Section 4.4.2). The result is  $\sim 1.2$  mg/min of Indium Chloride, which is  $\sim 40$  ppm (mass basis) of Indium Chloride in the flame. Nitrogen was used as a carrier gas to facilitate the seeding of Indium into the flame.

The conditions of the two premixed flames used are shown in Table 4.1. The equivalence ratios ( $\Phi$ ) of the flames were adjusted by varying the fuel flow rate to a constant oxidant flow rate. This is to maintain a similar volumetric flowrate

Flame number	Equivalence ratio ( $\Phi$ )	% N <sub>2</sub> (vol/vol)	Bulk velocity (m/s)	Thermocouple reading (K)
1	1.5	18	0.17	1803
2	1.2	14	0.23	2004

**Table 4.1:** Premixed flat-flame conditions.

and thus similar seeded Indium concentration. It is worth noting that the % N<sub>2</sub> in the table refers to the percentage of the additional N<sub>2</sub> in the premixed steam due to the seeding process.

### 4.3.2 Optical Setup

The experimental arrangement in this study is similar in most aspects to the setup depicted in Figure 3.9, with the exception of the removal of the Nd:YAG laser, mirror and the camera used for the generation and the detection LII signals. In brief, the beams from the two Nd:YAG-pumped dye lasers, fired with  $\sim 100$  ns separation, were shaped into co-planar sheets of 45 mm height and  $\sim 4.5$  mm thickness. A thick light sheet was used to give an improved SNR and was sufficient for the current laminar flat-flames.

Each of the images presented in this chapter has been spatially matched and corrected for background and detector attenuation, as detailed in Section 3.4. The in-plane spatial resolution of the matched images is  $\sim 375$   $\mu\text{m}$  per pixel, in each direction. Measurements were conducted 20 mm above the burner face to provide a uniform thermal field away from any interference from the burner. All data are extracted from the central region, where the Indium fluorescence is most uniform.

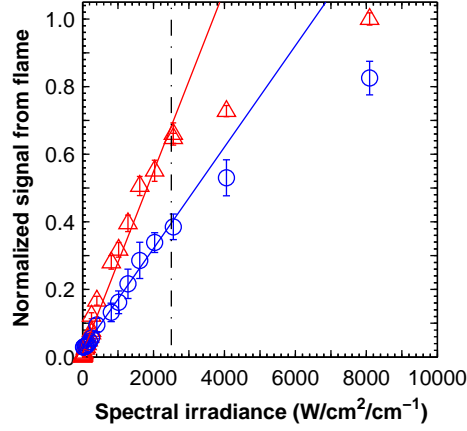


**Figure 4.2:** Indium fluorescence as a function of spectral intensity in the linear fluence regime. The fluorescence signals are normalized to the local maximum values. Open circles: Stokes. Open triangles: anti-Stokes.

## 4.4 Results and Discussion

### 4.4.1 Linear Fluence

The SNR (defined as the ratio of the signal intensity to the inter-pixel noise) of the Indium fluorescence images is dependent on the laser energy used. In the linear excitation regime, the amount of the fluorescence signal obtained is proportional to the amount of incident laser energy. The linear regime, however, has a finite limit beyond which the fluorescence signal deviates from the linear regime. It is therefore necessary to identify the maximum fluence at which the lasers can be operated, and hence optimum SNR achievable, whilst remaining within the linear excitation regime.

To determine the maximum fluence before deviation from the linear regime, the Indium fluorescence is plotted against the excitation energy for both excitation schemes. The laser energy was varied here by the addition of neutral density (ND) filters of differing optical density. This approach maintains consistent optical properties of the laser while changing the fluence. The flame condition and the Indium seeding concentration ( $\sim 1.5$  mg/mL) were held constant.

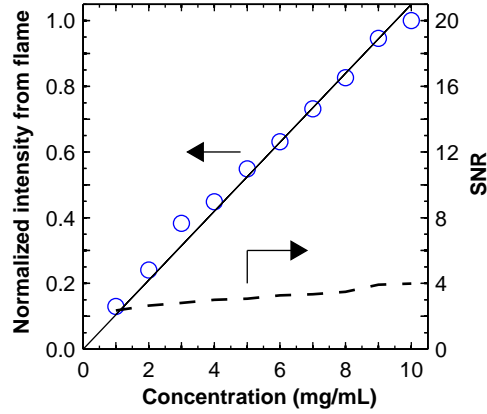


**Figure 4.3:** Indium fluorescence as a function of Indium Chloride concentration. The fluorescence signals are normalized to the local maximum values. Stokes.

Figure 4.2 presents the 200-shot averaged of both Stokes and anti-Stokes Indium fluorescence obtained for Flame 1 (Table 4.1), for various laser energies and thus spectral irradiances. Also included on this plot is the standard deviation with respect to the mean for each point. It is apparent that the fluorescence is linear for a laser energy of up to  $2500 \text{ W/cm}^2/\text{cm}^{-1}$ , beyond which a nonlinear behaviour is detected. A spectral irradiance of  $\sim 3000 \text{ W/cm}^2/\text{cm}^{-1}$  has previously been indicated to be in the linear excitation regime [59, 77], consistent with the current validation.

#### 4.4.2 Seeding Concentration

The fluorescence signal is dependent on the number of neutral Indium atoms present in the measurement volume. For the TLAF theory to apply, it is necessary to verify that the fluorescence is linear with the concentration of Indium. Figure 4.3 presents the fluorescence intensity as a function of the concentration of Indium Chloride in the seeding solution. The Indium Chloride concentration is assumed to be directly proportional to the number of neutral Indium atoms within the flame itself. Shown in Figure 4.3 is both the normalized and the SNR of the fluorescence intensity over a 100-shot data set.

Figure 4.3 demonstrates that, for the current seeding arrangement, the behaviour of the fluorescence is linear up to a concentration of  $10 \text{ mg/mL}$ . Of particular note

is that, despite an increase in normalized fluorescence with higher concentration, no significant improvement in the SNR of the fluorescence is observed. This results in there being no significant improvement in the SNR with increasing concentration of Indium.

It is advantageous to minimize the seeding concentration because it has previously been indicated that the presence of metal additives within a flame environment can influence the soot formation process [126]. Although global flame properties remain unaffected, metal ions when present in sufficient quantity, could inhibit coagulation of soot particles [127], leading to a greater number of small particles and thus to a higher oxidation rate [128]. For low to moderate seeding concentrations, it has been shown using LII measurements that, within experimental uncertainty, the inclusion of Indium does not affect the soot volume fraction [59]. For the remainder of the experimental results presented, a concentration of  $\sim 1.5$  mg/mL is used to ensure linear behaviour with concentration whilst minimizing the effect of Indium on the flame properties.

Providing the Indium concentration is sufficient to yield good signal, precise determination of the concentration is not overly important since the measurement of temperature using the TLAF theory is independent of the Indium concentration. Thermocouple measurements confirm that the inclusion of Indium into the flame has a negligible influence on the flame temperature itself, which is below measurable limits.

### 4.4.3 Temperature Calibration

As described in Section 4.2, to determine temperature from TLAF requires the evaluation of a calibration constant. Thus, a reference temperature is required using an independent technique. Here, an R-type thermocouple, with a bead diameter of 0.7 mm, was used as the primary reference. The measured thermocouple temperature was corrected for radiation by applying an energy balance to the junction [21] (Appendix B). To validate the thermocouple measurement, temperature was also measured using Rayleigh scattering and compared with adiabatic equilibrium calculations. The results of the independently derived maximum temperature obtained for a premixed natural gas/air flame are shown in

Technique	Max. temp
Adiabatic equilibrium calculations	2232K
Thermocouple (after radiation correction)	2204K
Rayleigh scattering	2211K

**Table 4.2:** Maximum temperature measurements and calculations for a premixed natural gas/air flame.

Table 4.2. The two measured values agree within  $\sim 10$  K. The calculated value agrees with the measured values to  $\lesssim 30$  K. This difference in temperature is expected due to radiative heat loss from the flame, which is not accounted for in the adiabatic equilibrium calculations.

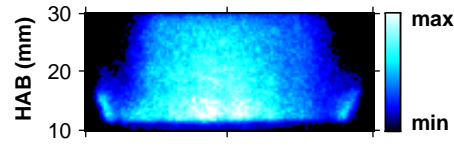
#### 4.4.4 Typical Instantaneous Images

Figure 4.4(a) and Figure 4.4(b) show typical instantaneous images of the Stokes and anti-Stokes Indium fluorescence recorded simultaneously under a low spectral irradiance of approximately  $2500 \text{ W/cm}^2/\text{cm}^{-1}$ . The images represent an area 20 mm high and 50 mm wide, centred 20 mm height above burner (HAB).

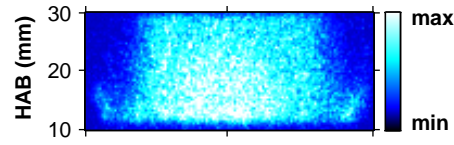
Both the Stokes and anti-Stokes images show a gradient in the Indium fluorescence across the width of the flame. An independent measurement of temperature suggests that the thermal field across the measurement volume is essentially constant. The variation in signal is attributed to a variation in the concentration of neutral Indium atoms throughout the burner. The non-uniformity of Indium atoms is believed to be due to a combination of non-uniform seeding and the process by which the Indium atoms are formed from the Indium Chloride solution. In the context of TLAF, such a difference in concentration only influences the absolute signal and not the deduced temperature. As can be seen in these images, the non-uniformity affects both the Stokes and anti-Stokes fluorescence, thus the differences cancel out in the temperature expression.

The flame presented in Figure 4.4 has a  $\Phi$  of  $\sim 1.5$ , which favours strong Indium fluorescence. Previous studies (*e.g.*, [77]) have also shown that fuel-rich conditions provide the optimal environment for maximizing Indium signal. An increase in signal under fuel-rich conditions is attributed to the reducing environment that

(a) Stokes



(b) Anti-Stokes



(c) Temperature

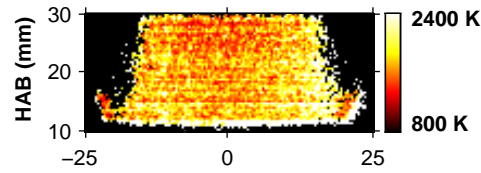


**Figure 4.4:** Typical instantaneous images of (a) Stokes, (b) anti-Stokes Indium fluorescence and (c) temperature in Flame 1 (Table 4.1). Linear fluence excitation ( $2500 \text{ W/cm}^2/\text{cm}^{-1}$ ). Laser propagation from left to right. HAB, height above burner. Dimensions of images in mm.

is necessary for the conversion of the Indium Chloride salt to neutral Indium atoms [29]. The formation of neutral Indium is believed to involve electron-ion recombination and molecular dissociation, though the exact process by which the atoms are produced is complex and unclear [87]. Despite near-optimal flame conditions, the SNR of the instantaneous fluorescence images in Figure 4.4 is  $\sim 18:1$  for the Stokes, and only  $\sim 5:1$  for the anti-Stokes.

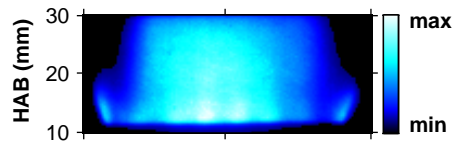
From the combination of the instantaneous images presented in Figure 4.4(a) and Figure 4.4(b), the TLAf equation (Equation 4.1), and the calibrated thermocouple temperature, the temperature distribution throughout the image has been calculated in Figure 4.4(c). The calibration constant was determined by ‘forcing’ the mean temperature of the averaged images to match the radiation-corrected thermocouple reading at one point of the flow [76]. This calibration method limits the TLAf accuracy to that of a thermocouple (here  $\pm 30\text{K}$ ), but does not affect the precision of the technique. Determination of the  $C_t$  term in Equation 4.1 via calibration is preferred over trying to estimate the necessary terms that are grouped into the constant. Experimental calibration eliminates the need for accurate quantification of numerous experimental factors, such as laser linewidth, collection efficiency and seed concentration [76].

Since the calibration constant was chosen based on this particular flame condition, the measurement temperature necessarily agrees with the thermocouple measurement. Nevertheless, the almost uniform temperature distribution appearance, with a slight increase towards the edges of the flame, follows the same trend of that measured using the thermocouple probe. The high apparent temperature and gradient at the edges of the flame is a result of the paucity of Indium in the surrounding air. The SNR of the deduced temperature image is  $\sim 8:1$ , corresponding to a precision of  $\sim 250\text{ K}$ .

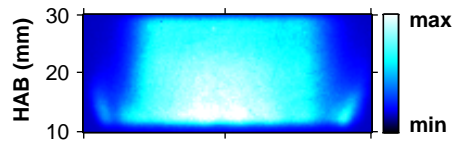
#### 4.4.5 Typical Averaged Images

The SNR of the instantaneous temperature image is rather poor. To improve the SNR of the images in Figure 4.4, Figure 4.5(a) and Figure 4.5(b) now show the same flame conditions as in Figure 4.4, but over a 200-shot average. The SNR of the averaged images is improved to  $\sim 35:1$  and  $\sim 20:1$  for the Stokes

(a) Stokes



(b) Anti-Stokes



(c) Temperature

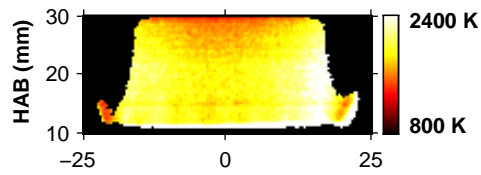


**Figure 4.5:** Typical averaged images of (a) Stokes, (b) anti-Stokes Indium fluorescence and (c) deduced temperature in Flame 1 (Table 4.1). Laser propagation from left to right. HAB, height above burner. Dimensions of images in mm.

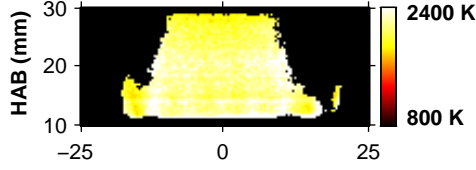


**Figure 4.6:** Typical deduced 200-shot averaged temperature image in Flame 2 (Table 4.1). Laser propagation from left to right. HAB, height above burner. Dimensions of image in mm.

and anti-Stokes respectively. Being a laminar flame, there is no other loss of information resulting from the averaging. As a result of the averaging, the SNR of the resulting temperature image is improved to  $\sim 20:1$  (*i.e.*  $\sim 100$  K).

To assess the sensitivity of the technique to operating conditions, Figure 4.6 shows the averaged temperature image for Flame 2 (Table 4.1). The calibration constant for Flame 2 is the same as determined for Figure 4.5. The TLAF measurement yields a temperature of 2030 K, in good agreement with the thermocouple measurement of 2004 K. Nonetheless, these images remain averaged over 200 shots.

#### 4.4.6 Nonlinear Excitation Regime

The linearity limited spectral irradiance has been shown to be  $2.5 \times 10^3 \text{ W/cm}^2/\text{cm}^{-1}$  in Figure 4.2. Figure 4.7 now extends the fluence to  $5 \times 10^9 \text{ W/cm}^2/\text{cm}^{-1}$ , representing the maximum attainable laser power when shaped into a line. Despite an increase in the fluence by six orders of magnitude, complete saturation (*i.e.* to a plateau) does not occur. It is apparent that there is a potential for a significant improvement in the signal intensity by increasing the spectral intensity into the nonlinear regime. An increase in the signal level reduces the susceptibility of the TLAF signal to background interference. It therefore offers the potential to improve the quality of the temperature images.

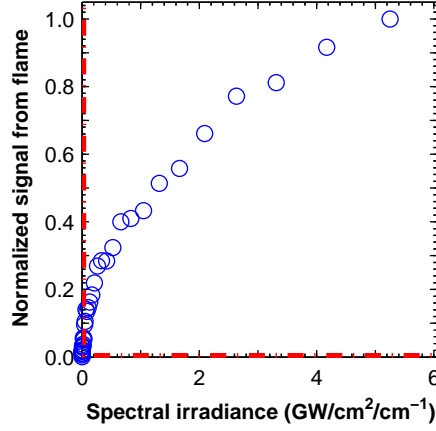


**Figure 4.7:** Indium fluorescence as a function of spectral intensity to the maximum achievable laser fluence. Stokes. Vertical and horizontal dashed line indicate limit of linearity ( $2500 \text{ W/cm}^2/\text{cm}^{-1}$ ) and the corresponding normalized signal intensity.

## 4.5 Summary

The capability of the two-line atomic fluorescence (TLAF) technique, in the linear excitation regime, to provide single-shot imaging has been assessed in this chapter. The Stokes and anti-Stokes instantaneous fluorescence images are found to have a signal-to-noise ratio (SNR) of  $\sim 18:1$  and  $\sim 5:1$ , respectively. The SNR of the deduced single-shot temperature image is found to be  $\sim 8:1$ , which corresponds to an inter-pixel noise of  $\sim 250 \text{ K}$ . Shot-averaging is found to have improved the SNR of the Stokes and anti-Stokes fluorescence images to  $\sim 35:1$  and  $\sim 20:1$  respectively. The SNR of the deduced average temperature image is improved to  $\sim 20:1$ , which corresponds to a precision of  $\sim 100 \text{ K}$ . The averaged temperature data set obtained from TLAF has been shown to be in good agreement in comparison with other techniques ( $\sim 30 \text{ K}$ ). This chapter has also shown that there is an opportunity to improve on the quality of the measurements by increasing the spectral irradiance beyond the linear excitation regime.

This page intentionally left blank.

## Chapter 5

# Assessment of Nonlinear Regime TLAF (NTLAF) in Laminar Premixed Flames

In this chapter, the feasibility to improve on the signal quality of the two-line atomic fluorescence (TLAF) measurements, by extending the incident laser energy beyond the linear excitation regime, to facilitate instantaneous imaging is assessed.

### 5.1 Introduction

In Chapter 4, it was shown that there is a significant opportunity to improve the signal quality by increasing the incident laser energy beyond the linear excitation regime. By extending the fluence into the nonlinear regime, it may be possible to achieve TLAF measurements with much improved signal-to-noise ratio (SNR) to facilitate instantaneous imaging, which is especially useful in turbulent flames. However, for work in the nonlinear excitation regime, simplifications made in previously developed derivations in the linear excitation regime no longer hold.

In this chapter, derivations are made to facilitate the application of TLAF in nonlinear excitation regime. The developed nonlinear excitation regime TLAF

(NTLAF) method is assessed by measuring the flame temperature of laminar premixed natural gas, hydrogen and ethylene flames, over a range of equivalence ratios ( $\Phi$ ).

## 5.2 Methodology

It was shown in Chapter 4 that, in the linear laser-induced fluorescence regime, the temperature takes the form of

$$T = \frac{\Delta E_{10}/k}{\ln\left(\frac{F_{21}}{I_{02}}\right) - \ln\left(\frac{F_{20}}{I_{12}}\right) + 4\ln\left(\frac{\lambda_{21}}{\lambda_{20}}\right) + C_t} . \quad (4.1)$$

To improve the fluorescence signal, there are potential advantages in extending the fluence beyond the linear limit. In this case, the previously developed derivations in the linear excitation regime will no longer apply.

Without any simplifications resulting from linearity assumptions, the derivation of the temperature follows a similar procedure but includes two additional parameters that result in the equation being independent of the fluence regime. Following the derivations given in Appendix A, the equation for NTLAF is given by

$$T = \frac{\Delta E_{10}/k}{\ln\left(F_{21} \times \left(1 + \frac{C_S}{I_{20}}\right)\right) - \ln\left(F_{20} \times \left(1 + \frac{C_A}{I_{21}}\right)\right) + C_T} , \quad (5.1)$$

where the parameters  $C_S$ ,  $C_A$  and  $C_T$  are defined as

$$C_S = \frac{Q + A}{B_{20}} , \quad (5.2)$$

$$C_A = \frac{Q + A}{B_{21}} , \quad (5.3)$$

and

$$C_T = \ln\left(\frac{\nu_{20}}{\nu_{21}}\right) + \ln\left(\frac{\Omega_{20}}{\Omega_{21}}\right) + \ln\left(\frac{\varepsilon_{20}}{\varepsilon_{21}}\right) + \ln\left(\frac{A_{20}}{A_{21}}\right) . \quad (5.4)$$

$C_S$  and  $C_A$  are obtained experimentally from the curve fits of the fluorescence from flame versus fluorescence from tank plots for the Stokes and anti-Stokes excitation schemes, over a range of laser intensity. The resulting plots are shown in Figure 5.1(a) and Figure 5.1(b), with the tank fluorescence being linearly proportional to the incoming laser intensity. The curve fits used take the form of Equation A.13. This approach permits the normalization of the variation in flame fluorescence due to laser power variation, based on the change in the tank fluorescence. It is worth noting that the laser intensity was varied here with the addition of neutral density (ND) filters of differing optical density. This is to maintain consistent optical properties of the laser while changing the laser intensity.

The  $C_T$  is subsequently determined via calibration in a premixed flame, with the use of the measurements from an alternative thermometry technique as reference, once  $C_S$  and  $C_A$  have been derived from the plots. For this work, measurements in a laminar premixed flat-flame using an R-type thermocouple with a bead diameter of 0.7 mm was used as the primary reference. The  $C_S$ ,  $C_A$  and  $C_T$  are assessed to be 4593, 29 and -1.3, respectively, for the present experiment.

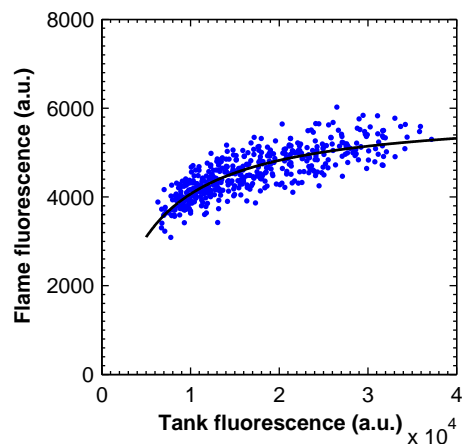
It is important to note that the  $C_S$ ,  $C_A$  and  $C_T$  values are arbitrary, and are dependent on the details of the experimental arrangement used. Given the dependence of the values on the experimental setup, it is therefore necessary to perform a similar experimental calibration procedure for different experiments.

### 5.3 Experimental Arrangement

The same experimental setup presented in Chapter 4 was used for this study. An outline of the differences follows.

Three fuels were considered in this study, namely, natural gas ( $\geq 92\%$  vol.  $\text{CH}_4$ ), hydrogen ( $\geq 99.95\%$  vol.  $\text{CH}_4$ ), and ethylene ( $> 99.5\%$  vol.  $\text{C}_2\text{H}_4$ ). The conditions for two natural gas/air flames, selected to be similar to those used in Chapter 4,

(a) Stokes



(b) Anti-Stokes

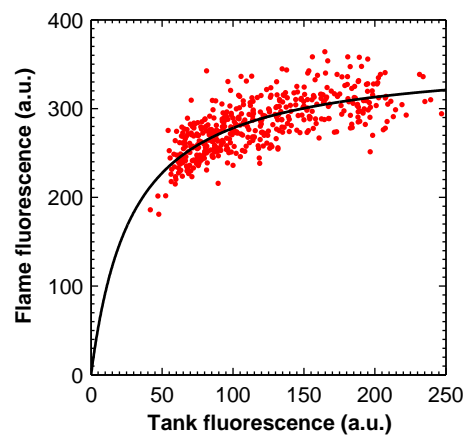


**Figure 5.1:** Flame fluorescence as a function of tank fluorescence for (a) Stokes and (b) anti-Stokes processes. Dots: NTLAF measurements. Solid line: curve fit.

Flame number	Fuel type	Equivalence ratio ( $\Phi$ )	% N <sub>2</sub> (vol/vol)	Bulk velocity (m/s)	Thermocouple reading (K)
1	Natural Gas	1.5	18	0.17	1803
2	Natural Gas	1.2	14	0.23	2004
3	Natural Gas	0.93–1.46	10.0–10.5	0.30–0.32	1810–2033
4	Hydrogen	0.94–3.78	16–28	0.11–0.20	1082–1578
5	Ethylene	0.80–2.25	9.9–17	0.19–0.32	1589–2246

**Table 5.1:** Premixed flat-flame conditions.

are presented in Table 5.1 along with the range of conditions for the other flames.

Much of the data presented are shown for a range of  $\Phi$ . In such cases,  $\Phi$  was adjusted by varying the fuel flow rate at a constant air flow rate to maintain a similar volumetric flow rate and seeded Indium concentration.

The measurements presented were conducted in the nonlinear excitation regime using a 45 mm height and  $\sim 4.5$  mm sheet with a spectral irradiance of  $2.5 \times 10^5$  W/cm<sup>2</sup>/cm<sup>-1</sup>. A thick light sheet was used in the current experiment to give improved SNR. The SNR is defined as the ratio of the signal intensity to the inter-pixel noise. All data are extracted from the central region of the flame where the Indium fluorescence is the most uniform.

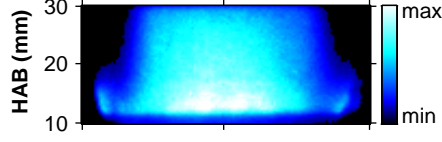
Each of the images presented in this chapter has been spatially matched and corrected for background and detector attenuation, as detailed in Section 3.4. The in-plane spatial resolution of the matched images is  $\sim 375$   $\mu$ m per pixel, in each direction.

## 5.4 Results and Discussion

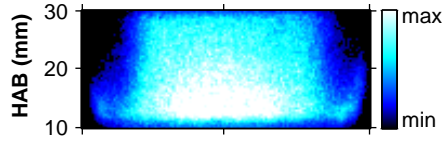
### 5.4.1 Typical Instantaneous Images

For nonlinear excitation, Figure 5.2(a) and Figure 5.2(b), respectively, show typical instantaneous Stokes and anti-Stokes fluorescence images collected simultaneously for Flame 1 (Table 5.1). The SNR of the nonlinear images is  $\sim 25:1$  for Stokes and  $\sim 15:1$  for anti-Stokes, an improvement to that achieved in the linear

(a) Stokes



(b) Anti-Stokes



(c) Temperature

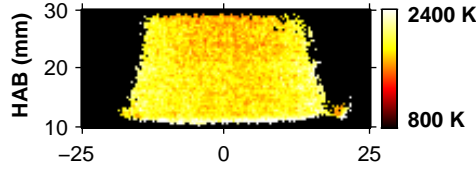
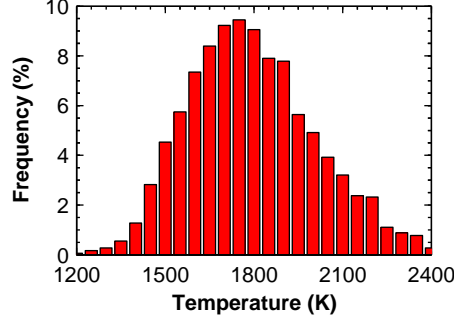


**Figure 5.2:** Typical instantaneous images of (a) Stokes and (b) anti-Stokes Indium fluorescence and (c) deduced temperature in Flame 1 (Table 5.1). Nonlinear fluence excitation ( $250,000 \text{ W/cm}^2/\text{cm}^{-1}$ ). Image size approximately  $20 \text{ mm} \times 50 \text{ mm}$ . Laser propagation from left to right. HAB, height above burner. Dimensions of images in mm.

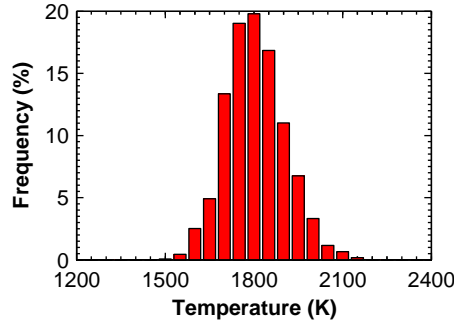
regime in Chapter 4 (*i.e.*  $\sim 18:1$  for Stokes and  $\sim 5:1$  for anti-Stokes). Applying the derived NTLAF theory to these images yields the deduced temperature image presented in Figure 5.2(c). For nonlinear excitation, the SNR of the temperature image has improved to  $\sim 20:1$  ( $\sim 100 \text{ K}$ ), significantly higher than  $8:1$  ( $\sim 250 \text{ K}$ ) of the linear regime in Chapter 4.

Figure 5.3 presents a histogram from each of the instantaneous temperature images for Flame 1, obtained using linear (Figure 4.4) and nonlinear regime TLAf (Figure 5.2), respectively. The decrease in the span of the histogram of the temperature data demonstrates an improvement in SNR, and hence an enhancement in the precision, by operation in the nonlinear regime. Specifically, while both the

(a) Linear



(b) Nonlinear



**Figure 5.3:** Temperature histograms for a typical instantaneous image of Flame 1 (Table 5.1) for (a) linear ( $2500 \text{ W/cm}^2/\text{cm}^{-1}$ ) and (b) nonlinear ( $250,000 \text{ W/cm}^2/\text{cm}^{-1}$ ) excitation regimes.

linear and the nonlinear measurements yield a mean temperature of  $\sim 1800 \text{ K}$ , the range of measured data spans  $1500\text{--}2100 \text{ K}$  for the nonlinear measurement, approximately half of the  $1200\text{--}2400 \text{ K}$  range measured in the linear regime.

#### 5.4.2 Natural Gas Flames

The generality of the NTLAF method depends on the sensitivity of the constants in equation 5.1 to local conditions, such as species concentration. To assess the sensitivity of the NTLAF technique to the composition, the  $\Phi$  of a premixed

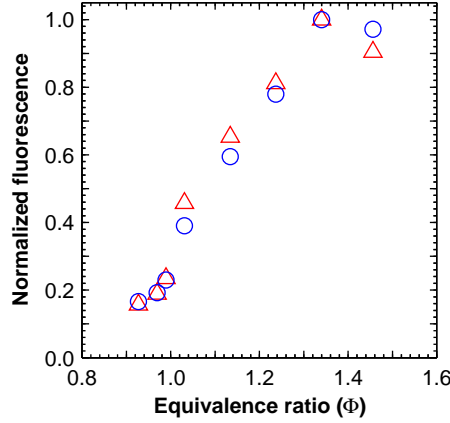


**Figure 5.4:** Normalized fluorescence signal in Flame 3 (Table 5.1) as a function of equivalence ratio. The fluorescence signals are normalized with respect to the local maximums. Open circles: Stokes. Open triangles: anti-Stokes.

natural gas/air flame was varied. This provides a range of differing concentrations of key species that may affect the NTLAF constants.

The formation of neutral Indium atoms from the Indium Chloride is favoured under fuel-rich conditions (Section 4.4). Figure 5.4 presents the Stokes and anti-Stokes fluorescence across the range of premixed natural gas/air flames achievable with the current flat-flame burner. The increase in Indium atoms in fuel-rich flames can be deduced from the increase in fluorescence signal shown in Figure 5.4.

Figure 5.5 presents the measured temperature derived over a range of  $\Phi$ . Included on Figure 5.5 are the calibrated radiation corrected temperature measurements using the thermocouple probe, as well as the deduced NTLAF temperature. The maximum temperature measured by NTLAF and the thermocouple is 2033 K. It is also noted that equilibrium calculations predict a maximum temperature of  $\sim 2060$  K, within 30 K of the NTLAF and thermocouple measurements. A close agreement between all three techniques is noted, indicating for the first time the validity of the derived NTLAF derivations.

The measurements presented in Figure 5.5 were obtained at a height 20 mm above the burner face. The NTLAF temperature was evaluated from the mean over a region of the images corresponding to the location of the thermocouple bead (measured separately). Also included in Figure 5.5 is the standard deviation

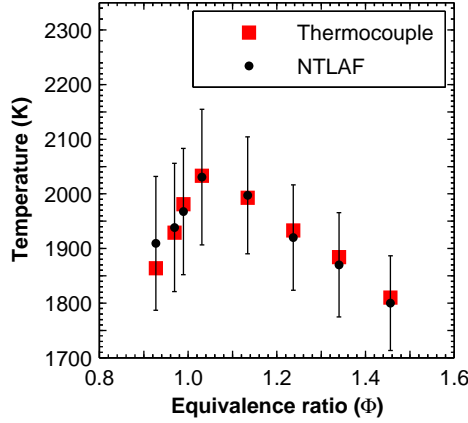


**Figure 5.5:** Temperature of Flame 3 (Table 5.1) over a range of equivalence ratios for NTLAF and calibrated thermocouple measurements.

of the data obtained from 200 shots for each NTLAF data point (indicated by the error bars). The standard deviation is typically around 100 K, representing a precision of approximately 5%, and is due primarily to detector noise in the image and imperfect correction of the laser beam energy and profile from the reference source (*viz.* the tank).

Determination of temperature by NTLAF requires calibration, which has been determined here based on the maximum temperature condition. Results at other  $\Phi$  have been calculated based on the single calibration point. The close agreement at the other equivalence ratios ( $\lesssim 20$  K) suggests that the calibration constants are relatively insensitive to changes in the flame composition.

The flame  $\Phi$  was varied by maintaining a constant flow rate of air and nitrogen through the seeder, and adjusting the fuel flow rate. This ensures a relatively constant net flow rate, and so also a consistent seeding concentration. Worth noting is that the maximum temperature is approximately 180 K below the adiabatic flame temperature for methane. This temperature drop is due to the combined effects of the nitrogen carrier gas and the effect of the water solvent used in the seeding system, which has been confirmed with systematic thermocouple measurements.

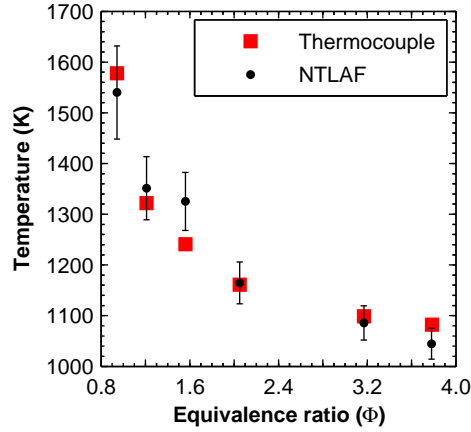


**Figure 5.6:** Temperature of Flame 4 (Table 5.1) over a range of equivalence ratios for NTLAF and calibrated thermocouple measurements.

### 5.4.3 Hydrogen Flames

Further assessment of the sensitivity of the calibration constants determined from the maximum temperature condition of the natural gas/air premixed flame is obtained by performing the measurements with hydrogen. Figure 5.6 presents the measured temperature for premixed hydrogen/air flames over a range of  $\Phi$ . The standard deviation (indicated by the error bars) obtained from the 200-shots at each NTLAF point is approximately 5%. Close agreement (typically less than 80 K) is again found between the thermocouple and NTLAF measurements. Of particular note is that, although the calibration constants were determined for natural gas fuel, they also provide good results for hydrogen. This is further confirmation of the validity and wide applicability of the nonlinear theory, even with a single set of constants.

The hydrogen/air mixture can sustain flames with higher equivalence ratio, and therefore lower temperature, than is possible for the natural gas/air case. Figure 5.6 demonstrates that the NTLAF technique can measure temperatures below 1000 K. Assessment of temperatures less than this cannot be achieved with the current burner.

As was previously observed with the natural gas/air flames, on the lean side of equivalence ratio the Indium fluorescence signal is insufficient to obtain reliable

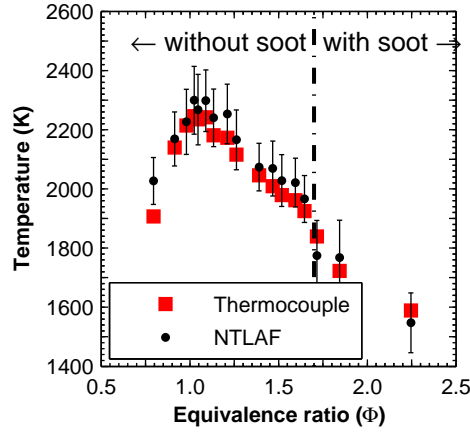


**Figure 5.7:** Temperature of Flame 5 (Table 5.1) over a range of equivalence ratios for NTLAF and calibrated thermocouple measurements.

measurement of temperature using NTLAF.

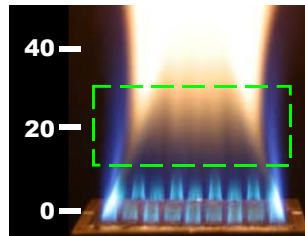
As with the natural gas flames, the temperatures in the seeded hydrogen/air flames are lower than those of an unseeded hydrogen/air flame. Again, this is primarily due to the introduction of the nitrogen from the seeding system. For the present system higher nitrogen dilution was required for the hydrogen flame to enable safe and reliable operation of the burner, although this is not a general requirement.

#### 5.4.4 Ethylene Flames

For a further examination of the sensitivity of the calibration constants to fuel type, the measurement was also performed with ethylene as the fuel. Figure 5.7 presents the measured temperatures for premixed ethylene/air flames over a range of  $\Phi$ . As before, these measurements are derived from the calibration constants obtained for natural gas and the standard deviation at each point is approximately 5%. Again, the NTLAF agrees well with the thermocouple measurements, with a difference typically not more than 40 K. The leanest ( $\Phi=0.8$ ) measurement shows the most variation between the NTLAF and the thermocouple, a difference of around 100 K, due to the lower signal under lean conditions.

Ethylene has a strong propensity to generate soot. Flame conditions with  $\Phi > 1.7$

(a) Photograph



(a) Temperature

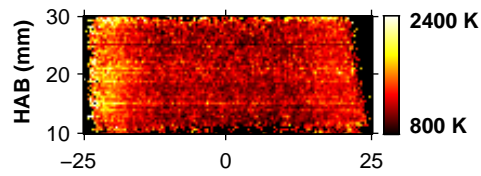


**Figure 5.8:** (a) Photograph of natural light emission from ethylene/air flame with  $\Phi=2.25$  showing soot. Dashed area indicates approximately laser-imaging area. (b) Instantaneous NTLAF temperature image for this flame with nonlinear fluence excitation ( $250,000 \text{ W/cm}^2/\text{cm}^{-1}$ ). Vertical axis indicates height above burner (mm). Laser propagation from left to right. Dimensions of images in mm.

(indicated by the vertical dashed line) visually show evidence of the presence of soot within these flames. Figure 5.8(a) shows a photograph of the flame with  $\Phi=2.25$ . The deduced NTLAF instantaneous single-shot temperature image for this flame is presented in Figure 5.8(b). The agreement between the NTLAF and the thermocouple are independent, irrespective of the presence or absence of soot (Figure 5.7). In those flames with soot, when the laser wavelength was shifted off-resonance, the fluorescence signal was found to be below detectable limits, demonstrating good capacity of the present filtering to exclude soot interferences. Similarly, soot did not influence the thermocouple readings as there was no deposition on the bead, thus not altering its emissivity.

## 5.5 Summary

In this chapter, the previous two-line atomic fluorescence (TLAF) derivations have been extended from linear excitation into the nonlinear fluence regime using existing theory. The nonlinear excitation regime TLAF (NTLAF) has been shown to provide superior signal when compared with conventional linear TLAF. The signal-to-noise ratio (SNR) of the deduced instantaneous temperature image NTLAF measurements has been shown to be  $\sim 20:1$ , which corresponds to a precision of  $\sim 100$  K. Temperature imaging with a precision of  $\sim 100$  K compares favorably with alternative thermometry techniques, but with the advantage of being suited to flames containing soot. Although NTLAF is susceptible to the effects of differing composition, the small amount of uncertainty associated with the determination of the constants is far outweighed by the ability to collect large-dimension single-shot images with superior signal. The validity of the nonlinear derivations and the applicability of a single set of constants across a wide range of flame conditions has been demonstrated. Using the calibration from a single natural gas/air premixed flame, NTLAF has been shown to resolve the temperature profile for a range of equivalence ratios for natural gas, hydrogen and ethylene flames, with deviation from thermocouple measurements not exceeding 100 K and typically  $\sim 30$  K. NTLAF imaging has also been applied to flames containing soot. For the soot levels of the flame conditions presented, the background interferences were below detectable limits, demonstrating good

capacity of filtering to exclude soot interferences. All these findings indicates the feasibility to use a single set of NTLAF constants for different flame conditions, including in the presence of soot.

## Chapter 6

# Assessment of NTLAF in Laminar Nonpremixed Flames

In this chapter, the validity of the developed nonlinear excitation regime two-line atomic fluorescence (NTLAF) method is further assessed in a laminar non-premixed flame, which has a wider range of chemical compositions and temperatures when compared with laminar premixed flame.

### 6.1 Introduction

In Chapter 5, the NTLAF method was shown to enhance single-shot precision in premixed flames from  $\sim 250\text{K}$  for conventional TLAF to  $\sim 100\text{K}$ . The calibration constants were shown to be independent of the fuel and flame composition, within experimental uncertainty, over a range of equivalence ratios for natural gas, hydrogen, and ethylene laminar premixed flat-flames. This independence from composition suggests that the technique will be applicable within the reaction zone of nonpremixed flames, however this is yet to be verified. Additionally, it is known that the local composition of the flame dramatically affects the fluorescence intensity due to changes in the mechanism of conversion of the Indium Chloride solution into Indium atoms, leading to low signal in lean conditions [59, 77]. This is a result of the requirement of the activation of the Indium within the flame front [65].

For these reasons, the viability of the NTLAF technique to cover the wider range of chemical compositions encountered in nonpremixed flames is assessed in this chapter.

## 6.2 Experimental Arrangement

The same setup used in the previous chapters was applied for this study. An outline of the differences follows.

The nonpremixed flame used in this study was produced with the same flat-flame burner used for calibration purposes. The details of the square flat-flame burner are described in Section 3.1.1.

For calibration, the burner was operated in a premixed mode, fuelled with a premixture of natural gas ( $\geq 92\%$  vol.  $\text{CH}_4$ ) and air. The air was used as a carrier gas to facilitate the seeding of Indium. The concentration of the Indium Chloride salt in the water was chosen to be 1.5 mg/mL, which has been demonstrated to provide the optimal fluorescence signal, whilst minimizing the potential effect of the metal salt on the soot formation process. The mass percentage of the seeding solution in the inlet gases is  $\sim 5\%$  for this seeding level. The result is a concentration of 75 ppm (mass basis) of Indium Chloride in the flame.

In the nonpremixed mode, the majority of the air flow was turned off, leaving only sufficient air to seed the Indium into the flame and also to clean the flame of soot. This corresponds to an air to fuel ratio of  $\sim 2.3:1$  by volume. The soot-free environment, while not necessary for the TLAf measurements, is chosen for the assessment of the present technique in nonpremixed flames, to eliminate any potential interference due to soot and to enable better modelling of the flame. The large cross-sectional area of the present burner results advantageously in a very low strain rate (flame time constant,  $D/U=0.21$  s [129]), leading to a spatially wide reaction zone. It is worth noting that although the seeding concentration used here was optimized with respect to the laminar premixed flame condition, this is not expected to have an impact on the findings of this study.

The measurements presented are for nonlinear excitation regime with a spectral irradiance of  $2.5 \times 10^5$  W/cm<sup>2</sup>/cm<sup>-1</sup>. A  $\sim 4.5$  mm thick sheet was used for this

study to allow a larger interaction region to be imaged and hence an improved signal-to-noise ratio (SNR). The SNR is defined as the ratio of the signal intensity to the inter-pixel noise. Future experiments with turbulent flames will require a thinner sheet. Each of the images presented has been spatially matched and corrected for background and detector attenuation, as detailed in Section 3.4. The in-plane spatial resolution of the matched images is  $\sim 270\text{ }\mu\text{m}$  per pixel, in each direction.

## 6.3 Results and Discussion

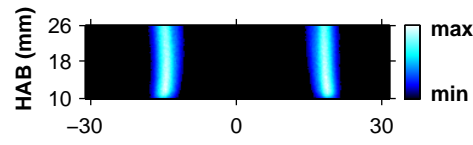
### 6.3.1 Typical Instantaneous Images

Figure 6.1(a) and Figure 6.1(b) show typical instantaneous Stokes and anti-Stokes fluorescence images, respectively, with the burner operating in nonpremixed mode. The images are  $\sim 16\text{ mm}$  high and  $70\text{ mm}$  wide, centred at  $18\text{ mm}$  height above burner (HAB).

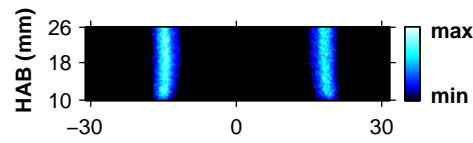
The flame front is clearly indicated by the strong Indium fluorescence in Figure 6.1(a) and Figure 6.1(b). It is readily apparent that both the Stokes and anti-Stokes transitions provide signal from approximately the same parts of the flame. This is due to the presence of sufficient concentration of neutral Indium atoms in these regions. It is also evident that the Stokes signal has a higher SNR than the anti-Stokes signal. The SNR of the images is  $\sim 20:1$  for Stokes and  $\sim 9:1$  for anti-Stokes. Note that the images presented have not been enhanced by image smoothing to reduce inter-pixel noise, as this may give misleading results regarding the SNR of the technique and also degrade the spatial resolution.

Figure 6.1(a) and Figure 6.1(b) also indicate that no Indium fluorescence is detected on either side of the reaction zone, implying a paucity of neutral Indium atoms there. While Indium Chloride is present in high concentrations along the jet centreline, the temperature and chemical conditions in this region are evidently not amenable to the formation of free, neutral atomic Indium, as is required for TLAF. The mist generated by the nebulizer creates fine droplets of Indium Chloride dissolved in water. Upon heating near the flame front, desolva-

(a) Stokes



(b) Anti-Stokes



(c) Temperature

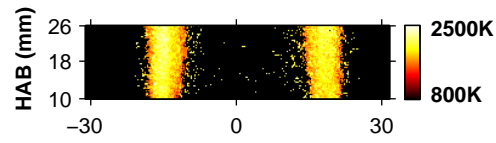


**Figure 6.1:** Typical instantaneous images of (a) Stokes and (b) anti-Stokes fluorescence and (c) deduced temperature in a laminar nonpremixed flame. Nonlinear fluence excitation ( $250,000 \text{ W/cm}^2/\text{cm}^{-1}$ ). Laser propagation from left to right. HAB, height above burner. Dimensions of images in mm.

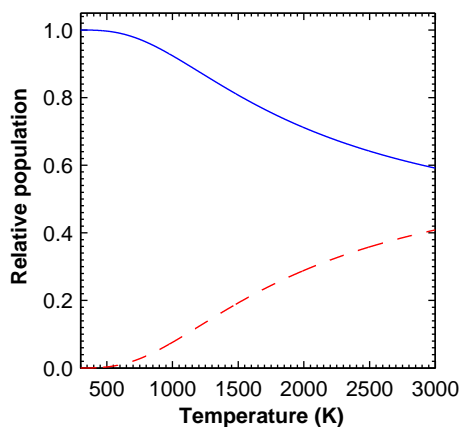


**Figure 6.2:** Boltzmann fraction as a function of temperature. Solid line: Stokes. Dashed line: anti-Stokes.

tion occurs, whereby the solvent is evaporated, leaving the Indium in the form of various metal complexes [89, 92]. The desolvated ions and molecules subsequently undergo a series of gas-phase reactions before neutral Indium atoms are released.

The process by which the Indium is converted into free atoms is dependent on numerous factors, one of which is the temperature. Away from the reaction zone the temperature is too low to generate sufficient Indium atoms. The Boltzmann distribution for both Stokes and anti-Stokes processes is constructed using the constants given by Sansonetti and Martin [125], and is presented in Figure 6.2. From the figure, it can be seen that the relative population of the anti-Stokes is less than  $\sim 3\%$  below  $\sim 800$  K. The absence of fluorescence signal in the central region of the flame is a limitation. Nonetheless, data is obtained from the regions of greatest interest, notably in and around the reaction zone, where the temperature exceeds 1000 K.

It should also be noted that, for the present experiment, the surrounding air was not seeded with Indium. While it has been shown that temperature may be deduced from TLAf under slightly lean conditions ( $\Phi \sim 0.8$ ) [82] the concentration of Indium atoms, and thus the intensity of its fluorescence, is known to be low under lean conditions. Previous investigations have suggested this decrease is

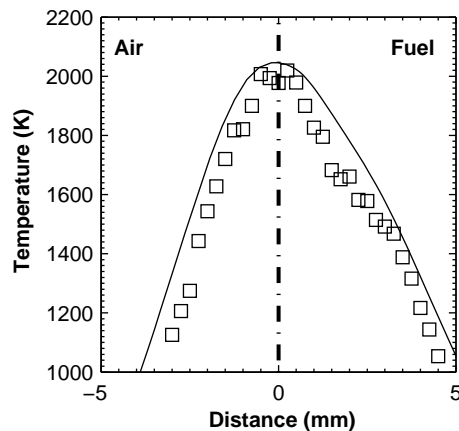


**Figure 6.3:** Temperature profile across the reaction zone of a laminar nonpremixed flame, from NTLAF measurements and laminar flame calculations. Open squares: NTLAF measurements. Solid line: laminar flame calculations.

due to an abundance of oxidizing species under such conditions [59, 77]. Hence, seeding the surrounding air does not improve the level of signal there and would lead to additional cooling effects due to the presence of extra water solvent.

Applying the NTLAF theory to the fluorescence images yields the image of deduced temperature presented in Figure 6.1(c), which has a SNR of  $\sim 16:1$ . Due to this inter-pixel noise, the corresponding precision for the temperature is  $\sim 120$  K, and is of this order over the entire temperature range. Those parts of the image for which no data is obtained are indicated to have a temperature of below 800 K. However, as described above, it is not possible to discriminate this temperature regime from other conditions not favorable for producing neutral Indium atoms from the Indium Chloride. Nonetheless, from Figure 6.1(c), it is apparent that the temperature is obtained over a reasonable range across the reaction zone.

### 6.3.2 Laminar Flame Calculations

Figure 6.3 presents the average temperature profile across the reaction zone over the range for which data can be obtained. This figure was produced by shifting each row of the temperature image (Figure 6.1(c)) to align the maximum temper-

atures. The radial profile is subsequently generated from the median average of rows (20 rows) from the centre of the image. This realignment of the temperature data is needed to account for the slight fluctuation in the flame front location across the height of the image. The realignment is also important to preserve the spatial features of the temperature data, particularly at the lateral wings, which are sensitive to the steep spatial gradients that occur in nonpremixed flames.

Overlaid on Figure 6.3 is the temperature profile from laminar flame calculations of the current experimental conditions using the OPPDIF routine of Chemkin, with the GRI-Mech 3.0 mechanism, at a peak normal strain rate of  $\sim 30 \text{ s}^{-1}$ . Due to the different configuration (co-flowing versus counter-flowing), the temperature profiles are not expected to match perfectly, but in general, good agreement is observed. The laminar flame calculations predict a peak temperature  $\sim 50 \text{ K}$  higher than the measurements. A difference of this magnitude is expected since the cooling effects of the liquid-phase water solvent (calculated to be  $\sim 30 \text{ K}$ ) and radiation are not taken into consideration in the calculations, which in combination more than account for the  $50 \text{ K}$  discrepancy.

It is also apparent from Figure 6.3 that the lowest temperature recorded is  $\sim 1000 \text{ K}$ . This threshold is significantly higher than the  $800 \text{ K}$  required for the anti-Stokes transition to yield a sufficient accessible ground-state population. This suggests that the Indium formation process from the Indium Chloride solution does not become significant until  $\sim 1000 \text{ K}$ . This temperature limit is consistent with previous TLAF studies [29].

## 6.4 Summary

In this chapter, the viability of the nonlinear excitation regime two-line atomic fluorescence (NTLAF) in a laminar nonpremixed flame, which has a wider range of chemical compositions and temperatures, has been assessed. The Indium has been seeded into the flame as Indium Chloride dissolved in distilled water. The NTLAF technique is used to resolve the temperature profile across the reaction zone of a laminar nonpremixed flame and the measured profile shows good agreement with the laminar flame calculations. The precision of the NTLAF

measurements is observed to be  $\sim 120$  K across the reaction zone, for the existing arrangement, where the temperature exceeds 1000 K. Indium fluorescence is observed to be the strongest at the flame front due to the local abundance of neutral Indium atoms. This observation reveals important information on the formation of free Indium atoms within the flame environment. Identification of the range where the NTLAF technique is applicable in nonpremixed flames using a water solvent to seed the Indium highlights the potential for further studies on alternative seeding arrangements.

# Chapter 7

## Solvent Effects on NTLAF Measurements

Indium has been typically seeded into flame as Indium Chloride dissolved in distilled water, when gaseous fuel is used. In this chapter, the feasibility to improve on the signal quality of the nonlinear excitation regime two-line atomic fluorescence (NTLAF) technique through the substitution of organic solvent for distilled water as the seeding solution is examined.

### 7.1 Introduction

The use of organic solvents to enhance spectral line emission in flame photometry was first reported by Berry *et al.* [130] and has since been widely applied to various flame spectroscopic techniques involving the utilization of flames to convert dissolved samples into optically active entities. A number of previous studies have investigated the effects of the various physical and chemical parameters involved in the enhancement of the spectral line emission with the use of organic solvents in place of water as the seeding medium (*e.g.* [87, 91, 131, 132]). The physical effects influence the release rate of the solute into flame by factors such as the rate of evaporation of the droplets and the droplet size distribution. The chemical effects, on the other hand, influence the flame temperature and chemical kinetics directly through the combustion of the solvent in flame. The aim of these

previous investigations has been to optimize the spectroscopic techniques by the combined physical and chemical effects of the organic solvents. These previous studies have focused on the improvement of the detection of the samples delivered to the flames, which are often only available in small quantities.

With some notable exceptions (*e.g.*, [29]), Indium has been typically seeded into flame in previous studies as Indium Chloride dissolved in water. This work therefore aims to investigate on the feasibility to improve the signal quality of the NTLAF Indium fluorescence images through the substitution of organic solvent for distilled water as the seeding medium. This work aims to exploit the physical effects of the organic solvent, with a secondary benefit of providing a small positive chemical influence of the solvent introduced on the properties (in particular the temperature) of the flame. These influences are explored for acetone, isopropanol, methanol, and ethanol, following earlier work to enhance emission in flame photometry [131]. In addition to the effect of the pure organic solvents, this work also aims to investigate the influence of mixtures of the organic solvent with water on the fluorescence signal. It then aims to assess the influence of flame equivalence ratio ( $\Phi$ ) on fluorescence signal and on signal-to-noise ratio (SNR) for those organic solvents that are found to have performed most favourably. The fluorescence signal obtained with water as the solvent is used as the reference measurement.

## 7.2 Methodology

### 7.2.1 Indium Atoms in Measurement Volume

Despite the complexity of the processes involved in the generation of neutral Indium atoms, as detailed in Section 2.3, the number of the thermally excited atoms within the measurement volume can be described by the Maxwell-Boltzmann distribution law [91, 132],

$$N^* \propto N \exp\left(-\frac{E}{kT}\right) . \quad (7.1)$$

Here, the concentration of the neutral atoms in the excited state,  $N^*$ , is governed by the concentration of the neutral atoms in the ground state,  $N$ , and the temperature of the flame,  $T$ . The ground state concentration of the neutral atoms within the measurement volume is influenced by the effective supply of the solute to flame. The increase in the effective supply of the solute is brought about by factors such as improved nebulizer performance and increased solvent evaporation rate from the droplets. The change in temperature of the flame is directly influenced by the combustion of the seeding solution that is introduced with the solute [87, 131].

### 7.2.2 Ultrasonic Nebulization

For this investigation, an ultrasonic nebulizer is used to disintegrate the seeding solution into an aerosol of droplets. The electronically driven nebulizer utilizes ultrasonic vibrations, whose energy is derived from the piezoelectric transducer [118], to generate unstable surface waves at the liquid-air interface. The liquid sheet is fragmented and subsequently released into the surrounding air as very fine droplets [117, 118, 133, 134]. This disintegration technique is characterized by fine droplets with a quite uniform size distribution. An empirical equation to estimate the droplet size from the ultrasonic nebulizer is described by Lang [117],

$$D = 0.34 \left( \frac{8\pi\sigma}{\rho F^2} \right)^{1/3}. \quad (7.2)$$

Here,  $D$  is the median diameter of the droplets,  $F$  is the exciting frequency of the ultrasonic nebulizer,  $\sigma$  is the surface tension, and  $\rho$  is the density of the liquid. Lang's correlation indicates no dependence of the droplet size on the liquid phase viscosity, which may be contrary to a number of experimental observations [118, 135]. However, the Lang's correlation provides a reasonably accurate estimation when the effect of the liquid viscosity on the droplet size is negligible [133].

Fuel	Equivalence ratio ( $\Phi$ )	Bulk velocity (m/s)	Thermocouple reading (K)
Natural Gas	0.91-1.80	0.27-0.29	1665-2165

**Table 7.1:** Premixed flat-flame conditions.

Solvent	Vapour pressure (kPa)	Density (kg m <sup>-3</sup> )	Viscosity (cP)	Surface tension (mN m <sup>-1</sup> )	Polarity index	Diameter ( $\mu$ m)
Acetone	24	790	0.32	25	5.1	2.21
Ethanol	5.9	789	1.18	22	4.3	2.12
Isopropanol	4.4	786	2.27	21	3.9	2.09
Methanol	12.3	792	0.58	23	5.1	2.15
Water	2.3	1000	1.00	73	10.2	2.92

**Table 7.2:** Selected physical properties of the solvents at 20 °C and 1 atm, and the median diameters of the resultant droplets estimated using Lang’s correlation.

## 7.3 Experimental Arrangement

The same setup used in the previous chapters was applied for this study. An outline of the differences follows.

For the assessment of the effects of solvents, a uniform, stable environment that enables comparisons to be made between different experimental cases was produced using the square flat-flame burner described in Section 3.1.1. The conditions of the natural gas ( $\geq 92\%$  vol. CH<sub>4</sub>)/air flames used are presented in Table 7.1. The air was used as a carrier gas to facilitate the seeding of Indium.

Much of the data presented in the first part of the study were collected with the flame  $\Phi$  set at unity. For the second part of the investigation, the  $\Phi$  of the flame was varied by varying the fuel flow rate at a constant air flow rate to maintain a similar total volumetric flow, and hence similar seeded Indium concentration.

Four organic solvents were considered, namely acetone, ethanol, isopropanol and methanol in addition to water. Selected physical properties of the solvents at 20 °C and 1 atm used in this investigation are presented in Table 7.2. A concentration of 1.5 mg/mL was used for all seeding solution (Section 4.4).

The temperature of the flames was measured with a fine-wire R-type thermocouple with a bead diameter of 0.7 mm. The thermocouple readings were corrected for radiation losses by applying an energy balance (Appendix B) to the thermocouple bead [21, 136].

The measurements were conducted in the nonlinear excitation regime with a spectral irradiance of  $2.5 \times 10^5 \text{ W/cm}^2/\text{cm}^{-1}$ . A  $\sim 4.5$  mm thick sheet was used for this study to allow a larger interaction region to be imaged and hence an improved SNR. Each of the images presented has been spatially matched and corrected for background and detector attenuation, as detailed in Section 3.4.

## 7.4 Results and Discussion

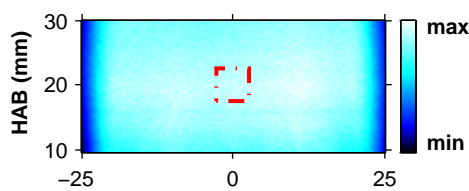
### 7.4.1 Effects of Solvents on Indium Fluorescence Emission

Figures 7.1(a) and 7.1(b) show typical instantaneous Indium Stokes and anti-Stokes fluorescence images, respectively, from the laminar premixed natural gas flat-flame. The images are  $\sim 20$  mm high and 50 mm wide, centred at a 20 mm height above burner (HAB). All data are extracted from the central region, as indicated by the dashed area in Figure 7.1, where the Indium fluorescence is most uniform.

#### 7.4.1.1 Organic Solvents

To assess the physical effects of the solvents on the spectral line emission, Figure 7.2 presents the data obtained from a 150-shot average of both the Stokes and anti-Stokes fluorescence for the solvents selected. As a reference, the fluorescence signals are normalized with respect to the fluorescence signal recorded when water is used. The concentration of the Indium salt was maintained at 1.5 mg/mL for all the seeding solutions used. This ensures that any change in the Indium fluorescence observed is solely a function of the solvent used, rather than an effect of differing Indium salt concentration within the solvents. Therefore, any variation in the fluorescence emission would give an indication on the efficiency of the generation of neutral Indium atoms associated with the use of

(a) Stokes



(b) Anti-Stokes

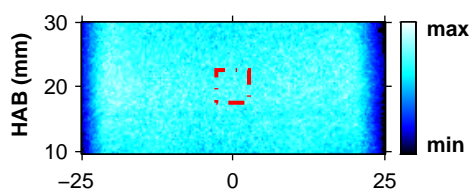


**Figure 7.1:** Typical instantaneous images of (a) Stokes and (b) anti-Stokes fluorescence in a laminar premixed natural gas flat-flame. Dashed area indicates data extraction area. Laser propagates from left to right. HAB, height above burner. Dimensions of images in mm.

different solvents, rather than the amount of Indium Chloride salt seeded.

Additionally, the  $\Phi$  was maintained at unity during the course of the experiment. This makes certain that any change in the fluorescence signal can be attributed entirely to the physical effects, *i.e.* negligible chemical influence on the properties of the flame. Thermocouple measurements show that the flame temperature varies by less than 40 K with the different solvents, suggesting that any influence of this parameter on the fluorescence emission is small.

From Figure 7.2, it is apparent that there is a threefold to fivefold gain in fluorescence signal, when organic solvents (excluding isopropanol) are used instead of water. Acetone and methanol, in particular, are observed to have intensified the fluorescence emission the most. The increase in the emission when organic solvents are used can be explained by the dependence of the nebulizer performance on the viscosity and the surface tension of the solutions [137]. Organic solvents such as acetone, ethanol and methanol have lower viscosity and surface tension values than water (Table 7.2). This eases the disintegration process, allowing

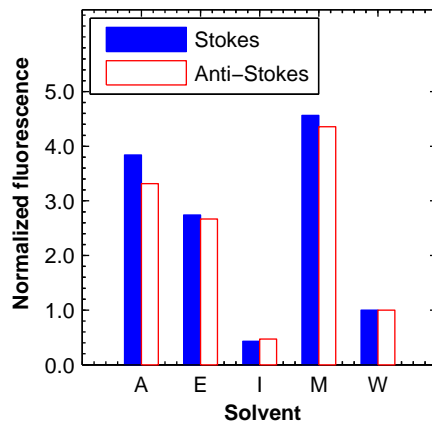


**Figure 7.2:** Normalized Indium Stokes and anti-Stokes fluorescence for five different seeding solutions for a flame equivalence ratio of 1.0. The fluorescence signals are normalized with respect to the fluorescence signal recorded with water as seeding solution. A: Acetone E: Ethanol I: Isopropanol M: Methanol and W: Water.

droplets with smaller sizes (Table 7.2) to be generated at a more rapid rate.

The droplets sizes are estimated using Lang’s correlation (Equation 7.2). Sindayiehbura *et al.* [133] have shown that the effect of liquid viscosity on the diameters of the droplets is negligible for the methanol-water and glycerol-water mixtures used in their investigation. This, combined with the knowledge that the estimated values are well within the range of droplet sizes (1–5  $\mu\text{m}$ ) typically generated from ultrasonic nebulization [118], justifies the use of the Lang’s correlation for the present investigation. Additionally, these organic solvents have a higher vapour pressure than water (Table 7.2), making the resultant droplets more evaporative and hence leading to a reduction in the amount of droplets persisting into the flame [91]. Together, these factors enhance the disintegration and desolvation process and hence the effective supply of the solute, namely Indium Chloride, into the flame. The increase in the effective supply of the solute leads to an increase in the concentration of Indium species in flame. This explains the stronger fluorescence emission observed.

It is also interesting to note that, even though isopropanol has more favourable physical properties (lower surface tension and higher vapour pressure) than water (Table 7.2), Figure 7.2 shows a drop in the fluorescence emission when isopropanol is used in place of water. The drop in the emission can be explained by the low

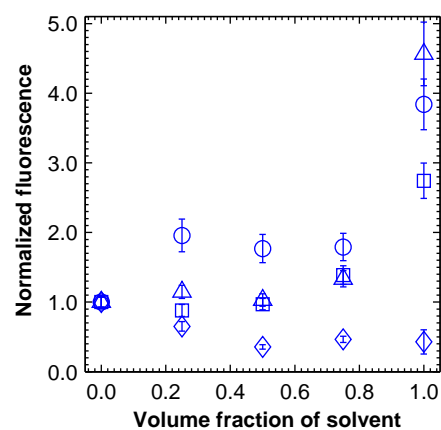
solubility of the polar Indium salt in the non-polar isopropanol, as indicated by the low polarity index of the solvent [138] in Table 7.2. The low solubility of the salt in the isopropanol solvent resulted in a reduction in the transportation of the solute into the flame, and hence the fluorescence emission. This finding indicates that there are limits to the types of organic solvent that can be used to enhance the fluorescence emission from the flame due to the polar nature of the Indium Chloride salt.

#### 7.4.1.2 Organic Solvent-Water Mixtures

The TLA<sub>F</sub> process is affected by a combination of processes (Section 2.3) that produce the TLA<sub>F</sub> active species. Most of these processes utilize little heat as compared with the heat released in a combustion reaction [29, 87]. An exception to these processes is desolvation, which takes up a significant fraction of the heat content, leading to a  $\sim 100\text{--}150$  K cooling of the flame [77]. This reduction in the flame temperature is significant and will change the combustion processes, so should be avoided if possible.

In Figure 7.3, the Indium Stokes and anti-Stokes fluorescence are plotted as a function of the volume fraction for the organic solvents within the seeding solution. This is to investigate the feasibility of using an organic solvent-water mixture whose enthalpy of reaction matches the latent heat of vaporization and also provides a reasonable gain in fluorescence signal. To assess this, the volume fraction of the organic solvent and water within the seeding solution were varied. Again, the concentration of the Indium salt within the seeding solution was maintained at 1.5 mg/mL. It is clear that, for the present burner system arrangement, the fluorescence signals for acetone, ethanol and methanol (normalized by the fluorescence signal recorded with water) increase with the concentration of the organic solvents within the seeding solution. However, the dependence is not linear. Rather, a sudden increase in the emission occurs when the volume fraction of the organic solvents within the seeding solution exceeds  $\sim 0.8$ . This observation implies that even though enhancement is attainable with the use of organic solvent-water mixtures; almost pure organic solvents are needed to achieve significant intensification. A volume fraction of  $\sim 0.1$  (significantly less than the amount required for sufficient intensification) corresponds to the concentration

(a) Stokes



(b) Anti-Stokes

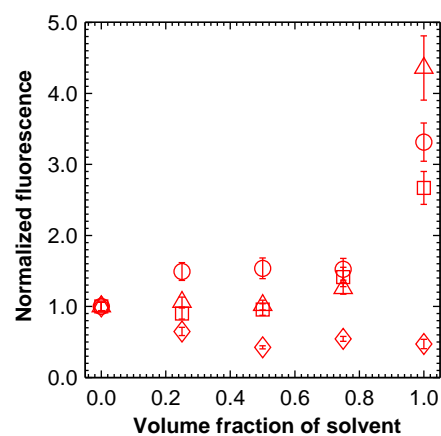


**Figure 7.3:** Normalized Indium (a) Stokes and (b) anti-Stokes fluorescence over a range of concentration of organic solvents within seeding solution, balanced with distilled water. The fluorescence signals are normalized by the fluorescence recorded with water as seeding solution. Open circles: acetone. Open squares: ethanol. Open diamonds: isopropanol. Open triangles: methanol.

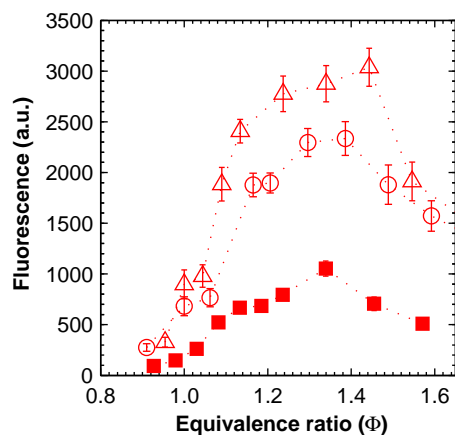


**Figure 7.4:** Indium fluorescence as a function of flame equivalence ratio. Anti-Stokes. Open circles: acetone. Open triangles: methanol. Squares: water.

of each of the organic solvent-water mixtures needed to match the enthalpy of reaction with the latent heat of vaporization of the mixture within flame. Hence, no benefit in using organic solvent-water mixture was found. Rather, these findings suggest that pure organic solvents should be used. The use of isopropanol as the solvent was found to reduce the fluorescence, consistent with the finding reported earlier.

Stokes fluorescence has been shown to have a higher SNR than anti-Stokes. Since the temperature is determined from the ratio of the two signals, the latter controls the SNR. Additionally, both Stokes and anti-Stokes are observed to display similar characteristics throughout this investigation. Hence, only the anti-Stokes fluorescence results are presented and discussed in the subsequent sections.

## 7.4.2 Effects of Selected Organic Solvents on Indium Fluorescence for Different Equivalence Ratios

### 7.4.2.1 Fluorescence

Comparison between the effectiveness of acetone and methanol, which are shown above to have performed most favourably, is made across a range of equivalence ratios of the laminar premixed flame. Figure 7.4 presents the measured anti-

Stokes fluorescence emission from these flames, with acetone, methanol or water (reference case) used as the seeding solution. Error bars (one standard deviation with respect to the mean) are used in the figure to show the variability in the measurements.

It is readily apparent from Figure 7.4 that the fluorescence increases as the  $\Phi$  of the flame increases, over the range  $0.9 < \Phi < 1.4$ . This indicates that the neutral Indium atoms are produced more effectively when the flame is rich, consistent with the findings of previous studies (*e.g.*, [29, 77, 139]). The process by which the Indium is converted into free atoms is dependent on multiple factors, involving the temperature and the local chemical composition. The lower fluorescence signal emission in the lean combustion region is caused by the less suitable chemical condition due to the abundance of oxidizing species. Beyond  $\Phi = 1$ , the fluorescence signal is observed to continue increasing, despite a reduction in flame temperature. This highlights the importance of the local chemical composition on the Indium fluorescence signal. The chemical conditions beyond  $\Phi = 1.4$  are apparently insufficient to counteract the drop in signal due to further reduction in temperature.

Figure 7.4 demonstrates a substantial increase in the fluorescence intensity when the organic solvents are employed. The enhancement is threefold to fivefold when acetone or methanol is used, and is higher with methanol. This suggests that the release rate of the solute improves the most with methanol.

The higher gain in the fluorescence emission appears to be explained by the finer methanol droplets relative to acetone and water (Table 7.2). The surface area per unit volume is inversely proportional to the droplet size. Methanol, which has the smallest droplet size, has the largest surface area per unit volume. The methanol droplets are desolvated at a faster rate than acetone and water droplets, resulting in a highest rate of release of solute and hence fluorescence emission as observed. It is interesting to note that the measured nebulization rate of acetone is  $\sim 1.5$  times (volumetric) higher than that of methanol. Furthermore, acetone vaporizes easier than methanol, as indicated by the higher vapour pressure in Table 7.2. Together, these findings show that despite the higher nebulization rate and volatility of the droplets when acetone is used, the effective supply of solute to flame is enhanced the most when methanol is used as seeding solution.

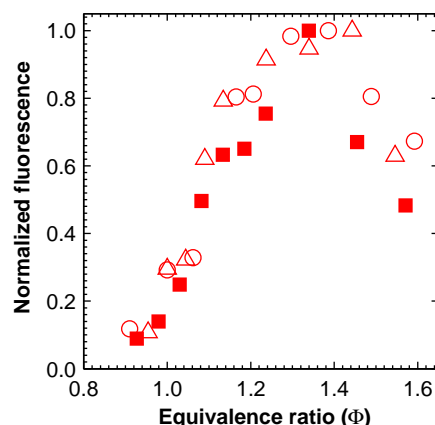


**Figure 7.5:** Normalized fluorescence signal as a function of flame equivalence ratio. The fluorescence signals are normalized with respect to local maximums. Anti-Stokes. Open circles: acetone. Open triangles: methanol. Squares: water.

#### 7.4.2.2 Normalized Fluorescence

The anti-Stokes fluorescence signals, normalized by the local maximum fluorescence values, are shown in Figure 7.5. The normalized curves are observed to display similar characteristics over the range of flame equivalence ratios presented. The good overlapping of the profiles, despite the differences in the properties of the solvents, suggests that any chemical influence of the organic solvents is small. Rather, the influence on fluorescence signal is dominated by the capacity to supply solute to the flame. The overlap of the profiles also indicates that the profiles are proportional with a factor that is constant over the tested range of flame equivalence ratios. This finding further validates the comparisons of the various solvents and solvent-water mixtures at a single flame condition in the previous sections (Section 7.4.1.1 and Section 7.4.1.2), since the differences between the solvents are observed to be consistent for all flame equivalence ratios.

#### 7.4.2.3 Relative Gain in SNR

To further assess the effectiveness of the organic solvents in enhancing the fluorescence signal, the relative gain in the SNR as a function of the flame equivalence ratio is presented in Figure 7.6. Error bars (one standard deviation) are used in the figure to show the variability in the measurements. SNR is defined here as

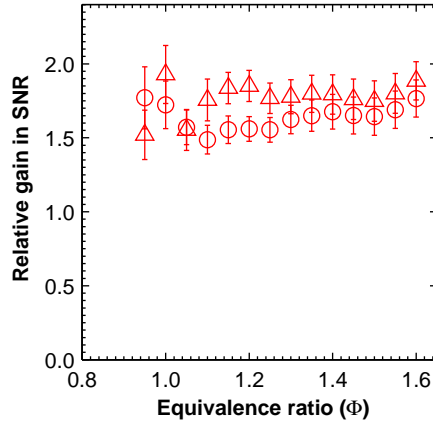


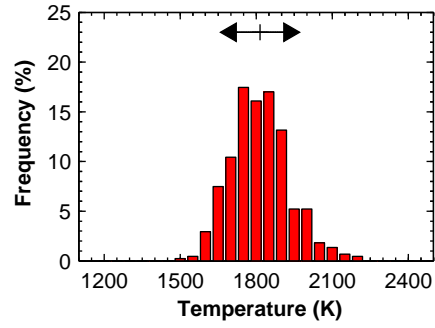
**Figure 7.6:** Relative gain in SNR of the Indium fluorescence as a function of flame equivalence ratio. Anti-Stokes. Open circles: acetone. Open triangles: methanol.

the ratio of the average signal intensity to the inter-pixel noise. This figure was obtained by comparing the SNR of the anti-Stokes fluorescence images obtained with acetone and methanol with water over a range of flame equivalence ratios. Figure 7.6 shows that methanol and acetone enhance the SNR of the fluorescence image across the tested range of the flame equivalence ratios. The gain in SNR is observed to be relatively invariant at  $\sim 1.8$  above a flame equivalence ratio of  $\sim 1.1$ . The observed invariant profile appears to be explained by the more efficient neutral Indium atom formation process in the fuel-rich region, counteracting the drop in fluorescence signals due to the decrease in flame temperature (in accordance with Equation 7.1) in the richer region. Some scatter in the data, coupled with larger error bars, is observable in the lean region of the flame. This is to be expected due to the lack of active Indium species in such an environment.

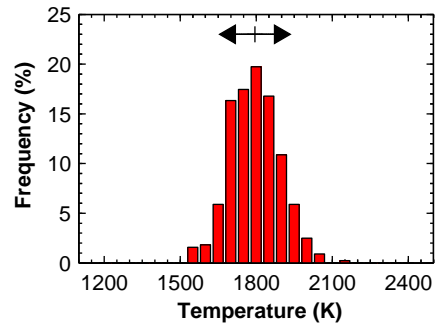
### 7.4.3 Effects of Solvents on the SNR of Temperature Images

Figure 7.7 presents histograms obtained from the typical instantaneous flame temperature images collected at  $\Phi \approx 1.55$ , with acetone, methanol, and water as seeding solutions. Again, the data are extracted from the central region, as indicated by the dashed area in Figure 7.1, of the temperature images. The histograms demonstrate that the use of the organic solvents provides a signifi-

(a) Acetone



(b) Methanol



(c) Water

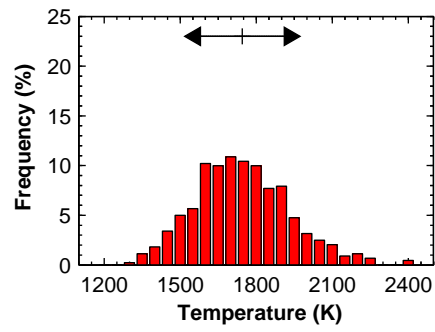


**Figure 7.7:** Temperature histograms from typical instantaneous images of laminar premixed flame with a flame equivalence ratio of  $\sim 1.55$  with (a) acetone (b) methanol and (c) water as seeding solution. Double-headed arrows indicate the temperature spans that are associated with one standard deviation.

cant improvement in SNR, as indicated by reduced temperature span, and the increased frequency at the expected temperature ( $\sim 1800$  K) of the flame. Double-headed arrows are also used to indicate the temperature spans that are associated with one standard deviation from the mean. Hence, a gain in the single-shot precision of the temperature images results. Again, the SNR of the temperature images are found to improve by a factor of  $\sim 1.8$  and  $\sim 1.6$ , with methanol and acetone as seeding solutions respectively, compared with water.

## 7.5 Summary

In this chapter, the potential use of four different solvents, namely acetone, ethanol, isopropanol and methanol, to replace water as the seeding solvent for nonlinear excitation regime two-line atomic fluorescence (NTLAF) has been investigated. Acetone and methanol have been shown to yield the highest gain in the fluorescence signal intensity (approximately threefold to fivefold). No significant benefit in signal gain is observed with the use of organic solvent-water mixtures. Acetone and methanol have been shown to enhance the SNR of the fluorescence emission over the range of flame equivalence ratios that were investigated, with the most significant enhancement (approximately twofold) observed in the rich combustion region. The use of acetone and methanol, therefore, has the potential to improve the precision of the deduced instantaneous temperature image using nonlinear two-line atomic fluorescence (NTLAF) measurements to  $\sim 60$  K. Acetone and methanol have also been demonstrated not to have a detrimental effect on the neutral Indium formation process. The benefit of the organic solvents is attributed mainly to combined influence of the more favourable physical properties that control the rate at which Indium species is seeded into the flame, such as surface tension, solubility and vapour pressure. The identification of the feasibility to enhance the signal quality of the NTLAF measurements, with the use of alternative solvent to replace water as the seeding solution, represents a significant development to support future imaging applications in turbulent and/or sooting flames where the backgrounds are expected to be more pronounced.

This page intentionally left blank.

# Chapter 8

## Application of NTLAF in Sooty Flames

In this chapter, the applicability of nonlinear excitation regime two-line atomic fluorescence (NTLAF) in sooty flames is examined. In particular, the interference of soot and its precursors on the NTLAF measurements is assessed.

### 8.1 Introduction

In Chapter 5, the NTLAF technique has been shown to provide accurate temperature measurement in lightly sooty flames. However, the applicability of NTLAF to perform temperature measurements in flames with higher soot concentrations is yet to be assessed. Such assessments are required because the extent of interference from spurious scattering, laser-induced incandescence and/or fluorescence from soot precursors [140] can be expected to increase when higher soot concentration is present within the flame.

This chapter aims to compare the measurements, for both the Stokes and anti-Stokes processes, when the excitation laser beams are tuned on- and off-wavelength. The measurements, when induced on-wavelength, are comprised of the Indium fluorescence signal and any induced interferences; whereas the measurements, when induced off-wavelength, are due from the extraneous interfer-

ences from non-Indium sources. The comparison of these measurements therefore gives an estimation of the contribution of the interferences from the non-Indium sources towards the NTLAF measurements. The measurements are compared over a range of operating laser fluences and flame equivalence ratios ( $\Phi$ ).

## 8.2 Experimental Arrangement

### 8.2.1 Burner and Seeding Arrangement

Laminar nonpremixed flames were chosen for this study since soot is formed readily in such conditions, whilst avoiding complications associated with the presence of turbulence [141]. Additionally, nonpremixed flames typically have distinct regions that are useful for the identification of the source of any observed extraneous interferences, based on spatial position in the reaction zone.

A Jet in Hot Co-flow (JHC) style burner was used in this study to generate the laminar nonpremixed flames required. The burner consists of a central fuel jet within an annular co-flow. An air co-flow was used for the present study. The details of the burner are given in Section 3.1.2. Industrial grade ethylene (>99.5% vol.  $\text{C}_2\text{H}_4$ ) was chosen as the fuel for this study. A portion of the fuel was passed through a seeder to facilitate the seeding of Indium into the fuel stream. The seeder, which consists of an ultrasonic nebulizer within a container, was used to generate a mist of droplets of Indium chloride dissolved in methanol. The concentration of the Indium chloride salt in the solution was chosen to be 1.125 mg/mL. This concentration provides an optimal signal while avoiding absorption and signal trapping for the investigated flame conditions.

The parameters of the fuel stream at the exit of the central fuel jet, issuing into a fixed air co-flow, are shown in Table 8.1. The  $\Phi$  of the flame was varied by adjusting the air flow rate with a constant fuel flow rate, thus maintaining a similar amount of seeded Indium within each of the flames. The low flow rates employed resulted in flames at low strain rates. These flames have spatially wide reaction zones with discernible features, which is advantageous for the purposes of this study.

Flame Number	Fuel stream	Equivalence ratio ( $\Phi$ )	Bulk velocity (m/s)	Percentage O <sub>2</sub> (% vol.)
1	Ethylene	$\infty$	0.63	0.0
2	Ethylene & air	31.3	0.91	6.3
3	Ethylene & air	9.6	1.53	12.3
4	Ethylene & air	5.9	2.09	14.6
5	Ethylene & air	4.2	2.68	16.0

**Table 8.1:** Parameters of the fuel stream at the exit of the central fuel jet, issuing into a fixed air co-flow, for the flame conditions of interest.

### 8.2.2 Optical Layout

The experimental arrangement in this chapter follows the setup depicted in Figure 3.9. In brief, the beams from the two Nd:YAG-pumped dye lasers were fired with  $\sim 100$  ns separation, and were shaped into co-planar sheets of  $\sim 0.3$  mm thickness through the measurement volume. The frequency-shifted emissions were detected through 450 nm and 410 nm optical filters (both with 10 nm bandwidth), using  $f_{\#}1.4$  lenses, onto two intensified CCD (ICCD) cameras. The gate widths of the cameras were set to 50 ns, prompt with laser excitation.

The 1064 nm laser beam, used for LII excitation, shared the same optical pathway as the beams from the dye lasers. The LII laser sheet was 20 mm in height with  $\sim 0.3$  mm thickness. The operating laser fluence was maintained at  $\sim 0.5$  J/cm<sup>2</sup>, which is within the plateau region (not shown), to ensure that LII signals observed are approximately independent of the laser fluence variation [94, 102]. The LII signal was detected through a 410 nm optical filter (10 nm bandwidth), using a  $f_{\#}1.4$  lens, onto another ICCD camera. The gate width of the camera was set to 100 ns, and the timing was set to be prompt to the LII excitation process. A delay generator was used to control the relative timing of the lasers and the camera detection gates (Section 3.3.2). The LII process was set to occur  $\sim 800$  ns after the NTLAF measurements.

The detection and timing schemes employed in this study are based upon the findings of Chapter 9, which assesses the technical feasibility of simultaneous measurements of soot and temperature using the joint NTLAF-LII approach. The detection and timing schemes are found to have avoided cross-talk between

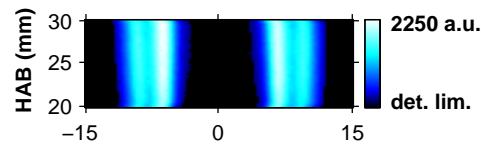
the NTLAF and the LII processes.

Following a similar methodology as Qamar *et al.* [102], calibration of the LII system was performed using laser extinction measurements. A flat-flame McKenna burner with a 25 mm diameter burner face was used to provide a uniform layer of soot. Here, a modulated continuous wave 1064 nm laser was used for laser extinction measurements to avoid extinction effects that may occur with the use of a 632 nm beam [142]. The soot extinction coefficient ( $Ke$ ) is taken to be 9.2, as measured by Williams *et al.* [112] who found that in the infrared spectrum for in-flame soot in a co-annular ethylene flame this value did not show any significant variation with flame height. The  $Ke$  value, predicted from the Rayleigh limit expression in combination with standard literature values for the soot refractive index (*e.g.*, [143]), was not used as there are valid concerns regarding the accuracy of this methodology [106, 112, 144].

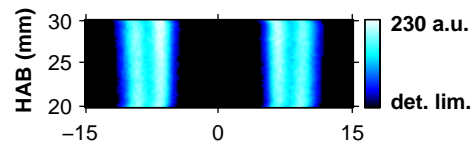
The processing of the images follows the image processing steps described in Section 3.4. Each of the images presented has been spatially matched and corrected for background and detector attenuation. The in-plane resolution of the images is  $\sim 260 \mu\text{m}$ , in each direction.

It is worth noting that the images presented for this laminar flame system were 150 shot-averaged to improve on the signal-to-noise ratio (SNR). Being a steady laminar flame system, there is no loss of information resulting from the averaging. No pixel binning was performed on the images to prevent degradation of the spatial resolution. It should be noted that, whilst the images presented here have been shot-averaged to achieve the best possible signal quality, the SNR of NTLAF technique is sufficient to be used for single-shot imaging, as demonstrated in the previous chapters.

(a) Stokes



(b) Anti-Stokes



(c) Soot

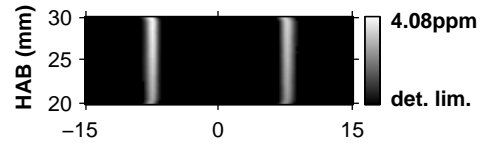
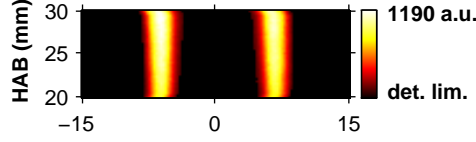


**Figure 8.1:** Typical averaged on-wavelength (a) Stokes, (b) anti-Stokes measurements and (c) LII soot volume fraction distribution in Flame 2 (Table 8.1). Laser propagates from left to right. HAB, height above burner. Dimensions of images in mm. The images are arbitrary scaled to their peaked values, which are indicated on their scales respectively

(a) Stokes



(b) Anti-Stokes

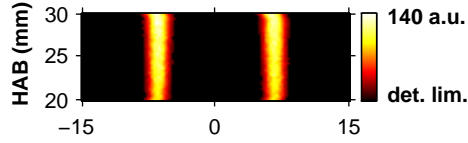


**Figure 8.2:** Typical averaged off-wavelength (a) Stokes and (b) anti-Stokes measurements in Flame 2 (Table 8.1). Laser propagates from left to right. HAB, height above burner. Dimensions of images in mm. The images are arbitrary scaled to their peaked values, which are indicated on their scales respectively.

## 8.3 Results and Discussion

### 8.3.1 On- and Off-Wavelength Measurements

#### 8.3.1.1 Typical On- and Off-Wavelength Measurements

Figure 8.1 shows the typical averaged on-wavelength measurements ( $I_{\text{on}}$ ), excited at 410 nm and 451 nm respectively, for the (a) Stokes and (b) anti-Stokes processes in Flame 2 (Table 8.1). These measurements comprise of the signal from the Indium fluorescence, and laser-induced interferences from the flame. Both measurements were recorded simultaneously under an operating fluence of  $\sim 0.01 \text{ J/cm}^2$ . Figure 8.1(c) presents the averaged soot volume fraction distribution of the same flame, excited at 1064 nm, and measured simultaneously with the on-wavelength measurements. The figure shows that the soot volume fraction for Flame 2 peaks at 4.08 ppm. The images presented represent an area of 10 mm high and 30 mm wide, taken at a height above burner (HAB) centred at 25 mm.

Figure 8.2 shows the typical averaged off-wavelength measurements ( $I_{\text{off}}$ ) for

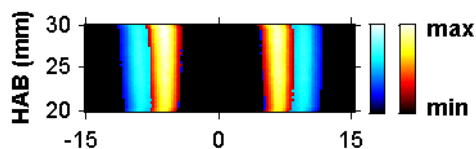
the (a) Stokes and (b) anti-Stokes processes in Flame 2 (Table 8.1). The off-wavelength measurements are defined here as the measurements obtained with the excitation laser detuned, but with the detection wavelength that was unchanged relative to the NTLAF process. It is important to note that no signal was detected in non sooting flame conditions when the lasers were tuned off-wavelength, indicating that the indium fluorescence does not contribute towards off-wavelength measurements observed here. These images were recorded under the same operating fluence as the on-wavelength measurements; only, the wavelength has been shifted slightly to detune it from the resonance of Indium. These images therefore correspond to the extraneous interferences, which would also contribute to the measurements shown in Figure 8.1. It is worth noting that even though the on- and off-wavelength measurements were performed at the same laminar flame condition *i.e.* Flame 2, it was not possible to collect these measurements concurrently with the present experimental setup. Their simultaneous measurement would require two additional tunable lasers and cameras.

It is worth noting that the on- and off-wavelength measurements presented here are given in arbitrary units (a.u.) since the strength of the measurements is dependent on the details of the optical arrangement. Nevertheless, a relative comparison of the off-wavelength with the on-wavelength measurements can be made, if the excitation characteristics of the off-wavelength measurements are assumed to be sufficiently broadband as to be insensitive to the slight changes in the linewidth associated with the change in the excitation frequency.

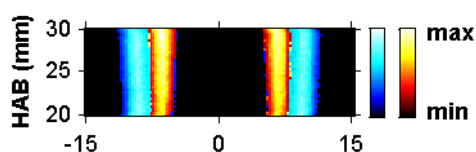
Figure 8.3 presents an overlay of the on- and off-wavelength measurements from Figure 8.1 and Figure 8.2, respectively. It is evident that the off-wavelength measurements overlap a narrow portion on the inner fuel-rich side of the broader on-wavelength measurements. The flame front can be identified from the region of highest intensity in the on-wavelength measurements, since this approximately marks the region with the highest temperature (Chapter 6). These observations suggest that the source(s) of the observed off-wavelength measurements is only associated with the fuel-rich side of the reaction zone, and not with the flame front or oxidizing region.

Figure 8.4 shows the overlapping of the off-wavelength measurements and the LII image of soot volume fraction for both the Stokes and anti-Stokes processes. It

(a) Stokes

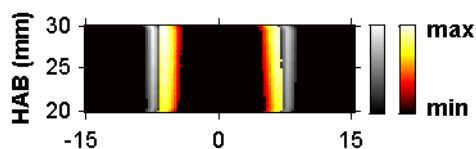


(b) Anti-Stokes



**Figure 8.3:** Typical averaged on-wavelength measurements, with off-wavelength measurements overlaid for (a) Stokes and (b) anti-Stokes processes in Flame 2 (Table 8.1). On-wavelength: Blue—White. Off-wavelength: Red—White. HAB, height above burner. Dimensions of images in mm.

(a) Stokes



(b) Anti-Stokes

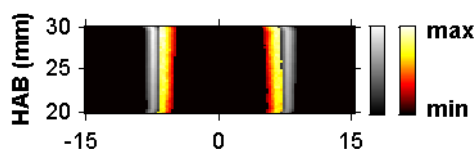


**Figure 8.4:** Typical averaged off-wavelength measurements with LII soot volume fraction overlaid for (a) Stokes and (b) anti-Stokes processes in Flame 2 (Table 8.1). Soot: Grey—White. Off-wavelength: Red—White. HAB, height above burner. Dimensions of images in mm.

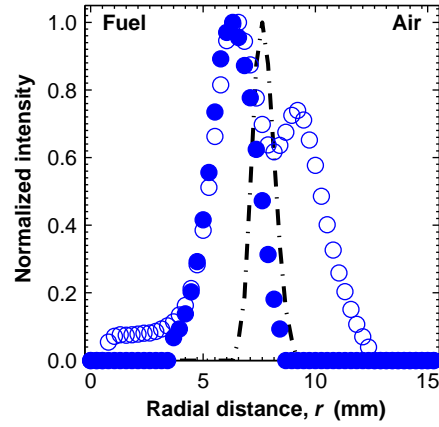
is apparent that the locations of the off-wavelength measurements are distinct from the soot regions and are also on the fuel-rich side of the soot sheet. The difference in the locations of the measurements implies that soot interferences, such as spurious scattering and laser-induced incandescence, do not contribute significantly to the off-wavelength measurements. Rather, such spurious scattering from the soot is effectively suppressed by the optical arrangement employed. The observation also indicates that the chosen fluence for these measurements is sufficiently low to avoid soot incandescence, which is consistent with the findings reported in the previous studies (*e.g.*, [94]), despite operating in the nonlinear excitation regime.

It can also be seen from Figure 8.4 that the off-wavelength measurements are observed to occur at a similar location for both the Stokes and anti-Stokes processes, suggesting that the same source(s) is likely to be responsible for each. Furthermore, since the off-wavelength measurements are detected for both the Stokes and anti-Stokes processes, it can be inferred that these laser-induced emissions are characterized by a broad spectral range.

The averaged distribution of the on- and off-wavelength measurements, and of the soot volume fraction are normalized in Figure 8.5. These averaged radial profiles were extracted at a HAB of 25 mm, and are normalized to their peak values. From Figure 8.5, it can be seen that the off-wavelength measurements peak at a radial location ( $r$ ) of  $\sim 6.5$  mm and have a FWHM spread of  $\sim 2.3$  mm. By contrast, the soot particles peak at  $r \approx 7.5$  mm and are confined to a thinner region (FWHM  $\approx 1.3$  mm). A close inspection of Figure 8.5 also reveals that the off-wavelength measurements peak at the same radial location ( $r \approx 6.5$  mm) as the onset of the soot. This observation suggests that the source(s) that resulted in the observed off-wavelength measurements participates in the soot formation process, since the consumption of the species coincides with the appearance of the soot particles. It is also consistent with the knowledge that soot precursors are found on the fuel-rich side of the soot layer.

Measurements from both Stokes and anti-Stokes processes are observed to have qualitatively similar characteristics throughout the present study. Hence, only results obtained for the anti-Stokes process are presented and discussed in the subsequent sections.

(a) Stokes



(b) Anti-Stokes

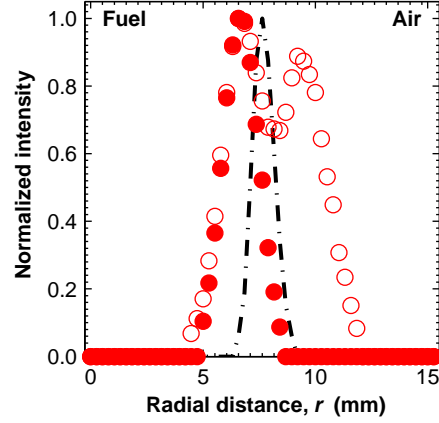


**Figure 8.5:** Average radial profiles for the (a) Stokes and (b) anti-Stokes processes extracted at a HAB of 25 mm in Flame 2 (Table 8.1). Open circles: on-wavelength measurements. Dots: off-wavelength measurements. Dashed line: soot volume fraction. These radial profiles have been normalized arbitrarily to their peak values.

### 8.3.1.2 Effect of Laser Fluence

Figure 8.6 presents the averaged radial profiles for the on- and off-wavelength measurements in Flame 2 (Table 8.1) at a HAB of 25 mm, at four different laser fluences. To generate this plot, the laser fluence was varied by the addition of neutral density filters of differing optical density (OD) into the beam. This approach allows the variation in intensity while maintaining consistent optical properties of the beam. Both the flame condition and Indium seeding concentration were held constant. The radial location of the peak soot volume fraction is indicated on the figure with a vertical dotted line.

A consistent trend is evident in Figure 8.6, with the intensities of both the on- and off-wavelength measurements found to reduce with decreasing laser fluence. In general, each of the on-wavelength measurements is observed to exhibit a qualitatively similar trend. The on-wavelength measurements are observed to peak (air-side peak) at a radial location between the air side and the position of the maximum soot volume fraction. Also, a secondary peak (fuel-side peak) appears at an intermediate position between the soot zone and the fuel-rich side. The off-wavelength measurements exhibit qualitatively similar trends to the findings discussed earlier from Figure 8.5.

The peaks for the on-wavelength measurements are observed to display dissimilar trends when different laser fluences are used. For the case of laser fluence of  $0.010 \text{ J/cm}^2$  and  $0.008 \text{ J/cm}^2$ , the fuel-side peaks are observed to have a higher intensity than the air-side peaks. However, such characteristic does not persist and is found to have inversed for the case at lower laser fluences (*i.e.* laser fluence of  $0.003 \text{ J/cm}^2$  and  $0.001 \text{ J/cm}^2$ ). The difference in the dependency of the air-side and the fuel-side peaks on the laser fluences implies that the observed on-wavelength measurements are comprised of laser-induced emissions from species with dissimilar spectroscopic properties. A close inspection of the radial profiles in Figure 8.6 further reveals that the fuel-side peaks of the on-wavelength measurements are in good agreement with profiles of the off-wavelength measurements, with the local maxima of the fuel-side peaks and the off-wavelength measurements occurring at similar radial locations. The likeness of the profiles over the region suggests that the fuel-side peak of the on-wavelength measurements are mainly comprised of the laser-induced emissions from the same non-Indium

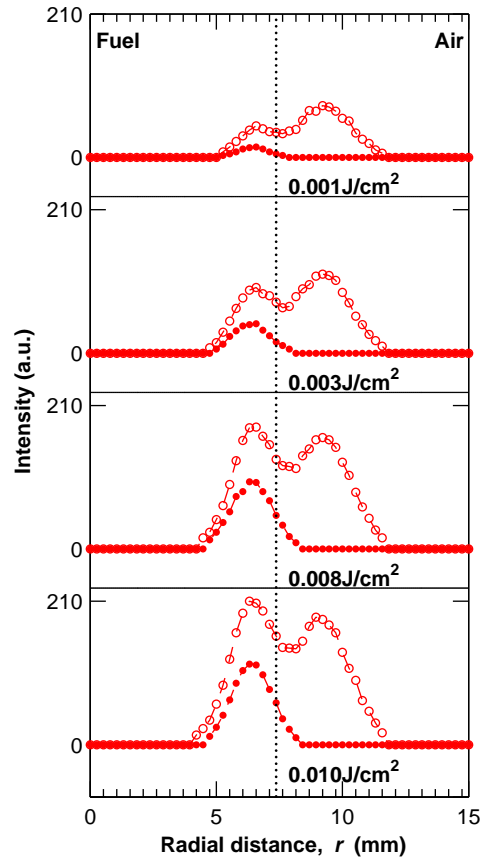


**Figure 8.6:** Averaged radial profiles for the on-wavelength measurements at four different laser fluences, extracted at a HAB of 25 mm in Flame 2 (Table 8.1). Anti-Stokes process. Open circles: on-wavelength measurements. Dots: off-wavelength measurements. Vertical dotted line: peak soot volume fraction location.

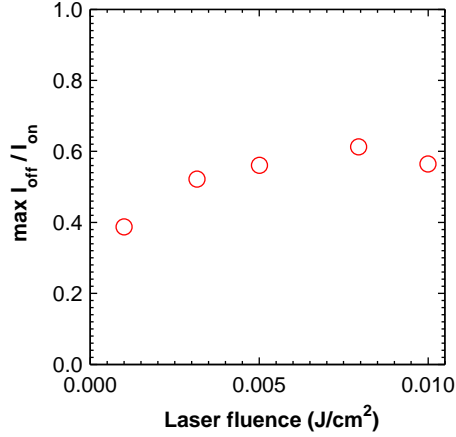


**Figure 8.7:** Maximum off-wavelength to on-wavelength measurements ratio as a function of laser fluence. Anti-Stokes.

source(s) responsible for the off-wavelength measurements.

The measured off-wavelength measurements in Figure 8.6 are found to be linearly proportional to the laser fluences used. Nonetheless, the magnitude of the on-wavelength measurements is also observed to decrease with the operating laser fluences. The relative magnitude of the maximum off-wavelength to on-wavelength measurements obtained from Figure 8.6 is therefore compared in Figure 8.7, as a function of laser fluence. It is evident from the figure the interference remains significant at all fluences. This observation implies that the laser-induced emissions from the non-indium source(s) are not an artefact of the operating laser fluence of NTLAF and are readily stimulated even at very low fluences. It is worth noting that the measurements obtained with linearity-limited laser fluence ( $6 \times 10^{-6}$  J/cm<sup>2</sup>) are plagued by poor SNR, for the nonpremixed flame conditions used here, thus preventing derivation of useful information.

Polycyclic aromatic hydrocarbons (PAH) [140, 141, 145, 146] and condensed species (CS) [147, 148, 149] have been reported to form readily in fuel-rich zones and are deduced to play important roles in soot formation processes. The emissions from both PAH and CS are characterized by broad spectra range and are reported to exhibit both Stokes (red-shifted) and anti-Stokes (blue-shifted) components [150, 151]. The similarities between the characteristics of the off-wavelength measurements and the findings of the previous studies suggest that

the laser-induced emissions from PAH and CS should be considered in seeking to identify the cause of the interference. Other studies, however, have reported that PAH emission in the visible spectrum is negligible [148], indicating that CS is more likely to be the species causing the off-wavelength measurements. Nevertheless, it is possible that the spectroscopic properties of the PAH might be influenced by the high temperature flame environment, shifting in the emission significantly towards visible [149, 152]. Therefore, the contribution of the PAH emission in perturbing the NTLAF measurements cannot be ruled out completely.

### 8.3.1.3 Effect of Equivalence Ratio

Figure 8.8 presents the averaged radial profiles of on- and off-wavelength measurements in Flame 1 to Flame 5 (Table 8.1) at a fixed operating laser fluence of  $\sim 0.01 \text{ J/cm}^2$ . Again, these profiles were extracted at a HAB of 25 mm in all flames. Measurements are presented as a function of radial distance from the peak of the soot volume fraction ( $r'$ ). This identifies the variations relative to the flame front. From Figure 8.8, it can be seen that the influence of the fuel-rich interference peak in the on-wavelength measurements is greater in the richer flames than in the leaner flames. That is, the richer the flame, the more intense the off-wavelength measurements. This is consistent with the deduced importance of PAH and CS since both are formed preferentially under richer conditions.

From Figure 8.8, it can be seen that there is an enhancement in the intensity of the on-wavelength measurements, as the flame becomes leaner. This observation appears to be opposite to the general view that the neutral Indium atoms are generated more efficiently in fuel-rich zones [59, 77]. The processes by which the neutral Indium atoms are converted from Indium chloride solutions are complex, as described in Section 2.3.3. Flame 2 to Flame 5 are fuel-rich flames slightly premixed with air, so have wide reaction zones. The various processes involved in the generation of Indium atoms are therefore allowed more time to proceed. Additionally, the efficiency of the desolvation step is also expected to increase in the leaner flames, which have more favorable heat release profiles. The interactions of these two effects may have compensated for the decrease in the efficiency of Indium formation in leaner flames. Factors such as the requirement for the activation of Indium within flame front [65] or the possible formation of carbon-

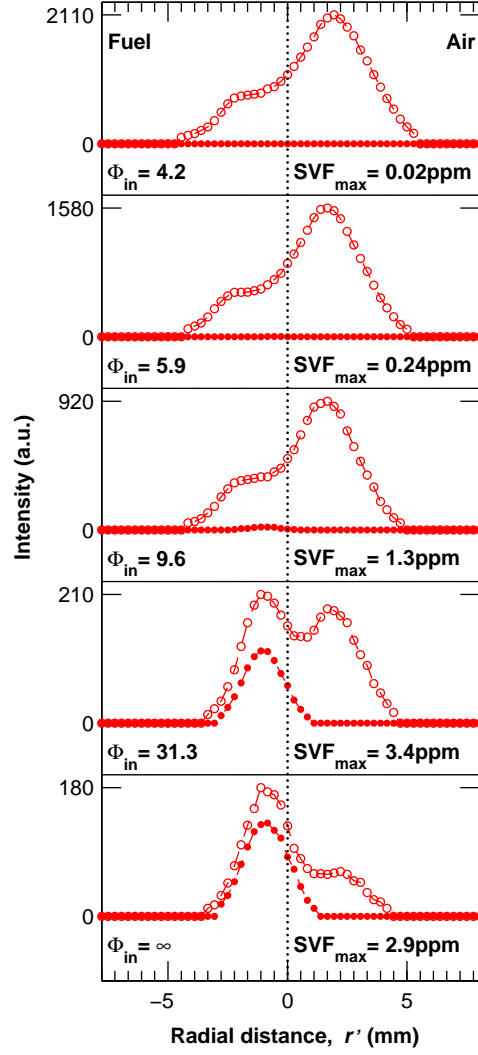


**Figure 8.8:** Averaged radial profiles as a function of radial distance from peak soot volume fraction location, extracted at a HAB of 25 mm in Flame 1 to 5 (Table 8.1). Anti-Stokes process. Open circles: on-wavelength measurements. Dots: off-wavelength measurements. Vertical dotted line: peak soot volume fraction location.

containing Indium compounds in sooty flames, which result in decreased Indium atom formation efficiency [93], may also contribute to the observed trends.

It is worth mentioning that, despite an overall enhancement in the intensity of the on-wavelength measurements from fuel-rich to fuel-lean, there is no substantial difference in the general shapes of the profiles. Neglecting the cases such as  $\Phi=\infty$  and 31.3, where the on-wavelength measurements are highly perturbed by the extraneous emissions from non-Indium sources, all of the curves are found to pass through a maximum at an intermediate position between the soot zone and air side. Again, the shapes of these curves are expected to reflect the composite effects of the various factors discussed previously.

## 8.3.2 Potential Schemes to Correct for or Circumvent Interferences

### 8.3.2.1 Off-wavelength measurements

To investigate approaches to correct for the aforementioned interferences, Figure 8.9 presents the averaged radial profiles that result from the subtraction of the extraneous interferences, *i.e.* off-wavelength measurements, from the on-wavelength measurements in Figure 8.7 when changing laser fluence. It can be seen that each of the averaged radial profiles exhibit qualitatively similar trends to the on-wavelength measurements in Figure 8.8 that are observed to be least affected by the extraneous interferences (*i.e.*  $\Phi=4.2$  and 5.9). This observation suggests that the off-wavelength measurements can potentially be used to account/correct for the interferences present, over a range of laser fluences. Also, this observation supports the earlier assumption in Section 8.3.1.1 that the off-wavelength measurements are likely to be insensitive to the changes in linewidth associated with slight detuning of the laser.

### 8.3.2.2 Off-Resonance Measurements

To investigate approaches to circumvent the aforementioned interferences, the averaged distribution of the off-resonance and the corresponding off-wavelength

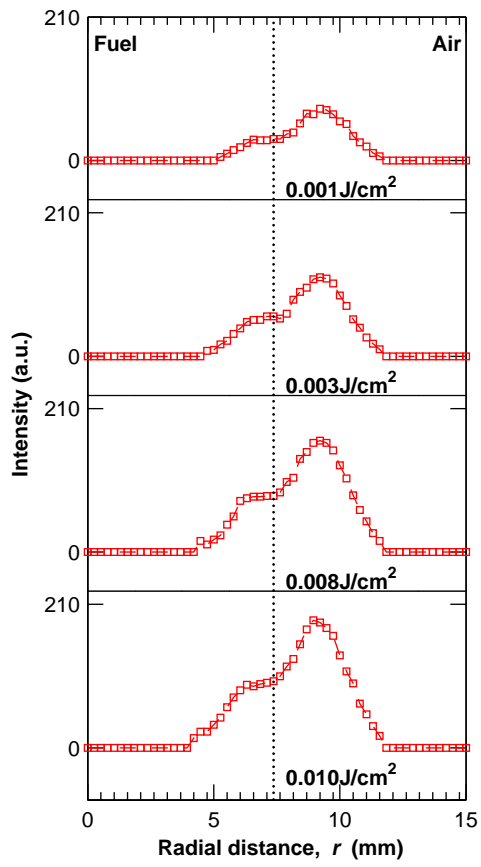


**Figure 8.9:** Averaged radial profiles for the corrected on-wavelength measurements at four different laser fluences, extracted at a HAB of 25 mm in Flame 2 (Table 8.1). Anti-Stokes process.

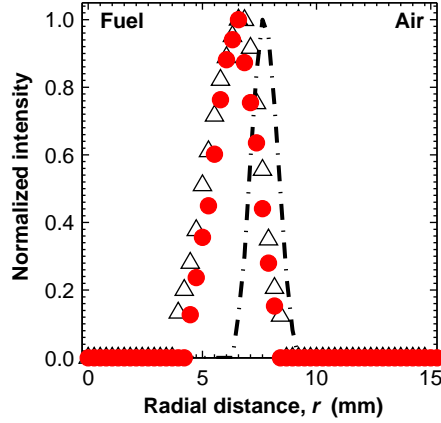


**Figure 8.10:** Averaged radial profiles extracted at a HAB of 25mm in Flame 1 (Table 8.1). Anti-Stokes process. Dashed line: soot volume fraction. Dots: off-wavelength measurements. Open triangles: off-resonance measurements. These radial profiles have been normalized arbitrarily to their peak values.

measurements in Flame 1 (Table 8.1) are presented in Figure 8.10 for the anti-Stokes process. The off-resonance measurements are defined here as the measurements collected with the on-wavelength excitation, but with detection wavelength that was detuned relative to the NTLAF process. The LII soot volume fraction distribution for the flame is overlaid as well. The off-resonance measurements were collected with the use of a 430 nm filter (10 nm bandwidth) in conjunction with on-wavelength excitation *i.e.* 450 nm excitation for anti-Stokes process.

From Figure 8.10, it is evident that the both the off-resonance and off-wavelength measurements show qualitatively similar features. It is worth noting that the off-resonance and off-wavelength measurements are found to differ quantitatively, as expected, since different detection optics were used for the collection of each of the measurements. These findings suggest that the off-resonance measurements would be more useful for identification, rather than correction, of the regions of NTLAF images that are identified to be significantly affected by the extraneous interferences present. It is also important to note that the off-resonance and off-wavelength measurements for the Stokes process (not shown here) are found to display similar characteristic as well.

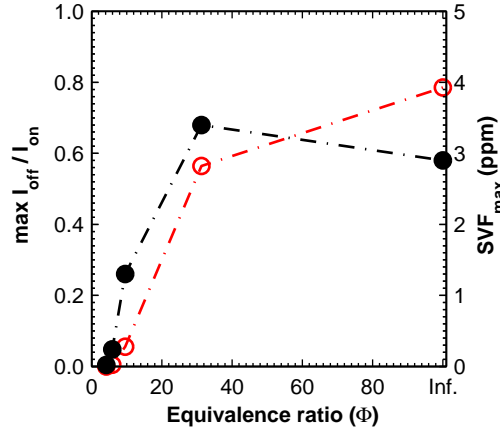


**Figure 8.11:** Comparison of the maximum off-wavelength to on-wavelength measurements ratio and the maximum soot volume fraction at different flame equivalence ratios. Anti-Stokes. Open circles: maximum off-wavelength to on-wavelength measurements ratio. Dots: maximum soot volume fraction.

### 8.3.2.3 Equivalence Ratio

Figure 8.11 presents the dependence on the flame equivalence ratio of the maximum off-wavelength to on-wavelength measurements ratios. These data were extracted from the fuel-rich peak between the fuel and soot zones where the off-wavelength measurements are found to be significant. Also presented are the corresponding maximum soot volume fractions ( $\text{SVF}_{\text{max}}$ ). It can be seen that there is a strong, although not absolute, correlation between the amount of soot and interference, as expected. Clearly, the relationship between these two parameters is not absolute and will depend on factors such as fuel type and strain [153]. Nevertheless, it is demonstrated that measurements without the need for correction will be possible for flames with sufficiently low yet still useful soot loadings. Specifically, it can be seen that the maximum interference to the total emission ratio is lower than 0.05 when the flame equivalence ratio is less than  $\Phi=9.6$  and when the  $\text{SVF}_{\text{max}}$  is  $\sim 1.3$  ppm for this fuel. Given the expected dependence of this relationship on fuel type and experimental conditions, it is desirable to perform a similar check for specific conditions of interest.

## 8.4 Summary

The applicability of the nonlinear excitation regime two-line atomic fluorescence (NTLAF) for the measurements in flames with high soot concentrations has been assessed. The contribution of the extraneous interferences from non-Indium sources towards the NTLAF measurements in flames with high soot loadings is measured. The off-wavelength measurements show that the interference is significant from soot precursors, but not from soot itself. Additionally, the comparison of the spatial locations of the various peaks of the measurements suggests that the interference is derived predominantly from condensed species (CS) and perhaps also from polycyclic aromatic hydrocarbons (PAH). It has been shown it is possible to use the off-wavelength measurements to correct for the extraneous interferences. It has also been shown that off-resonance measurements can be used to identify and isolate the regions of the NTLAF data that are found to be significantly affected by extraneous interferences. The NTLAF can be expected to perform reliably, without the need for correction, in selected flame conditions with low yet useful soot loadings. All these results justify more work to directly evaluate the efficacy of the correction schemes on the accuracy of the measurements in flames with high soot loadings. These correction schemes would allow the extension of the usable range of the NTLAF technique to flames of higher soot loadings.

## Chapter 9

# Simultaneous Application of NTLAF and LII

In this chapter, the technical feasibility of the nonlinear excitation regime two-line atomic fluorescence (NTLAF) technique to be used concurrently with laser-induced incandescence (LII) for simultaneous imaging of temperature and soot concentration in sooty flames is investigated.

### 9.1 Introduction

Temperature characterizes the heat transfer process and controls the chemical and physical processes within a flame [21]. Soot concentration measurements within a flame, on the other hand, provide valuable insights to the study of soot growth and radiant transport [101, 102, 106]. Temperature and soot have an inherent coupled dependence since temperature depends on soot concentration due to heat transfer through radiation. At the same time, the temperature affects the formation and destruction of soot in flame [153]. Therefore, a detailed understanding of soot requires the knowledge of temperature and vice versa. Simultaneous planar measurements of temperature and soot concentration within a flame environment are therefore essential to shed light on the complex processes associated with soot.

In this chapter, the technical feasibility of conducting simultaneous single-shot

temperature imaging using NTLAF and soot concentration measurements using LII technique is investigated. These techniques are selected with a view towards future application in turbulent environments as they offer the advantage of planar imaging. The concurrent application of the NTLAF and LII techniques has the potential to result in optical interference and it is therefore necessary to demonstrate that simultaneous imaging with these methods is possible. This chapter also presents the measurements to evaluate the fluorescence, temperature and soot concentration single-shot images.

## 9.2 Experimental Arrangement

### 9.2.1 Burner and Seeding Arrangement

A laminar premixed, a laminar nonpremixed and a wrinkled laminar nonpremixed flames were chosen to provide media with distinct features to be used for these evaluations. A circular ceramic honeycomb matrix was used to generate the required flames. The burner is described in Section 3.1.1. In brief, the burner consists of a honeycomb matrix encased in a brass annular tube. A second annular tube is aligned to provide co-annular flow. The burner was used for calibration and to stabilize the premixed and nonpremixed flames examined in this study. The flame was shrouded by a nitrogen co-flow when operated in premixed mode. No co-flow was introduced when operated in the nonpremixed mode. To prevent buoyancy-driven instability, a stabilization plate with a diameter of 100 mm was mounted 30 mm above the burner face. Industrial grade ethylene ( $>99.5\%$  vol.  $\text{C}_2\text{H}_4$ ) was used as fuel.

Indium Chloride was dissolved in methanol as the source of the Indium atoms for excitation using the NTLAF technique. The seeding solution was introduced into the fuel stream as an aerosol generated by a pair of pneumatic nebulizers mounted at the base of the burner. The fallout of the aerosol within the burner was observed to be considerable as a result of the type of nebulizer used. Therefore, a seeding solution of higher Indium Chloride concentration (7.5 mg/mL) was needed to yield sufficiently good signal. The surrounding air was not seeded with Indium, as this does not improve the level of signal, and would lead to additional

impact of the solvent on the flame. The molar percentage of the solvent in the inlet gases was  $\sim 3\%$ .

In the nonpremixed mode, the majority of the air flow was turned off, leaving sufficient air to generate aerosol from the nebulizers to allow seeding of the flow. The corresponding air fuel ratio was  $\sim 2.7:1$  by volume, thus exhibiting the same traits as nonpremixed flames. The large cross sectional area of the burner gave a low strain rate (flame time constant,  $D/U=2.33$  s [129]), which resulted in spatially wide flames with distinguishable features.

### 9.2.2 Optical Layout

The experimental arrangement used for this study follows the setup depicted in Figure 3.9. The experimental details are similar to that presented in Chapter 8, with the exception that the laser fluence of the LII laser was operated at  $\sim 0.9$  J/cm<sup>2</sup>. This was to ensure that the LII signals observed are approximately independent of the fluence variation [94, 102]. The LII signals were calibrated using laser extinction measurements, with a chopped, continuous-wave 1064 nm beam, as described in Chapter 8. The soot extinction coefficient ( $Ke$ ) was taken to be 9.2, following the work of Williams *et al.* [112].

A delay generator was used to control the relative timing of the lasers and the camera detection gates, as detailed in Section 3.3.2. The LII process was delayed  $\sim 800$  ns after the NTLAF measurements, and was found to avoid cross-talk of the LII with the NTLAF imaging. This delay is small in relation to the physical and chemical time-scales of the flame, ensuring that the NTLAF and LII measurements were virtually simultaneous. The LII process was set to occur after the NTLAF process since the temporal decay (hundreds of nanoseconds) of the LII signal is slower than that of the fluorescence (tens of nanoseconds) [146]. Also, the laser ablation of the soot may invoke other influences, such as laser modulated particulate incandescence and vaporization [24], on the flame.

It is noted that whilst LII is reasonably well-established, recent studies [154, 155] have revealed that primary particle size may significantly influence soot volume fraction measurements. The implementation of a particle size correction scheme for an improved measurement of soot concentration is desirable, no such

approach has been demonstrated to be feasible in turbulent flames, however. Additionally, the semi-quantitative measurements provided by single-color LII technique is adequate for the purpose of this study. Single-color LII was therefore used for soot concentration measurements.

The processing of the images follows the image processing steps described in Section 3.4. Each of the images presented has been spatially matched and corrected for background and detector attenuation. The in-plane resolution of the images is  $\sim 380 \mu\text{m}$ , in each direction.

## 9.3 Results and Discussion

### 9.3.1 Laminar Premixed Flame

Figure 9.1(a) and Figure 9.1(b) show typical single-shot Indium Stokes and anti-Stokes images, which are recorded simultaneously under a spectral irradiance of approximately  $1.5 \times 10^6 \text{ W/cm}^2/\text{cm}^{-1}$ . The images presented are 20 mm high and 50 mm wide, centred at a 10 mm height above burner (HAB). The equivalence ratio ( $\Phi$ ) of the flame presented in the figure is  $\sim 2.5$ . The SNR (ratio of the signal strength to the standard deviation of the signal in a uniform region of flame) of the Stokes and anti-Stokes images are  $\sim 20:1$  and  $6:1$ , respectively. No image smoothing was applied here to reduce inter-pixel noise, as this can degrade spatial resolution and give false information on the SNR of the images.

Applying the NTLAF theory to the fluorescence images yields the deduced temperature image in Figure 9.1(c), which has an average value of  $\sim 1300 \text{ K}$ , and a SNR of  $\sim 17:1$  (leading to a precision of  $\sim 60 \text{ K}$ ). The temperature is a result of the combined heat loss to the stabilization plate, burner and to the surrounds by radiation from flame and soot.

Both the Stokes and anti-Stokes fluorescence images exhibit non-uniformity across the imaged region. This is attributed mainly to the disproportionate seeding and formation of neutral Indium atoms within the flame, as the non-uniformity of the fluorescence images is observed to follow the burner when rotated. Additionally, laser measurements indicate that extinction due to soot is  $\sim 5\%$  in the

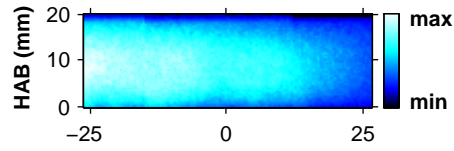
present flame. This was deduced from other measurements showing that the self-absorption from Indium in non sooting flames was negligible. Since extinction is wavelength dependent, and both Stokes and anti-Stokes excitations are similar in wavelength, the differences in the extinction affect both images approximately equally, and do not affect the inferred temperature measurement. Evidence of the non-uniformity of the fluorescence images having a negligible effect on the deduced temperature image is seen in Figure 9.1(c). A constant temperature field is observed across the width of the burner, with no apparent temperature difference across the image. Furthermore, the path length of this flame is significantly greater than that typically encountered in nonpremixed flames and therefore the effects of the absorption (governed by the optical thickness) are expected to be conservative relative to many future flames of interest (*viz.* turbulent nonpremixed flames).

Tuning the laser off-wavelength reveals that interferences due to soot are insignificant ( $\lesssim 1\%$ ) in both Stokes and anti-Stokes images for the present flame. This demonstrates that the filtering capability of the NTLAF is adequate in suppressing soot interference, such as scattering.

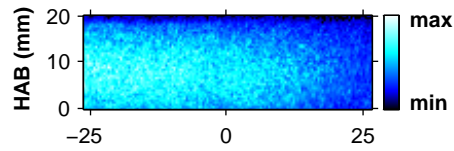
Figure 9.1(d) represents the two-dimensional soot volume fraction distribution measured simultaneously with the fluorescence and temperature images shown in Figure 9.1(a-c). The figure shows that the soot volume fraction of the present flame peaks at  $\sim 0.07$  ppm. The uniformity of the temperature field (Figure 9.1(c)) appears to be unaffected by the soot concentration distribution. This suggests that, for the selected flame conditions, flame temperature changes little with height above burner (HAB) despite the emergence of soot in the downstream region of the flame.

For comparison purposes, a further re-evaluation of the measured soot volume fraction based on the  $Ke$  value of 4.9, estimated from the complex refractive index of  $1.57-0.56i$  [106, 143], gives a peak value of  $\sim 0.14$  ppm. It is important to note that the flames produced by the present burner are sensitive to the geometry and the placement of the plate. Therefore, it is not possible to directly compare the current measurement with previous studies. However, the observed values are similar to those of a laminar premixed ethylene- air flame with a similar arrangement, as measured by Menon *et al.* [156].

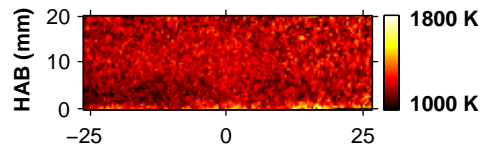
(a) Stokes fluorescence



(b) Anti-Stokes fluorescence



(c) Temperature



(d) Soot volume fraction

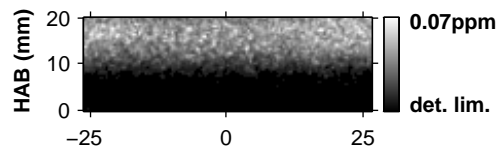


**Figure 9.1:** Simultaneous single-shot images for a laminar premixed ethylene-air flame. (a) Stokes, (b) anti-Stokes Indium fluorescence (c) NTLAF temperature, and (d) LII soot volume fraction. Laser propagation from left to right. HAB, height above burner. Dimensions of images in mm.

### 9.3.2 Laminar Nonpremixed Flame

Figure 9.2(a) and Figure 9.2(b) shows typical single-shot Stokes and anti-Stokes images recorded with the burner operating in nonpremixed mode, respectively. Good signal is detected across the region of interest, namely the reaction zone. The regions without signal on either side of the reaction zone are due to a paucity of neutral Indium atoms there, as discussed in Chapter 6.

The temperature image (Figure 9.2(c)) is inferred from the fluorescence images, using the calibration constants determined from the laminar premixed flame. The temperature profile exhibits a steep temperature gradient, as expected. The temperature threshold of the image is found to be  $\sim 1000$  K, below which the Indium formation process from the Indium Chloride solution does not become significant (Chapter 6). Hence, those parts of images with no data are caused by temperature and/or chemical effects that are not favourable for the production of neutral Indium atoms from the Indium Chloride.

Collected simultaneously with the temperature, the corresponding single-shot soot volume fraction distribution is presented in Figure 9.2(d). The peak soot volume fraction value ( $\sim 0.3$  ppm) for the laminar nonpremixed flame is found to be higher than that measured for the laminar premixed flame ( $\sim 0.07$  ppm), which is to be expected.

Exploiting the simultaneity of the imaging measurements, Figure 9.2(e) shows the overlapping nonpremixed flame temperature field and the corresponding single-shot soot distribution. A color scale is used for the temperature and a grey shading is specified for the soot sheet to highlight different regimes within the nonpremixed flames highlighted in the figure. From Figure 9.2(e), it is apparent that temperature data is available from the NTLAF at all regions where the soot is present. The soot regions are observed to be narrow and are confined to a restricted temperature range. This observation demonstrates that the NTLAF technique is well suited to investigate the coupled dependencies between temperature and soot in flames.

The single-shot temperature-soot distribution exhibit the qualitative features expected for a laminar nonpremixed flame [153]. The soot sheets are observed to be located at radial locations on the fuel-rich side of the peak temperature. The ob-

servation that the soot sheets are spatially separated from the high temperature regions, *i.e.*, the reaction zones is consistent with previous studies [157].

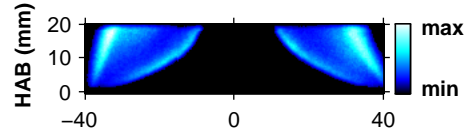
### 9.3.3 Wrinkled Nonpremixed Flame

Figure 9.3 presents the equivalent sets of images for a wrinkled nonpremixed case. The turbulent motions deduced from Figure 9.3 were generated by removing the stabilization plate from the burner. An external air supply was also used to physically induce a cross-flow to the flame. These figures highlight the benefits of planar imaging in providing physical insights in the study of rapidly varying two-dimensional or three-dimensional flows [54, 64].

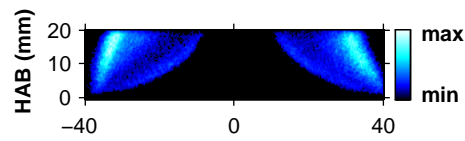
Evident from Figure 9.3(e) is that the turbulent motions result in both spatial broadening and thinning of the high temperature zones and soot sheet, relative to the profiles observed in the laminar nonpremixed case. The soot concentration is observed to vary along the high temperature zones. Typically, increasing the strain in a laminar flame would lead to a reduction in soot concentration. However, it is evident that the influence of the turbulent motions on the present flame is complex, with no simple or constant relationship between temperature and soot volume fraction. It is also interesting to note that, as in the steady case, the soot sheet does not overlap the highest temperature part of the flame. However, in the wrinkled case, the soot sheet is not found radially inside of the highest temperature peak; rather the soot sheet abuts the high temperature sheet, but at a point of high curvature. All these observations are consistent with view that the location and the dynamics of the soot formation are closely related to the motions of the large-scale structures [157].

The influence of wrinkling in the present system on the relationship between soot volume fraction and temperature in laminar nonpremixed flames is further examined in Figure 9.4, which presents a scatter plot of soot volume fraction versus temperature for the present flame cases. It is clear that the flame with wrinkled structure has a much wider range of soot volume fraction values and is typically associated with lower temperatures. The details of this influence are expected to be case specific, rather than general. However, it demonstrates the need for simultaneous planar measurements to assess the relationship in detail.

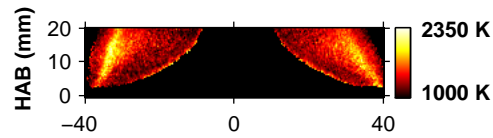
(a) Stokes fluorescence



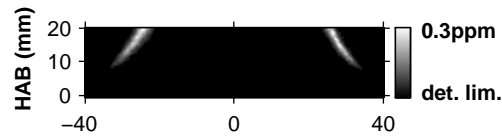
(b) Anti-Stokes fluorescence



(c) Temperature



(d) Soot volume fraction



(e) Temperature and soot volume fraction

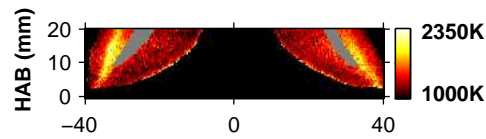
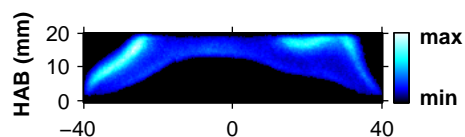
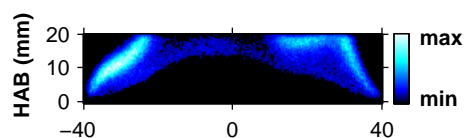


**Figure 9.2:** Simultaneous single-shot images for a laminar nonpremixed ethylene-air flame. (a) Stokes, (b) anti-Stokes Indium fluorescence, (c) NTLAF temperature, (d) LII soot volume fraction and (e) instantaneous temperature field with location of soot overlaid (in grey). Laser propagation from left to right. HAB, height above burner. Dimensions of images in mm.

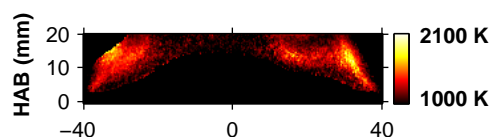
(a) Stokes fluorescence



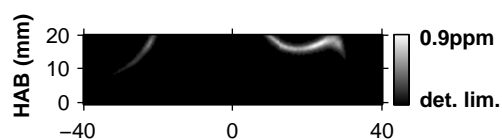
(b) Anti-Stokes fluorescence



(c) Temperature



(d) Soot volume fraction



(e) Temperature and soot volume fraction

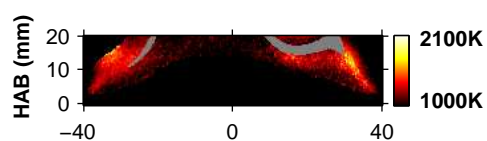


**Figure 9.3:** Simultaneous single-shot images of a wrinkled nonpremixed ethylene-air flame. (a) Stokes, (b) anti-Stokes Indium fluorescence, (c) NTLAF temperature, (d) LII soot volume fraction and (e) instantaneous temperature field with location of soot overlaid (in grey). Laser propagation from left to right. HAB, height above burner. Dimensions of images in mm.

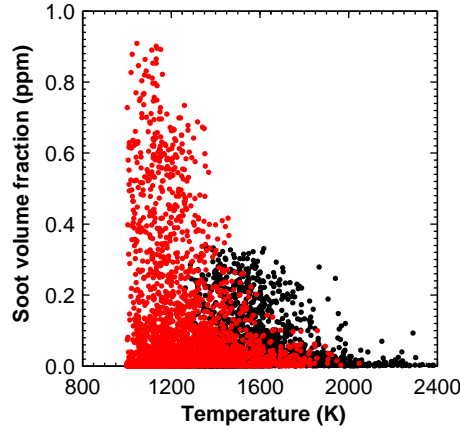


**Figure 9.4:** Soot volume fraction as a function of temperature for laminar non-premixed and wrinkled nonpremixed flames. Black: Laminar flame. Red: Wrinkled flame.

## 9.4 Summary

In this chapter, the technical feasibility of conducting simultaneous single-shot imaging of temperature and soot concentration in sooty flames with nonlinear excitation regime two-line atomic fluorescence (NTLAF) and laser-induced incandescence (LII) has been assessed. The measurements are performed in laminar premixed and nonpremixed flames, and in a wrinkled nonpremixed flame. No significant interference of the two measurements on each other is observed. All the observed features of the flames were found to be qualitatively consistent with previous work. The images reveal that, while NTLAF has a limited operating range, this range is sufficient to span all regions with soot. This study also demonstrates the applicability of joint NTLAF-LII measurements to assess the coupled dependency of temperature and soot in sooty flame.

This page intentionally left blank.

# Chapter 10

## Summary and Conclusions

The aim of this work was to develop the two-line atomic fluorescence (TLAF) technique, with neutral Indium atom as the seeded thermometric species, to permit instantaneous imaging in sooty flames. The four specific aims addressed in this dissertation were: (1) to assess the capability of the existing linear TLAF technique in providing single-shot temperature imaging; (2) to improve the existing linear TLAF technique to achieve sufficient signal-to-noise ratio (SNR) to permit single-shot temperature imaging; (3) to assess the capability of the developed technique to perform measurements in flames with high soot concentration, and (4) to demonstrate the technical feasibility of the developed technique to be used concurrently with other laser diagnostic method for simultaneous measurements in sooty flames.

In this work, the limitation of the existing TLAF in the linear excitation regime has been shown to be related to low SNR, thus preventing useful single-shot imaging. The SNR of the deduced single-shot temperature image is found to be  $\sim 8:1$ , which corresponds to a precision of  $\sim 250$  K, in a typical hydrocarbon flame. Shot-averaging is found to have improved the SNR of the deduced average temperature image to  $\sim 20:1$ , which corresponds to a precision of  $\sim 100$  K. In laminar steady flames, there is no other significant loss of information resulting from the averaging and thus the limitation of measuring mean temperature has been acceptable. However, in the context of the turbulent flames that are more dynamic in nature, such average data do not provide information, such as

instantaneous gradients or statistics, which are important for the understanding of such flames.

The TLAF derivations have been extended from the linear excitation regime (Equation 4.1) to the nonlinear fluence regime (Equation 5.1) to achieve measurements with improved signal quality to facilitate instantaneous imaging. The SNR of the deduced nonlinear excitation regime TLAF (NTLAF) single-shot temperature image is measured to be  $\sim 20:1$ , which corresponds to a precision of  $\sim 100$  K. The NTLAF technique is also shown to be able to resolve the temperature profile across a range of equivalence ratios for natural gas, hydrogen, and ethylene laminar premixed flames, with deviation from thermocouple measurements not exceeding 100 K, and typically  $\sim 30$  K. Temperature imaging with a precision of  $\sim 100$  K compares favorably with alternative thermometry techniques but with the advantage of being suited to flames containing soot. Although, the NTLAF technique is susceptible to the effects of differing composition, the small amount of uncertainty associated with the determination of the constants is far outweighed by the ability to collect large-dimension single-shot images with superior signal.

The NTLAF derivations has been further assessed in laminar nonpremixed flame, which has a wider range of chemical compositions and steeper temperature gradient, when compared with laminar premixed flame. The Indium has been seeded into the flame as dissolved Indium Chloride in water. The precision of the technique is found to be  $\sim 120$  K, across the reaction zone, where the temperature exceeds 1000 K. Indium fluorescence is observed to be the strongest at the flame front due to the local abundance of neutral Indium atoms. The observation reveals important information on the formation of free Indium atoms within the flame environment. The identification of the range where the NTLAF technique is applicable in nonpremixed flames using a water solvent to seed the Indium also highlights the potential for alternative seeding arrangements.

The Indium has been seeded into the flames as dissolved Indium Chloride in water for all of the work presented hitherto. The feasibility to improve on the signal quality of the NTLAF measurements through the substitution of organic solvent (namely acetone, isopropanol, methanol, and ethanol) for water as seeding solution has been assessed. Acetone and methanol have been shown to yield the

highest gain in the fluorescence signal intensity (approximately threefold to fivefold). Almost pure organic solvents were found to be needed to achieve significant signal intensification. Organic solvent-water mixtures with enthalpies of reaction that match the corresponding latent heats of vaporization, were therefore not used as the fluorescence signal gains associated with these mixture are observed to be not pronounced. Acetone and methanol have been shown to enhance the SNR of the fluorescence emission throughout the investigated range of flame equivalence ratios, with the most significant enhancement (approximately twofold) observed in the rich combustion region. The use of acetone or methanol has the potential to improve the precision of the NTLAF temperature measurements to  $\sim 60$  K. Acetone and methanol have also been demonstrated to have enhanced the neutral Indium formation process. The benefit associated with the organic solvents is attributed mainly to the combined influence of the more favourable physical properties of the organic solvents, as compared with water, which influence the seeding rate of the Indium species into the flame. The identification of the potential use of organic solvents in enhancing the NTLAF fluorescence signal represents a significant development to support future imaging applications in turbulent sooting flames where the background interferences are expected to be more pronounced.

The applicability of the NTLAF technique in flames with high soot loadings has been assessed. In particular, measurements have been conducted to determine the contribution of the extraneous interferences from non-Indium sources towards the total signal detected. The findings indicate that the interferences from soot, such as spurious scattering and laser-induced incandescence (LII), are not prominent. Rather, the interferences from soot precursors, predominantly condensed species (CS) and perhaps polycyclic aromatic hydrocarbons (PAH), are significant. Potential detection schemes to correct or to circumvent these interferences have been identified.

The technical feasibility of the NTLAF technique to be used concurrently with the LII technique to provide simultaneous single-shot imaging of temperature and soot concentration has been assessed. The joint NTLAF-LII method has been applied to laminar premixed and nonpremixed flames, and a wrinkled nonpremixed flame. No significant interference of these measurement techniques on each other

has been observed. All the observed features of the flames were found to be qualitatively consistent with previous work. The images also reveal that, whilst NTLAF has a limited operating range, this range is sufficient to span all regions with soot. The observation demonstrates the applicability of the joint NTLAF-LII method for the assessment of the coupled dependency of temperature and soot in sooty flames.

In summary, this work represents a breakthrough in the single-shot temperature imaging capabilities in flames containing soot, which is important for the detailed understanding of the soot formation and destruction processes in turbulent sooty flames.

## Recommendations for future work

Significant advancement towards the development of single-shot temperature imaging in sooty flames has been reported in this dissertation. Nevertheless, there remain issues that could be subjected to future investigation to complement the results of this work.

- In this work, Indium has been seeded into the flames as dissolved Indium Chloride in solvent, since gaseous fuels were used. In order to generate TLAF signals, at least part of the seeded Indium Chloride solution must be converted into free, neutral Indium atoms, as is required for TLAF. The Indium conversion process is dependent on numerous factors, such as temperature and chemical conditions. Therefore, in flames regions where the conditions are not amenable to the conversion process, insufficient Indium atoms are formed and thus no Indium fluorescence can be detected. Whilst temperature data can still be obtained in regions of greatest interest *i.e.* in and around the reaction zone, as demonstrated in this work, the absence of the Indium fluorescence in other regions can be a limitation. An alternative seeding arrangement, which permit the direct injection of free, neutral Indium atoms into all flame regions, could therefore be advantageous. The potential usage of pulsed laser ablation on Indium target to generate neutral Indium atoms [158] for seeding is currently under investigation.

- The findings from this work indicate that interferences from soot precursors, rather than soot, are prominent in flames with high soot loadings. Potential detection schemes to correct or circumvent these interferences have been identified. More work, however, is required to directly evaluate the viability and the efficacy of these detection schemes. Even an imperfect correction would allow the extension of the usable range of the NTLAF technique to flames of high soot loadings.
- Whilst single-shot temperature imaging with the use of NTLAF has been shown to be feasible in several combustion scenarios, the technique has yet to be demonstrated in a truly turbulent flame with high soot loading. Measurements in turbulent sooty flames impose challenges such as reduction in spatial fidelity, increased background interferences, and optical attenuations. Different approaches or detection schemes may be required to account for such effects.

This page intentionally left blank.

# Bibliography

- [1] S. Menon, J. Hansen, L. Nazarenko, and Y. Luo, “Climate effects of black carbon aerosols in China and India,” *Science* **297**, 2250–2253 (2002).
- [2] T. Novakov, M. O. Andreae, R. Gabriel, T. W. Kirchstetter, O. L. Mayol-Bracero, and V. Ramanathan, “Origin of carbonaceous aerosols over the tropical Indian Ocean: biomass burning or fossil fuels?” *Geophysical Research Letters* **27**, 4061–4064 (2000).
- [3] M. A. Delichatsios, J. D. Ris, and L. Orloff, “An enhanced flame radiation burner,” *Proceedings of the Combustion Institute* **24**, 1075–1082 (1992).
- [4] G. J. Nathan, J. Mi, Z. T. Alwahabi, G. J. R. Newbold, and D. S. Nobes, “Impacts of a jet’s exit flow pattern on mixing and combustion performance,” *Progress in Energy and Combustion Science* **32**, 496–538 (2006).
- [5] J. J. Parham, G. J. Nathan, J. P. Smart, S. J. Hill, and B. G. Jenkins, “The relationship between heat flux and  $\text{NO}_x$  emissions in gas-fired rotary kilns,” *Journal of the Institute of Energy* **73**, 25–34 (2000).
- [6] G. J. Nathan and B. B. Dally, “Challenges and progress in the modelling of heat transfer and  $\text{NO}_x$  emissions from rotary kiln flames involving unsteady flows,” in “Third International Conference on CFD in the Minerals and Process Industries,” (CSIRO, Melbourne, Australia, 2003).
- [7] Z. A. Mansurov, “Soot formation in combustion processes (review),” *Combustion, Explosion and Shock Waves* **41**, 727–744 (2005).
- [8] C. R. Shaddix and T. C. Williams, “Soot: giver and taker of light,” *American Scientist* **95**, 232–239 (2007).

- [9] V. Ramanathan, P. J. Crutzen, J. T. Kiehl, and D. Rosenfeld, “Aerosols, climate, and the hydrological cycle,” *Science* **294**, 2119–2124 (2001).
- [10] N. Künzli, R. Kaiser, S. Medina, M. Studnicka, O. Chanel, P. Filliger, M. Herry, F. Horak Jr, V. Puybonnieux-Textier, P. Quénel, J. Schneider, R. Seethaler, J. C. Vergnaud, and H. Sommer, “Public-health impact of outdoor and traffic-related air pollution: a European assessment,” *The Lancet* **356**, 795–801 (2000).
- [11] J. Hansen and L. Nazarenko, “Soot climate forcing via snow and ice albedos,” *Proceedings of the National Academy of Sciences* **101**, 423–428 (2004).
- [12] M. Z. Jacobson, “Strong radiative heating due to the mixing state of black carbon in atmospheric aerosols,” *Nature* **409**, 695–697 (2001).
- [13] D. W. Dockery and P. H. Stone, “Cardiovascular risks from fine particulate air pollution,” *The New England Journal of Medicine* **356**, 511–513 (2007).
- [14] K. A. Miller, D. S. Siscovick, L. Sheppard, K. Shepherd, J. H. Sullivan, G. L. Anderson, and J. D. Kaufman, “Long-term exposure to air pollution and incidence of cardiovascular events in women,” *The New England Journal of Medicine* **356**, 447–458 (2007).
- [15] I. M. Kennedy, “Models of soot formation and oxidation,” *Progress in Energy and Combustion Science* **23**, 95–132 (1997).
- [16] K. M. Leung and R. P. Lindstedt, “A simplified reaction mechanism for soot formation in nonpremixed flames,” *Combustion and Flame* **87**, 289–305 (1991).
- [17] D. Most and A. Leipertz, “Simultaneous two-dimensional flow velocity and gas temperature measurements by use of a combined particle image velocimetry and filtered Rayleigh scattering technique,” *Applied Optics* **40**, 5379–5387 (2001).
- [18] R. S. Barlow, “Laser diagnostics and their interplay with computations to understand turbulent combustion,” *Proceedings of the Combustion Institute* **31**, 49–75 (2007).

- [19] Q. N. Chan, P. R. Medwell, P. A. M. Kalt, Z. T. Alwahabi, B. B. Dally, and G. J. Nathan, “Simultaneous imaging of temperature and soot volume fraction,” *Proceedings of the Combustion Institute* **33**, 791–798 (2011).
- [20] J. Hult, A. Omrane, J. Nygren, C. F. Kaminski, B. Axelsson, R. Collin, P. E. Bengtsson, and M. Aldén, “Quantitative three-dimensional imaging of soot volume fraction in turbulent non-premixed flames,” *Experiments in Fluids* **33**, 265–269 (2002).
- [21] R. M. Fristrom and A. A. Westenberg, *Flame structure* (McGraw-Hill, 1965).
- [22] W. Stricker, R. Lückcrath, U. Meier, and W. Meier, “Temperature measurements in combustion – not only with CARS: a look back at one aspect of the European CARS workshop,” *Journal of Raman Spectroscopy* **34**, 922–931 (2003).
- [23] A. R. Masri and R. W. Bilger, “Turbulent diffusion flames of hydrocarbon fuels stabilized on a bluff body,” *Proceedings of the Combustion Institute* **20**, 319–326 (1984).
- [24] A. C. Eckbreth, *Laser diagnostics for combustion temperature and species* (Gordon and Breach Publishers, 1996).
- [25] M. Aldén, “Laser spectroscopic techniques for combustion diagnostics,” *Combustion Science and Technology* **149**, 1–18 (1999).
- [26] K. Kohse-Höinghaus and J. B. Jeffries, *Applied Combustion Diagnostics* (Taylor & Francis, 2002).
- [27] H. Haraguchi, B. Smith, S. Weeks, D. J. Johnson, and J. D. Winefordner, “Measurement of small volume flame temperatures by the two-line atomic fluorescence method,” *Applied Spectroscopy* **31**, 156–163 (1977).
- [28] G. Zizak, N. Omenetto, and J. D. Winefordner, “Laser-excited atomic fluorescence techniques for temperature measurements in flames: a summary,” *Optical Engineering* **23**, 749–755 (1984).

- [29] C. F. Kaminski, J. Engström, and M. Aldén, “Quasi-instantaneous two-dimensional temperature measurements in a spark ignition engine using 2-line atomic fluorescence,” *Proceedings of the Combustion Institute* **27**, 85–93 (1998).
- [30] G. Hartung, J. Hult, and C. F. Kaminski, “A flat flame burner for the calibration of laser thermometry techniques,” *Measurement Science and Technology* **17**, 2485–2493 (2006).
- [31] S. Prucker, W. Meier, and W. Stricker, “A flat flame burner as calibration source for combustion research: temperatures and species concentrations of premixed  $H_2$ /air flames,” *Review of Scientific Instruments* **65**, 2908–2911 (1994).
- [32] A. T. Hartlieb, B. Atakan, and K. Kohse-Höinghaus, “Temperature measurement in fuel-rich non-sooting low-pressure hydrocarbon flames,” *Applied Physics B* **70**, 435–445 (2000).
- [33] D. Hoffman, K. U. Münch, and A. Leipertz, “Two-dimensional temperature determination in sooting flames by filtered Rayleigh scattering,” *Optics Letters* **21**, 525–527 (1996).
- [34] R. B. Miles, J. N. Forkey, and W. R. Lempert, “Filtered Rayleigh scattering measurements in supersonic/hypersonic facilities,” in “AIAA 17th Aerospace Ground Testing Conference,” (AIAA-92-3894, AIAA, Nashville, USA, 1992).
- [35] G. S. Elliott, N. Glumac, and C. D. Carter, “Molecular filtered Rayleigh scattering applied to combustion,” *Measurement Science and Technology* **12**, 452–466 (2001).
- [36] S. P. Kearney, R. W. Schefer, S. J. Beresh, and T. W. Grasser, “Temperature imaging in nonpremixed flames by joint Rayleigh and Raman scattering,” *Applied Optics* **44**, 1546–1558 (2005).
- [37] R. B. Miles, A. P. Yalin, Z. Tang, S. H. Zaidi, and J. N. Forkey, “Flow field imaging through sharp-edged atomic and molecular ‘notch’ filters,” *Measurement Science and Technology* **12**, 442–451 (2001).

- [38] A. P. Yalin and R. B. Miles, “Ultraviolet filtered Rayleigh scattering temperature measurements with a mercury filter,” *Optics Letters* **24**, 590–592 (1999).
- [39] S. P. Kearney, S. J. Beresh, and T. W. Grasser, “Filtered Rayleigh scattering diagnostic for multi-parameter thermal-fluids measurements: LDRD final report. Report No. SAND2004-0158,” Tech. rep., Sandia National Laboratories (2004).
- [40] G. S. Elliott and T. J. Beutner, “Molecular filter based planar Doppler velocimetry,” *Progress in Aerospace Sciences* **35**, 799–845 (1999).
- [41] D. W. Ball, “Rayleigh and raman scattering,” *Spectroscopy* **15**, 28–29 (2001).
- [42] S. Roy, P. J. Kinnius, R. P. Lucht, and J. R. Gord, “Temperature measurements in reacting flows by time-resolved femtosecond coherent anti-Stokes Raman scattering (fs-CARS) spectroscopy,” *Optics Communications* **281**, 319–325 (2008).
- [43] M. Afzelius, P. E. Bengtsson, J. Bood, C. Brackmann, and A. Kurtz, “Development of multipoint vibrational coherent anti-Stokes Raman spectroscopy for flame applications,” *Applied Optics* **45**, 1177–1186 (2006).
- [44] M. C. Weikl, T. Seeger, M. Wendler, R. Sommer, F. Beyrau, and A. Leipertz, “Validation experiments for spatially resolved one-dimensional emission spectroscopy temperature measurements by dual-pump CARS in a sooting flame,” *Proceedings of the Combustion Institute* **32**, 745–752 (2009).
- [45] A. Malarski, F. Beyrau, and A. Leipertz, “Interference effects of C<sub>2</sub>-radicals in nitrogen vibrational CARS thermometry using a frequency-doubled Nd:YAG laser,” *Journal of Raman Spectroscopy* **36**, 102–108 (2005).
- [46] S. P. Kearney, K. Frederickson, and T. W. Grasser, “Dual-pump coherent anti-Stokes Raman scattering thermometry in a sooting turbulent pool fire,” *Proceedings of the Combustion Institute* **32**, 871–878 (2009).

- [47] K. P. Geigle, Y. Schneider-Kühnle, M. S. Tsurikov, R. Hadeß, R. Lückerrath, V. Krüger, W. Stricker, and M. Aigner, “Investigation of laminar pressurized flames for soot model validation using SV-CARS and LII,” *Proceedings of the Combustion Institute* **30**, 1645–1653 (2005).
- [48] C. J. Kliewer, Y. Gao, T. Seeger, J. Kiefer, B. D. Patterson, and T. B. Settersten, “Picosecond time-resolved pure-rotational coherent anti-Stokes Raman spectroscopy in sooting flames,” *Proceedings of the Combustion Institute* **33**, 831–838 (2011).
- [49] T. Seeger, J. Kiefer, A. Leipertz, B. D. Patterson, C. J. Kliewer, and T. B. Settersten, “Picosecond time-resolved pure-rotational coherent anti-Stokes Raman spectroscopy for N<sub>2</sub> thermometry,” *Optics Letters* **34**, 3755–3757 (2009).
- [50] T. Seeger, J. Kiefer, Y. Gao, B. D. Patterson, C. J. Kliewer, and T. B. Settersten, “Suppression of Raman-resonant interferences in rotational coherent anti-Stokes Raman spectroscopy using time-delayed picosecond probe pulses,” *Optics Letters* **35**, 2040–2042 (2010).
- [51] D. R. Richardson, R. P. Lucht, S. Roy, W. D. Kulatilaka, and J. R. Gord, “Single-laser-shot femtosecond coherent anti-Stokes Raman scattering thermometry at 1000 Hz in unsteady flames,” *Proceedings of the Combustion Institute* **33**, 839–845 (2011).
- [52] T. Lang and M. Motzkus, “Single-shot femtosecond coherent anti-Stokes Raman-scattering thermometry,” *Journal of the Optical Society of America B* **19**, 340–344 (2002).
- [53] J. D. Miller, M. N. Slipchenko, T. R. Meyer, H. U. Stauffer, and J. R. Gord, “Hybrid femtosecond/picosecond coherent anti-Stokes Raman scattering for high-speed gas-phase thermometry,” *Optics Letter* **35**, 2430–2432 (2010).
- [54] M. P. Lee, B. K. McMillin, and R. K. Hanson, “Temperature measurements in gases by use of planar laser-induced fluorescence imaging of NO,” *Applied Optics* **32**, 5379–5396 (1993).

- [55] L. Boltzmann, “Studien über das gleichgewicht der lebendigen kraft zwischen bewegten materiellen punkten,” Akademie der Wissenschaften in Wien. Mathematisch – Naturwissenschaftliche Klasse IIa **58**, 517–560 (1868).
- [56] J. M. Seitzman, R. K. Hanson, P. A. DeBarber, and C. F. Hess, “Application of quantitative two-line OH planar laser-induced fluorescence for temporally resolved planar thermometry in reacting flows,” *Applied Optics* **33**, 4000–4012 (1994).
- [57] R. Cattolica, “OH rotational temperature from two-line laser-excited fluorescence,” *Applied Optics* **20**, 1156–1166 (1981).
- [58] R. Giezendanner-Thoben, U. Meier, W. Meier, and M. Aigner, “Phase-locked temperature measurements by two-line OH PLIF thermometry of a self-excited combustion instability in a gas turbine model combustor,” *Flow, Turbulence and Combustion* **75**, 317–333 (2005).
- [59] J. Nygren, J. Engström, J. Walewski, C. F. Kaminski, and M. Aldén, “Applications and evaluation of two-line atomic LIF thermometry in sooting combustion environments,” *Measurement Science and Technology* **12**, 1294–1303 (2001).
- [60] M. Haudiquert, A. Cessou, D. Stepowski, and A. Coppalle, “OH and soot concentration measurements in a high-temperature laminar diffusion flame,” *Combustion and Flame* **111**, 338–349 (1997).
- [61] M. Tamura, J. Luque, J. E. Harrington, P. A. Berg, G. P. Smith, J. B. Jeffries, and D. R. Crosley, “Laser-induced fluorescence of seeded nitric oxide as a flame thermometer,” *Applied Physics B* **66**, 503–510 (1998).
- [62] T. Lee, J. B. Jeffries, and R. K. Hanson, “Experimental evaluation of strategies for quantitative laser-induced fluorescence imaging of nitric oxide in high-pressure flames (1–60 bar),” *Proceedings of the Combustion Institute* **31**, 757–764 (2007).
- [63] B. Atakan and A. T. Hartlieb, “Laser diagnostics of NO reburning in fuel-rich propene flames,” *Applied Physics B* **71**, 697–702 (2000).

- [64] B. K. McMillin, J. L. Palmer, and R. K. Hanson, “Temporally resolved, two-line fluorescence imaging of NO temperature in a transverse jet in a supersonic cross flow,” *Applied Optics* **32**, 7532–7545 (1993).
- [65] W. G. Bessler, F. Hildenbrand, and C. Schulz, “Two-line laser induced fluorescence imaging of vibrational temperatures in a NO-seeded flame,” *Applied Optics* **40**, 748–756 (2001).
- [66] H. Kronmayer, P. Ifeacho, C. Hecht, T. Dreier, H. Wiggers, and C. Schulz, “Gas-temperature imaging in a low-pressure flame reactor for nano-particle synthesis with multi-line NO-LIF thermometry,” *Applied Physics B* **88**, 373–377 (2007).
- [67] T. Fuyuto, H. Kronmayer, B. Lewerich, W. Koban, K. Akihama, and C. Schulz, “Laser-based temperature imaging close to surfaces with toluene and NO-LIF,” *Journal of Physics: Conference Series* **45**, 69–76 (2006).
- [68] R. K. Hanson, J. M. Seitzman, and P. H. Paul, “Planar laser-fluorescence imaging of combustion gases,” *Applied Physics B* **50**, 441–454 (1990).
- [69] D. Dabiri, “Digital particle image thermometry/velocimetry: a review,” *Experiments in Fluids* **46**, 191–241 (2009).
- [70] G. Särner, M. Richter, and M. Aldén, “Two-dimensional thermometry using temperature-induced line shifts of ZnO:Zn and ZnO:Ga fluorescence,” *Optics Letters* **33**, 1327–1329 (2008).
- [71] T. Hirasawa, Y. Kamata, T. Kaneba, and Y. Nakamura, “Visualization of ambient gas temperature based on two-color LIF,” in “9th Asia-Pacific Conference on Combustion,” (National Taiwan University, Taipei, Taiwan, 2009).
- [72] M. C. Thurber, F. Grisch, and R. K. Hanson, “Temperature imaging with single- and dual-wavelength acetone planar laser-induced fluorescence,” *Optics Letters* **22**, 251–253 (1997).
- [73] F. Grossmann, P. B. Monkhouse, M. Ridder, V. Sick, and J. Wolfrum, “Temperature and pressure dependences of the laser-induced fluorescence

- of gas-phase acetone and 3-pentanone,” *Applied Physics B* **62**, 249–253 (1996).
- [74] C. T. J. Alkemade, “A theoretical discussion on some aspects of atomic fluorescence spectroscopy in flames,” *Pure and Applied Chemistry* **23**, 73–98 (1970).
  - [75] M. Aldén, P. Grafström, H. Lundberg, and S. Svanberg, “Spatially resolved temperature measurements in a flame using laser-excited two-line atomic fluorescence and diode-array detection,” *Optics Letters* **8**, 241–243 (1983).
  - [76] J. E. Dec and J. O. Keller, “High speed thermometry using two-line atomic fluorescence,” *Proceedings of the Combustion Institute* **21**, 1737–1745 (1986).
  - [77] J. Engström, J. Nygren, M. Aldén, and C. F. Kaminski, “Two-line atomic fluorescence as a temperature probe for highly sooting flames,” *Optics Letters* **25**, 1469–1471 (2000).
  - [78] J. Hult, I. S. Burns, and C. F. Kaminski, “Two-line atomic fluorescence flame thermometry using diode lasers,” *Proceedings of the Combustion Institute* **30**, 1535–1543 (2005).
  - [79] I. S. Burns, X. Mercier, M. Wartel, R. S. M. Chrystie, J. Hult, and C. F. Kaminski, “A method for performing high accuracy temperature measurements in low-pressure sooting flames using two-line atomic fluorescence,” *Proceedings of the Combustion Institute* **33**, 799–806 (2011).
  - [80] R. G. Joklik and J. W. Daily, “Two-line atomic fluorescence temperature measurement in flames: an experimental study,” *Applied Optics* **21**, 4158–4162 (1982).
  - [81] I. S. Burns, J. Hult, and C. F. Kaminski, “Diode laser induced fluorescence spectroscopy for combustion thermometry,” *Journal of Physics: Conference Series* **15**, 201–206 (2005).
  - [82] I. S. Burns, J. Hult, G. Hartung, and C. F. Kaminski, “A thermometry technique based on atomic lineshapes using diode laser LIF in flames,” *Proceedings of the Combustion Institute* **31**, 775–782 (2007).

- [83] I. S. Burns, N. Lamoureux, C. F. Kaminski, J. Hult, and P. Desgroux, “Diode laser atomic fluorescence temperature measurements in low-pressure flames,” *Applied Physics B* **93**, 907–914 (2008).
- [84] I. S. Burns, J. Hult, and C. F. Kaminski, “Spectroscopic use of a novel blue diode laser in a wavelength region around 450 nm,” *Applied Physics B* **79**, 491–495 (2004).
- [85] U. Schwarz-Schampera and P. M. Herzig, *Indium: geology, mineralogy, and economics* (Springer, 2002).
- [86] N. Omenetto, R. Benetti, and G. Rossi, “Flame temperature measurements by means of atomic fluorescence spectrometry,” *Spectrochimica Acta* **27B**, 453–461 (1972).
- [87] J. A. Dean and C. T. Rains, *Flame Emission and Atomic Absorption Spectrometry: Theory*, vol. 1 (Marcel Dekker, Inc., 1969).
- [88] N. M. Laurendeau, “Temperature measurements by light-scattering methods,” *Progress in Energy and Combustion Science* **14**, 147–170 (1988).
- [89] L. Bütfering, G. Schmelzeisen-Redeker, and F. W. Röllgen, “Studies with a dual-beam thermospray interface in high-performance liquid chromatography mass-spectrometry,” *Journal of Chromatography* **394**, 109–116 (1987).
- [90] J. S. Casas, J. S. C. Fernández, and J. Sordo, *Lead: chemistry, analytical aspects, environment impact and health effects* (Elsevier Science, 2006).
- [91] J. H. Gibson, W. E. L. Grossman, and W. D. Cooke, “Excitation processes in flame spectroscopy,” *Analytical Chemistry* **35**, 266–277 (1963).
- [92] G. Schmelzeisen-Redeker, L. Bütfering, and F. W. Röllgen, “Desolvation of ions and molecules in thermospray mass spectrometry,” *International Journal of Mass Spectrometry and Ion Processes* **90**, 139–150 (1989).
- [93] V. A. Fassel, J. O. Rasmuson, R. N. Kniseley, and T. G. Cowley, “Relative free-atom populations in nitrous oxide-acetylene flames used in analytical spectroscopy,” *Spectrochimica Acta* **25B**, 559–575 (1970).

- [94] C. Schulz, B. F. Kock, M. Hofmann, H. Michelsen, S. Will, B. Bougie, R. Suntz, and G. Smallwood, “Laser-induced incandescence: recent trends and current questions,” *Applied Physics B* **83**, 333–354 (2006).
- [95] F. Goulay, P. E. Schrader, and H. A. Michelsen, “The effects of pulsed laser injection seeding and triggering on the temporal behavior and magnitude of laser-induced incandescence from soot,” *Applied Physics B* **96**, 613–621 (2009).
- [96] F. Goulay, P. E. Schrader, L. Nemes, M. A. Dansson, and H. A. Michelsen, “Photochemical interferences for laser-induced incandescence for flame-generated soot,” *Proceedings of the Combustion Institute* **32**, 963–970 (2009).
- [97] B. Mewes and J. M. Seitzman, “Soot volume fraction and particle size measurements with laser-induced incandescence,” *Applied Optics* **36**, 709–717 (1997).
- [98] C. R. Shaddix and K. C. Smyth, “Laser-induced incandescence measurements of soot production in steady and flickering methane, propane, and ethylene diffusion flames,” *Combustion and Flame* **107**, 418–452 (1996).
- [99] L. A. Melton, “Soot diagnostics based on laser heating,” *Applied Optics* **23**, 2201–2208 (1984).
- [100] R. L. Vander Wal and K. J. Weiland, “Laser-induced incandescence: development and characterization towards a measurement of soot-volume fraction,” *Applied Physics B* **59**, 445–452 (1994).
- [101] N. H. Qamar, G. J. Nathan, Z. T. Alwahabi, and K. D. King, “The effect of global mixing on soot volume fraction: measurements in simple jet, precessing jet, and bluff body flames,” *Proceedings of the Combustion Institute* **30**, 1493–1500 (2005).
- [102] N. H. Qamar, Z. T. Alwahabi, Q. N. Chan, G. J. Nathan, D. Roekaerts, and K. D. King, “Soot volume fraction in a piloted turbulent jet non-premixed flame of natural gas,” *Combustion and Flame* **156**, 1339–1347 (2009).

- [103] T. L. Henriksen, G. J. Nathan, Z. T. Alwahabi, N. Qamar, T. A. Ring, and E. G. Eddings, “Planar measurements of soot volume fraction and OH in a JP-8 pool fire,” *Combustion and Flame* **156**, 1480–1492 (2009).
- [104] R. L. Vander Wal, “Calibration and comparison of laser-induced incandescence with cavity ring-down,” *Proceedings of the Combustion Institute* **27**, 59–67 (1998).
- [105] R. L. Vander Wal, Z. Zhou, and M. Y. Choi, “Laser-induced incandescence calibration via gravimetric sampling,” *Combustion and Flame* **105**, 462–470 (1996).
- [106] M. Y. Choi, G. W. Mulholland, A. Hamins, and T. Kashiwagi, “Comparisons of soot volume fraction using gravimetric and light extinction techniques,” *Combustion and Flame* **102**, 161–169 (1995).
- [107] F. H. Perrin, “Whose absorption law?” *Journal of Optical Society of America* **38**, 72–74 (1948).
- [108] E. Therssen, Y. Bouvier, C. Schoemaeker-Moreau, X. Mercier, P. Desgroux, M. Ziskind, and C. Focsa, “Determination of the ratio of soot refractive index function  $E(m)$  at the two wavelengths 532 and 1064 nm by laser induced incandescence,” *Applied Physics B* **89**, 417–427 (2007).
- [109] P. S. Greenberg and J. C. Ku, “Soot volume fraction imaging,” *Applied Optics* **36**, 5514–5522 (1997).
- [110] S. D. Iuliis, F. Cignoli, and G. Zizak, “Quantitative two-dimensional imaging of soot volume fraction in flames,” in “24th Event of the Italian Section of the Combustion Institute,” (S. Margherita Ligure, 2001).
- [111] D. R. Snelling, K. A. Thomson, G. J. Smallwood, and O. L. Gülder, “Two-dimensional imaging of soot volume fraction in laminar diffusion flames,” *Applied Optics* **38**, 2478–2485 (1999).
- [112] T. C. Williams, C. R. Shaddix, K. A. Jensen, and J. M. Suo-Antilla, “Measurement of dimensionless extinction coefficient of soot within laminar diffusion flames,” *International Journal of Heat and Mass Transfer* **50**, 1616–1630 (2007).

- [113] P. R. Medwell, P. A. M. Kalt, and B. B. Dally, "Simultaneous imaging of OH, formaldehyde, and temperature of turbulent nonpremixed jet flames in a heated and diluted coflow," *Combustion and Flame* **148**, 48–61 (2007).
- [114] P. R. Medwell, P. A. M. Kalt, and B. B. Dally, "Imaging of diluted turbulent ethylene flames stabilized on a jet in hot coflow (JHC) burner," *Combustion and Flame* **152**, 100–113 (2008).
- [115] J. A. Dean and C. T. Rains, *Flame Emission and Atomic Absorption Spectrometry: Components and Techniques*, vol. 2 (Marcel Dekker, Inc., 1971).
- [116] R. K. Winge, V. A. Fassel, and R. N. Kniseley, "Direct nebulization of metal samples for flame atomic-emission and absorption spectroscopy," *Applied Spectroscopy* **25**, 636–642 (1971).
- [117] R. J. Lang, "Ultrasonic atomization of liquids," *The Journal of Acoustical Society of America* **34**, 6–8 (1962).
- [118] P. Rajan and A. B. Pandit, "Correlations to predict droplet size in ultrasonic nebulization," *Ultrasonics* **39**, 235–255 (2001).
- [119] C. D. West and D. N. Hume, "Radiofrequency plasma emission spectrophotometer," *Analytical Chemistry* **36**, 412–415 (1964).
- [120] K. W. Olson, W. J. Haas Jr., and V. A. Fassel, "Multielement detection limits and sample nebulization efficiencies of an improved ultrasonic nebulizer and a conventional pneumatic nebulizer in inductively coupled plasma-atomic emission spectrometry," *Analytical Chemistry* **49**, 632–637 (1977).
- [121] H. Matusiewicz, M. S. M. Hidalgo, and A. Canals, "Evaluation of various nebulizers for use in microwave induced plasma optical emission spectrometry," *Journal of Analytical Atomic Spectrometry* **22**, 1174–1178 (2007).
- [122] R. L. Vander Wal, "Laser-induced incandescence: detection issues," *Applied Optics* **35**, 6548–6559 (1996).
- [123] ABB Australia website. Available at <http://www.abb.com/ProductGuide/>; Last accessed: 6 December 2010 .

- [124] G. V. Deverall, K. W. Meissner, and G. J. Zissis, “Hyperfine structures of resonance lines of Indium ( $\text{In}^{115}$ )\*,” *Physics Review* **91**, 297–299 (1953).
- [125] J. E. Sansonetti and W. C. Martin, “Handbook of basic atomic spectroscopic data,” *Journal of Physical and Chemical Reference Data* **34**, 1559–2259 (2005).
- [126] P. A. Bonczyk, “Effects of metal additives on soot precursors and particulates in a  $\text{C}_2\text{H}_4/\text{O}_2/\text{N}_2/\text{Ar}$  premixed flame,” *Fuel* **70**, 1403–1411 (1991).
- [127] U. Wieschnowsky, H. Bockhorn, and F. Fetting, “Some new observations concerning the mass growth of soot in premixed hydrocarbon-oxygen flames,” *Proceedings of the Combustion Institute* **22**, 343–352 (1988).
- [128] B. S. Haynes, H. Jander, and H. G. Wagner, “The effect of metal additives on the formation of soot in premixed flames,” *Proceedings of the Combustion Institute* **17**, 1365–1374 (1979).
- [129] J. H. Kent and S. J. Bastin, “Parametric effects on sooting in turbulent acetylene diffusion flames,” *Combustion and Flame* **56**, 29–42 (1984).
- [130] J. W. Berry, D. G. Chappell, and R. B. Barnes, “Improved method of flame photometry,” *Industrial and Engineering Chemistry Analytical Edition* **18**, 19–24 (1946).
- [131] R. Avni and C. T. J. Alkemade, “The role of some organic solvents in flame photometry,” *Microchimica Acta* **48**, 460–471 (1960).
- [132] J. Elhanan and W. D. Cooke, “Factors affecting line intensities in the flame spectrometry of metals in organic solvents,” *Analytical Chemistry* **38**, 1062–1063 (1966).
- [133] D. Sindayihebura, M. Dobre, and L. Bolle, “Experimental study of thin liquid film ultrasonic atomization,” in “4th World Conference on Experimental Heat Transfer, Fluid Mechanics and Thermodynamics,” (Brussels, Belgium, 1997), pp. 1249–1256.
- [134] W. N. Wang, A. Purwanto, I. W. Lenggoro, K. Okuyama, H. Chang, and H. D. Jang, “Investigation on the correlations between droplet and particle

- size distribution in ultrasonic spray pyrolysis,” *Industrial and Engineering Chemistry Research* **47**, 1650–1659 (2008).
- [135] B. Avvaru, M. N. Patil, P. R. Gogate, and A. B. Pandit, “Ultrasonic atomization: effect of liquid phase properties,” *Ultrasonics* **44**, 146–158 (2006).
  - [136] C. G. Fotache, T. G. Kreutz, D. L. Zhu, and C. K. Law, “An experimental study of ignition in nonpremixed counterflowing hydrogen versus heated air,” *Combustion Science and Technology* **109**, 373–393 (1995).
  - [137] J. B. Willis, “Atomization problems in atomic absorption spectroscopy -I. A study of the operation of a typical nebulizer, spray chamber and burner system,” *Spectrochimica Acta* **23A**, 811–830 (1967).
  - [138] L. R. Snyder and J. J. Kirkland, *Introduction to modern liquid chromatography* (John Wiley & Sons, Inc., 1979).
  - [139] K. Fujiwara, H. Haraguchi, and K. Fuwa, “Profiles of the distribution of atoms in the nitrous oxide-acetylene flame,” *Bulletin of the Chemical Society of Japan* **48**, 857–862 (1975).
  - [140] C. Schoemaeker-Moreau, E. Therssen, X. Mercier, J. F. Pauwels, and P. Desgroux, “Two-color laser-induced incandescence and cavity ring-down spectroscopy for sensitive and quantitative imaging of soot and PAHs in flames,” *Applied Physics B* **78**, 485–492 (2004).
  - [141] A. Gomez, M. G. Littman, and I. Glassman, “Comparative study of soot formation on the centerline of axisymmetric laminar diffusion flames: fuel and temperature effects,” *Combustion and Flame* **70**, 225–241 (1987).
  - [142] J. Zerbs, K. P. Geigle, O. Lammel, J. Hader, R. Stirn, R. Hadeff, and W. Meier, “The influence of wavelength in extinction measurements and beam steering in laser-induced incandescence measurements in sooting flames,” *Applied Physics B* **96**, 683–694 (2009).
  - [143] K. C. Smyth and C. R. Shaddix, “The elusive history of  $\tilde{m}=1.57-0.56i$  for the refractive index of soot,” *Combustion and Flame* **107**, 314–320 (1996).

- [144] J. Zhu, M. Y. Choi, G. W. Mulholland, S. L. Manzello, L. A. Gritzo, and J. Suo-Anttila, “Measurements of visible and near-IR optical properties of soot produced from laminar flames,” *Proceedings of Combustion Institute* **29**, 2367–2374 (2002).
- [145] G. Prado, A. Garo, A. Ko, and A. Sarofim, “Polycyclic aromatic hydrocarbons formation and destruction in a laminar diffusion flame,” *Proceedings of the Combustion Institute* **20**, 989–996 (1984).
- [146] R. L. Vander Wal, K. A. Jensen, and M. Y. Choi, “Simultaneous laser-induced emission of soot and polycyclic aromatic hydrocarbons within a gas jet-diffusion flame,” *Combustion and Flame* **109**, 399–414 (1997).
- [147] A. Ciajolo, A. D’Anna, and R. Barbella, “PAH and high molecular weight species formed in a premixed methane flame,” *Combustion Science and Technology* **100**, 271–281 (1994).
- [148] A. Ciajolo, R. Ragucci, B. Apicella, R. Barbella, M. de Joannon, and A. Tregrossi, “Fluorescence spectroscopy of aromatic species produced in rich premixed ethylene flames,” *Chemosphere* **42**, 835–841 (2001).
- [149] A. Ciajolo, B. Apicella, R. Barbella, A. Tregrossi, F. Beretta, and C. Al-louis, “Depletion of fuel aromatic components and formation of aromatic species in a spray flame as characterized by fluorescence spectroscopy,” *Energy & Fuel* **15**, 987–995 (2001).
- [150] F. Beretta, V. Cincotti, A. D’Alessio, and P. Menna, “Ultraviolet and visible fluorescence in the fuel pyrolysis regions of gaseous diffusion flames,” *Combustion and Flame* **61**, 211–218 (1985).
- [151] L. Petarca and F. Marconi, “Fluorescence spectra and polycyclic aromatic species in a *n*-heptane diffusion flame,” *Combustion and Flame* **78**, 308–325 (1989).
- [152] D. S. Coe and J. I. Steinfeld, “Fluorescence excitation and emission spectra of polycyclic aromatic hydrocarbons at flame temperatures,” *Chemical Physics Letters* **76**, 485–489 (1980).

- [153] B. S. Haynes and H. G. Wagner, “Soot formation,” *Progress in Energy and Combustion Science* **7**, 229–273 (1981).
- [154] H. Bladh, J. Johnsson, and P. E. Bengtsson, “On the dependence of the laser-induced incandescence (LII) signal on soot volume fraction for variations in particle size,” *Applied Physics B* **90**, 109–125 (2008).
- [155] J. Reimann, S. A. Kuhlmann, and S. Will, “Improvement in soot concentration measurements by laser-induced incandescence (LII) through a particle size correction,” *Combustion and Flame* **153**, 650–654 (2008).
- [156] A. V. Menon, S. Y. Lee, M. J. Linevsky, T. A. Litzinger, and R. J. Santoro, “Addition of  $\text{NO}_2$  to a laminar premixed ethylene-air flame: effect on soot formation,” *Proceedings of the Combustion Institute* **31**, 593–601 (2007).
- [157] L. M. Pickett and J. B. Ghandhi, “Structure of a reacting hydrocarbon-air planar mixing layer,” *Combustion and Flame* **132**, 138–156 (2003).
- [158] K. Alti and A. Khare, “Low-energy low-divergence pulsed indium atomic beam by laser ablation,” *Laser and Particle Beams* **24**, 47–53 (2006).
- [159] S. Brohez, C. Delvosalle, and G. Marlair, “A two-thermocouples probe for radiation corrections of measured temperatures in compartment fire,” *Fire Safety Journal* **39**, 399–411 (2004).

This page intentionally left blank.

# Appendix A

## Theoretical Derivations

### A.1 Linear Two-Line Atomic Fluorescence

Referring to Figure 4.1, the rate equation for pumping to level 2 via optical absorption from lower state  $i$  (*viz.*  $i = 0$  or  $1$ ) is given by [24]:

$$\frac{dN_2}{dt} = N_i(Q_{i2} + B_{i2}I_{i2}) - N_2(B_{2i}I_{2i} + Q + A_{20} + A_{21}) . \quad (\text{A.1})$$

Here,  $N$  is the population in the corresponding energy level,  $Q$  is the non-radiative rate constant,  $A$  is the transition probability coefficient for spontaneous absorption or emission,  $B$  is the transition probability coefficient for stimulated absorption or emission, and  $I$  is the incident laser spectral irradiance. The subscripts refer to the transition between the energy levels.

Following excitation, the fluorescence process from level 2 to lower state  $i$  may be described by [24]

$$F_{2i} = h\nu_{2i}N_2A_{2i}\frac{\Omega}{4\pi}V , \quad (\text{A.2})$$

where  $F$  is the fluorescence intensity,  $h\nu$  is the photon energy,  $\Omega$  is the collection solid angle, and  $V$  is the measurement volume.

Taking the ratio of the two fluorescence signals, based on Equation A.2, gives

$$\frac{F_{20}}{F_{21}} = \frac{h\nu_{20} \frac{\Omega_{20}\varepsilon_{20}}{4\pi} \frac{N_1 B_{12} I_{12} A_{20}}{B_{21} I_{21} + Q + A}}{h\nu_{21} \frac{\Omega_{21}\varepsilon_{21}}{4\pi} \frac{N_0 B_{02} I_{02} A_{21}}{B_{20} I_{20} + Q + A}}, \quad (\text{A.3})$$

where  $\varepsilon$  represents the collection efficiency and  $A = A_{20} + A_{21}$ .

In the weak excitation regime *i.e.* the linear excitation regime,  $B_{21}I_{21}$  and  $B_{21}I_{21}$  are lesser than  $Q + A$ , the ratio of the two fluorescence signals can therefore be reduced to

$$\frac{F_{20}}{F_{21}} = \frac{h\nu_{20} \frac{\Omega_{20}\varepsilon_{20}}{4\pi} \frac{N_1 B_{12} I_{12} A_{20}}{Q + A}}{h\nu_{21} \frac{\Omega_{21}\varepsilon_{21}}{4\pi} \frac{N_0 B_{02} I_{02} A_{21}}{Q + A}}, \quad (\text{A.4})$$

Noting that

$$g_i B_{ij} = g_j B_{ji}, \quad (\text{A.5})$$

and

$$B_{ij} = \frac{g_j}{g_i} \frac{\lambda_{ij}^3 A_{ji}}{8h\pi}. \quad (\text{A.6})$$

The quotient of the fluorescence signals ratio in Equation A.4 can now be simplified to

$$\frac{F_{20}}{F_{21}} = \frac{\nu_{20} \Omega_{20} \varepsilon_{20} g_0 N_1 I_{12} \lambda_{12}^3}{\nu_{21} \Omega_{21} \varepsilon_{21} g_1 N_0 I_{02} \lambda_{02}^3}. \quad (\text{A.7})$$

The Boltzmann distribution [55] can be expressed as

$$\frac{N_j}{N_i} = \frac{g_j}{g_i} e^{\frac{-(E_j - E_i)}{kT}}. \quad (\text{A.8})$$

Combining Equation A.7 with Equation A.8

$$\frac{F_{20}}{F_{21}} = \frac{\Omega_{20} \varepsilon_{20} I_{12} \lambda_{12}^4}{\Omega_{21} \varepsilon_{21} I_{02} \lambda_{02}^4} e^{\frac{-(E_1 - E_0)}{kT}}. \quad (\text{A.9})$$

Taking the natural logarithm of Equation A.9 and re-arranging the equation, it can be shown that in the linear excitation regime, the temperature expression is given by [76],

$$T = \frac{\Delta E_{10}/k}{\ln\left(\frac{F_{21}}{I_{02}}\right) - \ln\left(\frac{F_{20}}{I_{12}}\right) + 4\ln\left(\frac{\lambda_{21}}{\lambda_{20}}\right) + \ln\left(\frac{\Omega_{20}\varepsilon_{20}}{\Omega_{21}\varepsilon_{21}}\right)} . \quad (\text{A.10})$$

Or,

$$T = \frac{\Delta E_{10}/k}{\ln\left(\frac{F_{21}}{I_{02}}\right) - \ln\left(\frac{F_{20}}{I_{12}}\right) + 4\ln\left(\frac{\lambda_{21}}{\lambda_{20}}\right) + C_t} . \quad (\text{A.11})$$

Here  $\Delta E$  is the energy difference between levels, and  $C_t$  is a constant dependent on a number of experimental factors (such as collection efficiency) and is best determined from experimental calibration.

## A.2 Nonlinear Two-Line Atomic Fluorescence

Equation A.11 and previous TLAf studies rely on the assumption of excitation occurs in the linear laser-induced fluorescence (LIF) regime. To improve the fluorescence signal, there are potential advantages in extending the fluence beyond the linear limit. In this case, the previously defined theory and derivations will no longer apply.

Without any simplifications resulting from linearity assumptions, the derivation of the quotient of the fluorescence signals follows a similar procedure; however, the numerator of Equation A.3 is now re-expressed as

$$F_{20} = h\nu_{20} \frac{\Omega_{20}\varepsilon_{20}}{4\pi} N_1 A_{20} \frac{B_{12}}{B_{21}} \frac{1}{1 + \frac{Q+A}{B_{21}I_{21}}} . \quad (\text{A.12})$$

Combining Equation A.12 with Equation A.5 gives

$$F_{20} = h\nu_{20}A_{20}N_1 \frac{\Omega_{20}\varepsilon_{20}}{4\pi} \frac{g_2}{g_1} \frac{1}{1 + \frac{Q+A}{B_{21}I_{21}}} . \quad (\text{A.13})$$

Applying the same re-arrangement to the denominator, equation A.3 can now be expressed as the ratio

$$\frac{F_{20}}{F_{21}} = \frac{\nu_{20}\Omega_{20}\varepsilon_{20}A_{20}N_1g_0}{\nu_{21}\Omega_{21}\varepsilon_{21}A_{21}N_0g_1} \left( \frac{1 + \frac{Q+A}{B_{20}I_{20}}}{1 + \frac{Q+A}{B_{21}I_{21}}} \right) . \quad (\text{A.14})$$

Using the previously defined  $C_S$  and  $C_A$  (Equation 5.2 and Equation 5.3) allows Equation A.14 to be written as

$$\frac{F_{20}}{F_{21}} = \frac{\nu_{20}\Omega_{20}\varepsilon_{20}A_{20}N_1g_0}{\nu_{21}\Omega_{21}\varepsilon_{21}A_{21}N_0g_1} \left( \frac{1 + \frac{C_S}{I_{20}}}{1 + \frac{C_A}{I_{21}}} \right) , \quad (\text{A.15})$$

Applying the Boltzmann function yields

$$\frac{F_{20}}{F_{21}} = \frac{\nu_{20}\Omega_{20}\varepsilon_{20}A_{20}}{\nu_{21}\Omega_{21}\varepsilon_{21}A_{21}} \left( \frac{1 + \frac{C_S}{I_{20}}}{1 + \frac{C_A}{I_{21}}} \right) e^{-\Delta E_{10}/kT} . \quad (\text{A.16})$$

Taking the natural logarithm and re-arranging Equation A.16 to express the temperature explicitly, the equation for NTLAF takes the form of

$$T = \frac{\Delta E_{10}/k}{\ln \left( F_{21} \times \left( 1 + \frac{C_S}{I_{20}} \right) \right) - \ln \left( F_{20} \times \left( 1 + \frac{C_A}{I_{21}} \right) \right) + C_T} , \quad (\text{A.17})$$

where  $C_T$  is previously defined (Equation 5.4).

The temperature expression now includes two additional parameters,  $C_S$  and  $C_A$ , that result in the equation being independent of the fluence regime.

# Appendix B

## Radiation Correction

Radiation correction of the thermocouple reading involves an estimation of the energy balance between the energy received via conduction from the gas and that lost via radiation from the thermocouple bead. In steady state conditions, the energy balance on the thermocouple bead can be expressed as [159]

$$h_c(T_g - T_b) = \epsilon_b \sigma (T_b^4 - T_\infty^4) . \quad (\text{B.1})$$

Here,  $T_\infty$  is the effective temperature of the surrounding,  $T_b$  is the thermocouple temperature,  $T_g$  is the gas temperature,  $\epsilon_b$  is the bare-bead thermocouple emissivity,  $h_c$  is the convective heat transfer coefficient, and  $\sigma$  is the Stefan-Boltzmann constant.

Convective heat transfer coefficient  $h_c$  between gas flow and the thermocouple bead can be estimated using Whitaker's correlation for external flow over a sphere, for  $0.71 < Pr < 380$  and  $3.5 < Re < 7.6 \times 10^4$  [159]:

$$Nu = 2 + 0.4(Re^{0.5} + 0.06Re^{0.67})Pr^{0.4} . \quad (\text{B.2})$$

The Nusselt, Reynolds and Prandtl number are defined as;

$$Nu = \frac{h_c D_b}{k_g} , \quad (\text{B.3})$$

$$Re = \frac{\rho_g U_g D_b}{\mu_g} , \quad (B.4)$$

$$Pr = \frac{c_{p,g} \mu_g}{k_g} . \quad (B.5)$$

Here,  $D_b$  is the diameter of the thermocouple bead,  $U_g$  is the local gas velocity in the vicinity of the thermocouple bead,  $\rho_g$  is the density of the gas,  $\mu_g$  is the viscosity of gas,  $c_{p,g}$  is the heat capacity of gas, and  $k_g$  is the thermal conductivity of gas.

# Appendix C

## Publications

### Journal Publications

1. N. H. F. Qamar, G. J. Nathan, Z. T. Alwahabi, and Q. N. Chan , “Soot sheet dimensions in turbulent nonpremixed flames,” *Combustion and Flame*, DOI: 10.1016/j.combustflame.2011.04.017 (2011).
2. G. J. Nathan, P. A. M. Kalt, Z. T. Alwahabi, B. B. Dally, P. R. Medwell, and Q. N. Chan , “Recent advances in the measurement of strongly radiating, turbulent reacting flows,” *Progress in Energy and Combustion Science*, DOI: 10.1016/j.pecs.2011.04.001 (2011).
3. Q. N. Chan, P. R. Medwell, Z. T. Alwahabi, B. B. Dally, and G. J. Nathan, “Assessment of interferences to nonlinear two-line atomic fluorescence (NTLAF) in sooty flames,” *Applied Physics B*, DOI: 10.1007/s00340-011-4497-0 (2011).
4. P. R. Medwell, G. J. Nathan, Q. N. Chan, Z. T. Alwahabi, and B. B. Dally, “The influence on the soot distribution within a laminar flame of radiation at fluxes of relevance to concentrated solar radiation,” *Combustion and Flame*, DOI: 10.1016/j.combustflame.2011.01.006 (2011).
5. Q. N. Chan, P. R. Medwell, P. A. M. Kalt, Z. T. Alwahabi, B. B. Dally, and G. J. Nathan, “Simultaneous imaging of temperature and soot volume fraction,” *Proceedings of the Combustion Institute* **33**, 791–798 (2011).

6. **Q. N. Chan**, P. R. Medwell, P. A. M. Kalt, Z. T. Alwahabi, B. B. Dally, and G. J. Nathan, “Solvent effects on two-line atomic fluorescence of Indium,” *Applied Optics* **49**, 1257–1266 (2010).
7. P. R. Medwell, **Q. N. Chan**, P. A. M. Kalt, Z. T. Alwahabi, B. B. Dally, and G. J. Nathan, “Instantaneous temperature imaging of diffusion flames using two-line atomic fluorescence,” *Applied Spectroscopy* **64**, 173–176 (2010).
8. P. R. Medwell, **Q. N. Chan**, P. A. M. Kalt, Z. T. Alwahabi, B. B. Dally, and G. J. Nathan, “Development of temperature imaging using the two-line atomic fluorescence,” *Applied Optics* **48**, 1237–1248 (2009).
9. N. H. F. Qamar, Z. T. Alwahabi, **Q. N. Chan**, G. J. Nathan, D. Roekaerts, and K. D. King, “Soot volume fraction in a piloted turbulent jet non-premixed flame of natural gas,” *Combustion and Flame*, **156**, 1339–1347 (2009).

## Refereed Conference Publications

1. **Q. N. Chan**, P. R. Medwell, P. A. M. Kalt, Z. T. Alwahabi, B. B. Dally, and G. J. Nathan, “Evaluation of nonlinear regime two-line atomic fluorescence (NTLAF) in sooty flames” in “The 10<sup>th</sup> Asia-Pacific Conference on Combustion,” (Hyderabad, India, 2010).
2. **Q. N. Chan**, P. R. Medwell, P. A. M. Kalt, Z. T. Alwahabi, B. B. Dally, and G. J. Nathan, “Simultaneous imaging of soot concentration and temperature in ethylene diffusion flames,” in “CHEMECA,” (The University of Adelaide, Adelaide, Australia, 2010).
3. P. R. Medwell, **Q. N. Chan**, and B. B. Dally, “Effect of fuel type on the reaction zone structure of moderate or intense low Oxygen dilution (MILD) combustion,” in “CHEMECA,” (The University of Adelaide, Adelaide, Australia, 2010).
4. G. J. Nathan, P. A. M. Kalt, Z. T. Alwahabi, B. B. Dally, P. R. Medwell, and **Q. N. Chan**, “Invited review: Recent advances in measurement of

turbulent reacting flows in which heat transfer is dominated by radiation,” in “14th International Heat Transfer Conference,” (Washington DC, USA, 2010).

5. **Q. N. Chan**, P. R. Medwell, P. A. M. Kalt, Z. T. Alwahabi, B. B. Dally, and G. J. Nathan, “Effects of solvent on laser-induced fluorescence in the context of two-line atomic fluorescence,” in “Australasian Conference on Optics Lasers and Spectroscopy,” (The University of Adelaide, Adelaide, Australia, 2009), pp. 44–45.
6. **Q. N. Chan**, P. R. Medwell, P. A. M. Kalt, Z. T. Alwahabi, B. B. Dally, and G. J. Nathan, “Temperature imaging of nonpremixed flames using non-linear regime two-line atomic fluorescence (NTLAF),” in “Proceedings of the Australian Combustion Symposium,” (The University of Queensland, Brisbane, Australia, 2009), pp. 63–66.
7. **Q. N. Chan**, P. R. Medwell, P. A. M. Kalt, Z. T. Alwahabi, B. B. Dally, and G. J. Nathan, “Comparison of water and acetone as solvent for two-line atomic fluorescence (TLAF),” in “Proceedings of the Australian Combustion Symposium,” (The University of Queensland, Brisbane, Australia, 2009), pp. 95–98.
8. G. J. Nathan, Z. T. Alwahabi, B. B. Dally, P. R. Medwell, and **Q. N. Chan**, “Progress and challenges in experimental investigations of realistic turbulent reacting flows,” in “Proceedings of the Australian Combustion Symposium,” (The University of Queensland, Brisbane, Australia, 2009), pp. 23–38.
9. **Q. N. Chan**, P. R. Medwell, P. A. M. Kalt, Z. T. Alwahabi, B. B. Dally, and G. J. Nathan, “Temperature measurement using non-linear two-line atomic fluorescence,” in “The 9<sup>th</sup> Asia-Pacific Conference on Combustion,” (National Taiwan University, Taipei, Taiwan, 2009).
10. P. R. Medwell, **Q. N. Chan**, P. A. M. Kalt, Z. T. Alwahabi, B. B. Dally, and G. J. Nathan, “Development of two-line atomic fluorescence (TLAF) technique for temperature measurement,” in “5<sup>th</sup> Australian Conference on Laser Diagnostics in Fluid Mechanics and Combustion,” (The University of Western Australia, Perth, Australia, 2008), pp. 116–118.

11. P. R. Medwell, Q. N. Chan, P. A. M. Kalt, Z. T. Alwahabi, B. B. Dally, and G. J. Nathan, “Non-linear regime two-line atomic fluorescence (NT-LAF) for temperature measurement,” in “5<sup>th</sup> Australian Conference on Laser Diagnostics in Fluid Mechanics and Combustion,” (The University of Western Australia, Perth, Australia, 2008), pp. 119–122.
12. N. H. F. Qamar, Z. T. Alwahabi, Q. N. Chan, G. J. Nathan, and D. Roekaerts, “Measurements of soot volume fraction in TNF Delft flame,” in “Proceedings of the Australian Combustion Symposium,” (The University of Sydney, Sydney, Australia, 2007), pp. 42–45.
13. Z. T. Alwahabi, J. Reppel, G. J. Nathan, Q. N. Chan, and K. D. King, “Structure of precessing jet methane flames from the planar hydroxyl radical distributions,” in “Proceedings of the Australian Combustion Symposium,” (The University of Sydney, Sydney, Australia, 2007), pp. 38–41.